

Innovative measurement techniques for atmospheric turbulence and wind energy

THÈSE N° 8536 (2018)

PRÉSENTÉE LE 31 MAI 2018

À LA FACULTÉ DE L'ENVIRONNEMENT NATUREL, ARCHITECTURAL ET CONSTRUIT
LABORATOIRE D'INGÉNIERIE ÉOLIENNE ET D'ÉNERGIE RENOUVELABLE
PROGRAMME DOCTORAL EN MÉCANIQUE

ÉCOLE POLYTECHNIQUE FÉDÉRALE DE LAUSANNE

POUR L'OBTENTION DU GRADE DE DOCTEUR ÈS SCIENCES

PAR

Fernando CARBAJO FUERTES

acceptée sur proposition du jury:

Dr M. Farhat, président du jury
Prof. F. Porté Agel, directeur de thèse
Prof. T. K. Mikkelsen, rapporteur
Prof. J. K. Lundquist, rapporteuse
Dr K. Mulleners, rapporteuse



ÉCOLE POLYTECHNIQUE
FÉDÉRALE DE LAUSANNE

Suisse
2018

Acknowledgements

This doctoral thesis is the tangible result of a long journey that, on a personal level, has significantly transcended its academic scope. During this period I have had an invaluable the opportunity to discover and learn extensively, not only about science, but also about myself and others. The precious teachings that I have acquired will undoubtedly shape me for the future. They are enough to write another thesis about them, but unfortunately they do not belong in this work.

This dissertation, which comes to an end today, has proved to be a challenge that, at many points, seemed insurmountable. During the tougher moments, which were more than the easier ones, I have been lucky enough to be able to count on many people that blindly believed in me and provided unconditional help and love. Among all of them, Cristina occupies the most important position and has shared most of my struggles during these years. It is not possible to express in a few lines how indebted I am to her love, kindness and patience. The dearest thank you from the bottom of my heart will never suffice, but it is the best that I can offer in return as of today.

My family has been the most important source of inspiration and influence in my life. I look up to each one of them, older and younger. Thanks to them I am never alone, despite the long distances that have separated us in the last nine years. My parents, who I greatly admire, inculcated in me important values from a very early age and that has been a priceless gift that will help me for the rest of my life. My aunt Cuqui, my brothers Eduardo and Alfredo, my grandparents Hortensia and Pepe, and those who are not with us anymore, Esperanza and Tino, complete the picture of the people that watch over me, give me strength and provide continuous guidance and infinite love.

A very particular thank you is reserved for Prof. Fernando Porté-Agel, for giving me the opportunity of being part of an incredible institution such as EPFL and the freedom to explore my own ideas and carry out my particular, perhaps unorthodox, approach to fluid mechanics research. I would also like to thank the committee members of my defense, Prof. Torben K. Mikkelsen, Prof. Julie K. Lundquist, Prof. Karen Mulleners and Dr. Mohamed Farhat.

Two specific persons were of great help at different stages of my work. Prof. G. Valerio Iungo was the first person I got to know in the WiRE laboratory and the one who taught me and helped me at the beginning of my research. Prof. Corey D. Markfort always made easier the

Acknowledgements

difficult challenges and was a pleasure working with him at the end of my thesis. They are two people with an incredibly positive attitude towards life who I admire, both at the scientific and personal level. Special thanks go to both of them.

I have been lucky enough to have by my side many fantastic engineers or physicists and ultimately great colleagues that helped my research during their civilian service period (Nicolas Bocherens, Aidan Jungo, Thomas Curran, Brian Sifringer, Matthias Hofer, Kevin Sin and Lionel Wilhelm) and their studies at EPFL (Frédéric Amblard, Cagri Atac, Jaime Legerén, Raffi Kazjian, Robin Luthi, Sébastien Schwegler and Martin Bodenand). I hoped they learned from me as much as I learned from them. The interaction with all of them has been, beyond a shadow of a doubt, the most fulfilling experience in my short academic career.

Finally, WiRE has managed to gather a number of fantastic people, without exception, with whom I shared sorrows and joys and who were ready to put a smile in my face first thing in the morning. Majid, Sina, Vince, Zoe, Mou, Nicolas, Joel, Alejandro, Deepu, Vera, Wai Chi, Ahmad, Mahdi, Ting, Farshid, Corinne, Carole, Pierre and Jiannong were the best companions of my journey.

I want to dedicate the last lines to the many great friends that I have made in these years in Lausanne and who provided much needed fun moments and an escape from the academic daily life. I cherish the uncountable hours in long discussions with Vlado, Magda, Giacomo, Carlos and many others while having lunch at the university, grilling by the lake, biking in the Lavaux or hiking and skiing in the mountains. And since it is difficult to separate personal life from the doctoral studies, they also deserve their place here.

Lausanne, 2018

Fernando. C. F.

Abstract

The measurement of different atmospheric flow quantities is of utmost importance for a correct understanding of most atmospheric phenomena. Researchers and industry in the fields of meteorology and wind engineering demand extensive and accurate measurements of atmospheric turbulence for a better understanding of its role in a wide range of applications such as weather forecast, wind resource evaluation, wind turbine wake flow, pollutant transport or urban climate. Quantitative measurements of relevant variables are particularly valuable for the development, testing and validation of turbulence parameterizations used in both analytical and numerical models. This thesis focuses on the development of innovative measurement techniques for atmospheric turbulence, particularly suitable for wind energy applications, and it is divided into four different studies.

The first study presents a multirotor UAV-based technique for the measurement of atmospheric turbulence and temperature. The technique is based on the integration of a fast-response multi-hole pressure probe and a thermocouple with an inertial measurement unit (IMU). This technique allows for an accurate measurement of time series of the three components of the velocity vector and temperature at any point in the atmosphere in which the UAV can fly. The technique relies on the correction of the velocity vector measured by the pressure probe on the frame of reference of the UAV -non inertial- with the information provided by the IMU. The study includes a validation of the technique against sonic anemometry and the measurement of the signature of tip vortices shed by the blades of a full-scale wind turbine as an example of its potential.

The second study presents a triple-lidar technique developed for the measurement of atmospheric turbulence at a point in space from synchronous measurements of three intersecting Doppler wind lidars. The laser beams must be non-coplanar so that trigonometric relationships allow the reconstruction of the velocity vector. The technique is validated against sonic anemometry in terms of the instantaneous velocity vector, turbulence statistics, Reynolds stresses and the spectra of the three components of the velocity and the turbulent kinetic energy.

The third study investigates the theoretical accuracy of the reconstruction of a full-scale wind turbine wake in terms of the average and the standard deviation of the longitudinal velocity component by volumetric scans from lidar measurements. To that end, a series of virtual experiments are performed, where synthetic lidar measurements are obtained from LES simulation results. The methodology described quantifies the errors and allows the

Acknowledgements

optimization of the scan pattern so that it balances the different error sources and minimizes the total error.

The fourth study presents a measurement campaign dedicated to the characterization of full-scale wind turbine wakes under different inflow conditions. The measurements are performed with two nacelle-mounted scanning lidars. The first lidar characterizes the inflow while the second performs horizontal planar scans of the wake. The relationships obtained for the growth rate of wake width, velocity recovery and length of the near wake are compared to analytical models and allow to correct the parameters prescribed until now with new, more accurate values directly derived from full-scale experiments.

Key words: Airborne meteorology; Atmospheric boundary layer; Field experiments; LiDAR; Remote sensing; Sonic anemometry; Triple lidar; Turbulence measurements; UAV; Virtual LiDAR; Wake measurements; Wake modeling; Wind energy; Wind turbine wakes.

Résumé

La mesure de différentes variables atmosphériques est très importante pour une bonne compréhension de la plupart des phénomènes atmosphériques. Les chercheurs et l'industrie dans les domaines de la météorologie et de l'éolien exigent des mesures étendues et précises de la turbulence pour mieux comprendre son rôle dans un large éventail d'applications telles que les prévisions météorologiques, le potentiel éolien, le sillage, le transport des polluants ou le climat urbain. Les mesures quantitatives des variables pertinentes sont particulièrement utiles pour le développement, l'essai et la validation des modèles analytiques et numériques. Cette thèse porte sur le développement des techniques de mesure innovantes pour la turbulence atmosphérique, particulièrement adaptées aux applications éoliennes, et est divisé en quatre études différentes.

La première étude présente une technique basée sur un drone pour la mesure de la turbulence atmosphérique et de la température. La technique repose sur l'intégration d'une sonde de pression multi-trous à réponse rapide et d'un thermocouple avec une unité de mesure inertielle (IMU). Cette technique permet une mesure précise des séries temporelles des trois composantes du vecteur vitesse et de la température à n'importe quel point de l'atmosphère dans lequel le drone peut voler. La vitesse mesurée par la sonde de pression dans le référentiel non inertiel de l'UAV est corrigée grâce aux informations fournies par l'IMU. L'étude inclut une validation de la technique contre l'anémométrie sonique et la mesure de la signature des tourbillons de pointe créés par les aubes d'une éolienne.

La seconde étude présente une technique de lidar développée pour la mesure de la turbulence atmosphérique en un point de l'espace à partir de mesures synchrones de trois lidars entrecroisés. Les faisceaux laser doivent être non coplanaires de sorte que les relations trigonométriques permettent la reconstruction du vecteur vitesse. La technique est validée avec les résultats d'un anémomètre à ultrasons en comparant les vecteurs de vitesse instantanée, les statistiques de turbulence, les composantes du tenseur de Reynolds et les spectres des trois composantes de la vitesse et de l'énergie cinétique turbulente.

La troisième étude évalue la précision théorique de la reconstruction d'un sillage d'éolienne à grande échelle en termes de moyenne et l'écart-type de la composante de vitesse longitudinale par des balayages volumétriques d'un lidar. À cette fin, une série d'expériences virtuelles sont réalisées, où des mesures lidar synthétiques sont obtenues à partir des résultats d'une simulation LES. La méthodologie décrite quantifie les erreurs et permet l'optimisation du balayage de sorte qu'il équilibre les différentes sources d'erreur en minimisant l'erreur totale.

Acknowledgements

La quatrième étude présente des mesures dédiées à la caractérisation de sillages d'éoliennes dans différentes conditions flux incident . Les mesures sont effectuées par deux lidars montés sur la nacelle. Le premier lidar caractérise le vent en amont tandis que le second effectue des balayages planaires horizontaux du sillage. Les relations obtenues pour le taux de croissance de la largeur de sillage, la vitesse de récupération et la longueur du sillage proche sont comparées aux modèles analytiques et permettent de corriger les paramètres prescrits jusqu'à présent avec de nouvelles valeurs plus précises directement issues d'expériences en taille réelle.

Mots clefs : Anémométrie sonique; Couche limite atmosphérique; Drone; Énergie éolienne; Expériences de terrain; Lidar; Lidar virtuel; Lidar triple; Mesures de la turbulence; Mesures de sillage; Météorologie aéroportée; Modèles de sillage; Sillage d'éoliennes; Télédétection.

Contents

Acknowledgements	i
Abstract (English/Français)	iii
Contents	viii
List of figures	ix
List of tables	xiii
1 Introduction	1
2 Multicopter UAV-based platform for the measurement of atmospheric turbulence: validation and signature detection of tip vortices of wind turbine blades.	5
2.1 Introduction	6
2.2 Material and Methods	7
2.2.1 UAV platform and instrumentation	8
2.2.2 Data processing	12
2.3 Results	13
2.3.1 Validation of the measurement technique	13
2.3.2 Wind turbine blade tip-vortex signature detection	17
2.4 Summary	23
3 3D turbulence measurements using three synchronous wind lidars: validation against sonic anemometry	25
3.1 Introduction	26
3.2 Experimental set-up	26
3.2.1 CESAR observatory and meteorological mast	26
3.2.2 LiDAR system	27
3.2.3 Positioning system	27
3.2.4 Configuration	27
3.3 Technique and data analysis	28
3.3.1 The meteorological coordinate system and the transformation matrix	28
3.3.2 Comparison with sonic anemometry	30
3.4 Results	31

Contents

3.4.1	Instantaneous velocity vector	32
3.4.2	Turbulence statistics	32
3.4.3	Turbulence spectra	34
3.5	Summary	34
4	Using a virtual lidar approach to assess the accuracy of the volumetric reconstruction of a wind turbine wake.	37
4.1	Introduction	38
4.2	Methodology	41
4.2.1	LES simulations	42
4.2.2	Lidar virtual measurements	44
4.2.3	Scanning strategy and reconstruction of 3D fields	46
4.2.4	Optimization	47
4.3	Results	48
4.3.1	Error of the average longitudinal velocity component	48
4.3.2	Error of the standard deviation of the longitudinal velocity component	54
4.4	Summary	59
5	Wind turbine wake characterization with nacelle-mounted wind lidars for analytical wake model validation.	61
5.1	Introduction	62
5.2	Methodology	63
5.2.1	Test site	63
5.2.2	Lidar setup	66
5.2.3	Upstream scanning	67
5.2.4	Downstream scanning and reconstruction of planar velocity fields	70
5.2.5	Wake analysis	71
5.3	Results	73
5.4	Summary	78
6	Overall summary and future research perspectives	81
6.1	Overall summary	81
6.2	Future research perspectives	82
	Bibliography	94
	Curriculum Vitae	95

List of Figures

2.1	Image of the UAV platform in stationary flight photographed from the ground. The fast-response pressure probe and the thermocouple are mounted at the extremity of a carbon fiber beam and at a distance of 115 cm from the UAV center in order to avoid the rotor downwash. The rest of the equipment is mounted on a platform below the main UAV body.	9
2.2	Image of the fast-response pressure probe. The cylindrical body of the probe can be seen in the back and the four pressure tap locations on the 2 mm wide faceted head are highlighted. On the bottom left part of the image, a schematic of the front view of the faceted head is presented.	10
2.3	Photographic view of the meteorological tower inside the EPFL campus. The red arrow represents the incoming wind direction during the tests. The sonic anemometer is located at 25 m height. The nearest building is 10 m high.	14
2.4	Example of time series of the IMU variables used for the retrieval of the wind velocity in the geographical fixed frame of reference, as explained in equation 2.1 and in section 2.2. The variables shown correspond to test 1 of table 2.2 and figure 2.5. Top: angular velocity of the UAV in its frame of reference; center: Euler angles in the geographical frame of reference; bottom: translation velocity of the UAV in the geographical frame of reference.	17
2.5	Comparison of wind speed and temperature time series of the sonic anemometer and the UAV-based technique for the first 300 s of test 1 presented in table 2.2. The UAV-based measurements have been downsampled to match the 20 Hz frequency of the sonic anemometer.	18
2.6	Spectra of the streamwise and vertical wind velocity components, the temperature and $w'T'$. The sonic anemometer and the UAV platform results are shown for the test 1, whose statistics are presented in Table 2.2. The spectrum has been computed using Hanning windows of 30 s and 50% overlapping. The UAV-based measurements have been downsampled to match the 20 Hz frequency of the sonic anemometer.	19
2.7	Perspective view of the flat section of the Rhone valley in which the E-70 wind turbine is located (46°09'35"N 7°02'14"E), as well as the villages of Collonges and Dorénaz. Map data: Google, DigitalGlobe.	20

List of Figures

2.8	Horizontal wind speed, wind direction and virtual potential temperature measured during an ascent-descent flight three rotor diameters upstream of the wind turbine. The dark blue and light blue lines present, respectively, the data obtained during the ascent and descent flights. The black dashed line represents the wind turbine hub height and the red dashed lines the upper and lower limits of the turbine rotor. The ABL shows small variations of all variables across the rotor disk during the tests.	21
2.9	Signature of detected tip vortex pairs. Top: tangential velocity in ms^{-1} of two consecutive 2D free vortices separated approximately 9 m in the longitudinal direction and with a strength $\Gamma = 50 \text{ m}^2\text{s}^{-1}$. Their lateral distance to the measurement point (long dashed white line) is indicated. Bottom: velocity components of the vortex pairs measured together with the signature of the 2D free vortices depicted on the top part. Taylor's frozen approximation has been used in order to convert time series to spatial measurements.	22
3.1	Sketch of the configuration of the lidars, together with the meteorological mast and the sonic anemometer.	28
3.2	Sketch of the meteorological coordinate system and an arbitrary radial velocity measured by a wind Doppler lidar	29
3.3	Graphical concept of the pseudo-spatial filtering applied one of the velocity components measured by the sonic anemometer	31
3.4	Example of the reconstructed components of the velocity vector in streamwise coordinates with triple-lidar technique against filtered and unfiltered measurements by the sonic anemometer (only 5 minutes presented)	32
3.5	Spectra of the longitudinal, transversal and vertical components of the wind velocity as well as turbulent kinetic energy measured with triple-lidar technique against filtered and unfiltered measurements by the sonic anemometer	34
4.1	Inflow conditions in terms of average horizontal wind speed and longitudinal, transversal and vertical turbulence intensity. The panels on top (a) show three cases with the same turbulence intensity (medium) but different wind speeds, while the panels at the bottom (b) show three cases with the same wind speed (medium) at hub height but different turbulence intensities. The resulting average transversal and vertical velocities from the LES simulations are negligible.	43
4.2	Flow statistics of the simulated wind turbine wakes for the five different inflow cases studied. The figures present vertical symmetry planes of the longitudinal component of the wind velocity in terms of its average (a) and its standard deviation (b). The black boxes correspond to the location of the wind turbine rotor.	44

4.3	Example of errors in the reconstruction of the longitudinal average velocity component associated only with the assumption of unidimensional flow. The errors correspond to the MV-MT inflow case and for the lidar installed on the nacelle (a) and at the base of the tower (b) . The volume of interest is delimited by the white dashed line. The figures show the error as a percentage of the undisturbed wind speed at hub height (see section 4.2.1).	49
4.4	Example of total errors in the reconstruction of $\bar{u}(x, y, z)$ for three different angular resolutions. The errors correspond to the MV-MT inflow case with the nacelle-mounted lidar. The volume of interest is delimited by the white dashed line, and spherical grid points are marked as white dots. The figures show the error as a percentage of the undisturbed wind speed at hub height (see section 4.2.1).	52
4.5	$\sigma_u(x, y, z)$ from LES simulations (a) and example of its reconstruction. The example corresponds to the MV-MT inflow case and to the nacelle-mounted lidar. The volume of interest is delimited by the white dashed line, and spherical grid points are marked as white dots. The figures show the magnitude of $\sigma_u(x, y, z)$ in m/s.	55
5.1	Power coefficient and blade pitch angle as function of the wind speed for the 2.5 MW Liberty C96 wind turbine obtained from SCADA data. 10-minute values are shown in blue dots and binned averages in red. A quasi constant power coefficient is observed for wind speeds from 5 to 10 m/s.	64
5.2	Location of the wind turbine and the meteorological tower inside Kirkwood's campus as well as the outskirts of Cedar Rapids. Map data: Google, Image NASA.	65
5.3	Wind rose measured at the Eastern Iowa Airport for 10 years, situated approximately 5 km to the SW of the wind turbine and visible in Figure 5.2. The wind presents two main directions: NW and SSE. Data obtained from Iowa State University, Iowa Environmental Mesonet. The length of the bars indicate frequency in percentage units.	66
5.4	Sketch of the lidar setup with one lidar dedicated to the measurement of the incoming flow conditions and another one dedicated to the characterization of the wake.	67
5.5	Example of the estimation of the yaw angle and the horizontal wind speed at hub height with plan position indicator (PPI) scans. Data corresponding to the period 22h30–22h35, 15 September 2017.	68
5.6	Example of the characterization of the vertical profile of horizontal velocity with range height indicator (RHI) scans. The red dashed lines indicate the upper and lower limits of the rotor. (a) All measurements; (b) Binned statistics. 22h35–22h40, 15 September 2017.	69
5.7	Example of the average and standard deviation of the wake in polar and Cartesian coordinates. 22h30–23h00, 15 September 2017. Units in m/s.	71

List of Figures

5.8	Example of the analysis of the wake of the wind turbine. (a) Velocity deficit and Gaussian fits; (b) Downstream evolution of the fit parameters. 22h30–23h00, 15 September 2017.	73
5.9	Example of three cases of wakes for increasing different longitudinal turbulence intensity conditions at hub height (Case 1–2.2%; Case 2–4.6%; Case 3–9.9%). The top quadrants present the adimensional velocity deficit while the bottom quadrants present the longitudinal turbulence intensity in the horizontal plane at hub height. These three example cases are further referenced in Figures 5.10–5.12.	75
5.10	Relationship between wake growth k^* and longitudinal turbulence intensity TI_x . In blue all the data collected during the experiment, in dashed red the linear fit to the full-scale field data presented in Equation (5.16). In black the data obtained from Bastankhah and Porté-Agel (2014) and the linear fit used in Niayifar and Porté-Agel (2016). Numbers 1 to 3 indicate the cases presented in Figure 5.9.	76
5.11	Relationship between wake growth k^* and wake width at the rotor ε . In blue all the data collected during the experiment, in dashed red the linear fit to the full-scale field data presented in Equation (5.17). In black the data obtained from Bastankhah and Porté-Agel (2014). Labels numbered 1 to 3 indicate the cases presented in Figure 5.9.	77
5.12	Relationship between near wake length ℓ_{nw} and longitudinal turbulence intensity TI_x . In blue all the data collected during the experiment, in dashed black Equation (5.18) for the estimation of the near wake length with the value of $\alpha = 2.32$ prescribed in Bastankhah and Porté-Agel (2016) and in dashed red the same equation with the value of $\alpha = 3.6$ that provides a better fit to the full-scale field data. The grey rectangle at the bottom indicates the lowest bound for a possible calculation of the near wake length with the presented setup and analysis. Numbers 1 to 3 indicate the cases presented in Figure 5.9.	78

List of Tables

2.1	Main specifications of the MULTIROTOR G4 Eagle. * Note: The endurance is highly affected by the wind speed and the payload.	8
2.2	Comparison of flow statistics obtained with the UAV platform and a sonic anemometer at a height of 25 m over the EPFL campus.	15
3.1	Differences in statistics of wind speed and direction between the sonic anemometer measurements and the lidar technique proposed. Note that the differences calculated are always between the filtered sonic data and the lidar measurements.	33
4.1	Ranges of the azimuth and elevation angles needed to cover the whole volume of interest for both lidar locations	46
4.2	Angular resolutions used for the 3D scan optimization and corresponding number of repetitions for each laser beam orientation.	48
4.3	Errors in the reconstruction of the average longitudinal velocity component associated only with the assumption of unidimensional flow. The errors are presented for the different inflow cases studied in terms of average and maximum values found within the volume of interest (see section 4.2.3 and white dashed lines in figure 4.3) for both nacelle-mounted and ground-based lidars. Percentages are based on the undisturbed wind speed at hub height (see section 4.2.1)	50
4.4	Example of optimization of the angular resolution for one inflow case and both lidar locations. The table presents the average and maximum total errors for the reconstruction of the average longitudinal velocity component inside the volume of interest. The errors are shown as a percentage of the undisturbed wind speed at hub height (see section 4.2.1).	53
4.5	Total average and maximum errors for the reconstruction of $\bar{u}(x, y, z)$ inside the volume of interest for all inflow cases studied and both lidar locations with the overall optimum angular resolution of 3° . The errors are shown as a percentage of the undisturbed wind speed at hub height (see 4.2.1). The optimum values found in table 4.4 correspond to the first column of this table.	54

List of Tables

4.6	Total average and maximum errors for the reconstruction of $\sigma_u(x, y, z)$ inside the volume of interest for all inflow cases studied and both lidar locations with the overall optimum angular resolution of 3° . The errors are shown as a percentage of the undisturbed wind speed at hub height (see section 4.2.1).	56
4.7	Total average and maximum errors for the reconstruction of $\bar{u}(x, y, z)$ inside the volume of interest for all inflow cases studied and both lidar locations. The errors are shown as a percentage of the undisturbed wind speed at hub height (see section 4.2.1). The errors corresponding to an optimum angular resolution for each case are identified with an asterisk.	57
4.8	Total average and maximum errors for the reconstruction of $\sigma_u(x, y, z)$ inside the volume of interest for all inflow cases studied and both lidar locations. The errors are shown as a percentage of the undisturbed wind speed at hub height (see section 4.2.1). The errors corresponding to an optimum angular resolution for each case are identified with an asterisk.	58
5.1	Wind turbine main characteristics.	64

1 Introduction

The correct understanding of most atmospheric phenomena relies on observations of different variables such as the atmospheric pressure, the temperature, humidity and density of the air, the speed and direction of the wind or the chemical composition of the air. The lower part of the atmosphere is mostly influenced by its mechanical and thermal interaction with the Earth's surface and this region is called the atmospheric boundary layer (ABL). Within the ABL, the atmospheric turbulence is the main driver of the vertical exchanges of momentum, heat, water and gases like CO₂ or CH₄ (Stull, 1988; Kaimal and Finnigan, 1994). Therefore, accurate measurements of turbulence quantities are particularly valuable for the development, testing and validation of turbulence parameterizations used in analytical and numerical models used in a wide range of onshore and offshore applications like weather forecasting, pollutant transport, urban climate studies or wind energy. Some of the most used turbulence quantities in the study of the ABL are longitudinal, transversal and vertical turbulence intensities as well as vertical turbulent flux of momentum and heat, but an accurate measurement of these quantities poses still nowadays a significant challenge (Mullan, 2016; Rambola, 2016).

Different measurement techniques have been developed during the last century according to the hardware and data processing possibilities of the time. Tethered balloons are best suited to profiling of atmospheric chemistry, temperature and wind speed and direction but do not excel in turbulence characterization. A cup anemometer and a wind vane or a propeller anemometer, if accurately calibrated, are good tools for long-term measurement of wind speed and direction, but they are unable of measuring the three components of the wind vector and their turbulent fluctuations. The standard tool for turbulence measurement in the atmosphere, the sonic anemometer, offers a good accuracy, reliability, robustness and high spatial and temporal resolution, but similarly to cup or propeller anemometers, it only offers point-wise information and its location is limited by the possibility of erecting a meteorological mast where the turbulence quantities need to be quantified.

Advances in the last two decades propose alternatives to the sonic anemometer and the meteorological mast. The two most interesting fields in meteorological instrumentation for ABL turbulence measurements are unmanned aerial vehicles (UAV) for airborne meteorology

Chapter 1. Introduction

(Elston et al., 2015) and remote sensing (Emeis, 2011). Their main advantage over traditional techniques is their flexibility and ability to take measurements where other instruments cannot be installed. Nevertheless, they also have disadvantages: UAV-based techniques are still mostly in prototype phase, they are not suitable for long-term statistics because of their limited autonomy and covering a volume with point-wise measurements would imply thousands of hours of flights. On the other hand, light detection and ranging (lidar) is able to effectively cover long distances and volumes in the atmosphere, although its spatial and temporal resolution is still unable to match that of the other techniques mentioned.

Chapter 2 presents the development and validation of a multirotor UAV-based platform for the measurement of atmospheric turbulence based on the corrections of the measurements of a multihole fast-response pressure probe with the information of an inertial measurement unit (IMU). The most important advantage of multirotor UAVs over fixed-wing UAVs relies on their capability of stationary flight. **Chapter 3** presents the development and validation of a triple-lidar technique for the measurement of atmospheric turbulence based on the trigonometric reconstruction of the three components of the velocity vector from the radial velocity measurements of three intersecting lidar beams. Both techniques are able to provide time series of the three components of the velocity vector, although they have different advantages: the UAV provides higher spatial and temporal resolution, making it ideal to study smaller scale phenomena such as the tip vortices shed by the blades of wind turbines, while the triple-lidar is ideal for the study of the bigger scales of turbulence since it is able to provide long term statistics.

Among the different applications that require extensive atmospheric measurements, wind energy is one of the most demanding. These measurements are needed to develop, improve and validate models that can optimize the wind farm layout and wind farm control as well as accurately predict the power generation. To that end, a complete characterization of the interaction between the atmospheric wind and the rotor of the wind turbine is needed. This includes: a detailed description of the incoming conditions of the ABL (ideally the thermal stability, the vertical profile of horizontal wind speed and direction, the three dimensional turbulence intensity at hub height and the yaw angle), a correct determination of the power and thrust coefficients and volumetric descriptions of the wind turbine wake in terms of the velocity deficit and the turbulence increase.

Light detection and ranging (lidar) instruments are arguably the best suited instruments for the study of the interaction between the wind and the turbine rotor, but their most important limitation arises from the Doppler effect: they can only provide measurements of radial velocity of the wind -i.e. the velocity component parallel to the laser orientation. Consequently, lidar techniques normally rely on different assumptions -e.g. horizontal homogeneity of the ABL- for the calculation of the horizontal or vertical components of the wind. Nevertheless, there is a lack of investigation of the effects of these assumptions in the uncertainty of many lidar techniques. **Chapter 4** presents the quantification of the error and the optimization of the measurement strategy of a wind turbine wake by volumetric lidar measurements from

virtual lidar measurements obtained from large-eddy simulations (LES). Finally, **chapter 5** presents the setup and data analysis used as well as the results from a measurement campaign dedicated to the characterization of the wake of a full scale single wind turbine for wake model validations. An overall summary and future research perspectives are presented in **chapter 6**.

2 **Multirotor UAV-based platform for the measurement of atmospheric turbulence: validation and signature detection of tip vortices of wind turbine blades.**¹

Abstract

The present study describes the development of a technique for the measurement of atmospheric turbulence and temperature at a point in space based on the integration of a fast-response multi-hole pressure probe and a thermocouple with an inertial measurement unit on a multirotor UAV-based platform. This allows for an accurate measurement of time series of the three components of the velocity vector and temperature at any point in space in which the UAV can fly within the limitations of its autonomy. The presented technique relies on an accurate correction of the three-component velocity vector measured by the pressure probe on the frame of reference of the UAV -non inertial- with the information provided by the inertial measurement unit. The study includes a validation of the technique against sonic anemometry and the measurement of the signature of tip vortices shed by the blades of a full-scale wind turbine as an example of its potential.

¹The contents of this chapter are currently under review: E. Carbajo Fuertes, L. Wilhelm and F. Porté-Agel. Multirotor UAV-based platform for the measurement of atmospheric turbulence: validation and signature detection of tip vortices of wind turbine blades. *Journal of Atmospheric and Oceanic Technology*.

2.1 Introduction

Precise measurements of different atmospheric flow quantities are of paramount importance for the correct understanding of most atmospheric phenomena. Quantitative measurements of the relevant variables are particularly valuable for the development, testing and validation of turbulence parameterizations used in both analytical and numerical models. Atmospheric models predict flow features at different scales, ranging from a few meters in the case of micrometeorological models to hundreds of kilometers in the case of global atmospheric models, but most of them rely heavily on a correct quantification of the atmospheric turbulence. Some of the most used turbulence quantities in the study of atmospheric boundary layer (ABL) are longitudinal, transversal and vertical turbulence intensities as well as vertical turbulent flux of momentum and heat, but an accurate measurement of these quantities poses still nowadays a significant challenge.

Different measurement techniques have been developed during the last century according to the hardware and data processing possibilities of the time for the measurement of atmospheric flow quantities. Tethered balloons are best suited to profiling of atmospheric chemistry, temperature and wind speed and direction but do not excel in turbulence characterization. A cup anemometer and a wind vane or a propeller anemometer, if accurately calibrated, are good tools for long-term measurement of wind speed and direction, but they are unable of measuring the three components of the wind vector and their turbulent fluctuations. Remote sensing techniques comprise a series of airborne, satellite-based and ground based techniques, of which ground-based Light Detection and Ranging (lidar) is the most suitable for ABL wind speed and direction measurements, as proved by Köpp et al. (1984), as well as turbulence characterization, as shown by Pichugina et al. (2012). Since it is based on the Doppler principle, it is only able to measure velocities parallel to the laser beam and therefore it must rely on some assumptions for the characterization of the transversal components as in Sathe et al. (2011), Sathe and Mann (2012) or Newman and Clifton (2017), unless it is used in a triple-lidar configuration as shown by Carbajo Fuertes et al. (2014) or Vasiljević et al. (2016). Still, the triple-lidar technique presents a limitation of spatial resolution to approximately 10-20 m, inherent in the laser wavelengths used.

Recently, a series of fixed-wing unmanned aerial vehicle (UAV) platforms have been developed by Spiess et al. (2007), van den Kroonenberg et al. (2008), Mansour et al. (2011), Martin et al. (2011), Reineman et al. (2013) or Wildmann et al. (2014b). They make use of inertial measurement units in conjunction with pressure-based measurements in order to retrieve the wind vector within the UAV trajectory at a high frequency and are therefore able to calculate turbulent fluxes. Nevertheless, most of these techniques use the assumption of horizontally homogeneous flow since a fixed-wing UAV cannot fly statically. By repeating a programmed trajectory a number of times it is possible to gather spatial statistics and eliminate the assumption of horizontally homogeneous flow. Some applications in the field of wind energy can be found in Kocer et al. (2011), Reuder and Jonassen (2012), Wildmann et al. (2014a), Subramanian et al. (2015a) and Subramanian et al. (2015b).

Despite the impressive developments in both remote sensing and UAV-based techniques of the last two decades, the sonic anemometer remains the standard instrument for turbulence quantification in the atmosphere. Its most important advantages are its accuracy, reliability and robustness when measuring the three components of the wind vector and the air temperature. Its main disadvantage lies in the fact that it needs to be installed on a meteorological tower, which limits the height of the measurements and the locations where it can be placed (e.g. inside an urban canyon or a wind farm). The technique presented in this article has some of the advantages of sonic anemometry such as high accuracy and high spatial and temporal resolution, while addressing the limitation in the location of sonic anemometers and the need for horizontally homogeneous flow used by fixed-wing UAV platforms. These limitations can be overcome by placing all the equipment on a rotary-wing UAV, which can fly statically in almost any point within the ABL. On the other hand, while the autonomy of many fixed-wing platforms is in the order to a few hours, the higher power required for static flight limits rotary-wing UAV autonomy to a few tens of minutes, which limits the duration of the measurements. However, developments in high energy density cells are quickly pushing this boundary.

The presented technique opens new possibilities for atmospheric turbulence measurements, with one particularly suitable application being the study of tip vortices of full-scale wind turbine blades. The tip vortices shed by the blades are complex turbulent vortical structures characteristic of turbine near-wake flows that evolve rapidly and have radii of only a few meters. Therefore they are difficult structures to measure and characterize with current standard measurement techniques. Most of the quantitative knowledge of these structures derives from the wind tunnel studies of [Leishman et al. \(1997\)](#), [Grant and Parkin \(2000\)](#), [Vermeer \(2001\)](#), [Haans et al. \(2008\)](#), [Lignarolo et al. \(2014a\)](#) or [Bastankhah et al. \(2017\)](#). Nevertheless, some attempts at full-scale measurements include the use of more traditional sonic anemometers installed on meteorological towers as shown by [Toloui et al. \(2015\)](#), measurements with fixed-wing UAVs like [Subramanian et al. \(2016\)](#) and more innovative approaches such as full-scale particle image velocimetry (PIV) using snowfall as in [Hong et al. \(2014\)](#). The use of a rotary-wing UAV platform is the only technique that provides time series of the velocity vector at any desired point in the near wake of a full-scale turbine, thus allowing for an accurate detection of the signature of tip vortices.

2.2 Material and Methods

This section includes a detailed description of the UAV platform and all the instrumentation used, as well as an explanation of the post-processing used to reconstruct the wind velocity vector from the raw data of each instrument.

Chapter 2. Multirotor UAV-based platform for the measurement of atmospheric turbulence: validation and signature detection of tip vortices of wind turbine blades.

2.2.1 UAV platform and instrumentation

The two most important elements of the proposed measurement technique are an octocopter UAV, which is used to situate the instruments at the desired point in space, and a multi-hole fast-response pressure probe for the measurement of the three components of the wind velocity vector.

Since the wind velocity measurements are taken relative to the UAV reference frame and the latter is by nature non-inertial, they have to be transformed back to a frame of reference of interest. Generally, they will be transformed to a fixed and horizontal reference frame. To that end, the measurements of the rest of the auxiliary instrumentation are involved; namely the accelerometer, gyroscope, magnetometer, and Global Positioning System (GPS) sensors (from here on, Inertial Measurement Unit - *IMU*). Although every UAV control includes most or all of these instruments in its control system, they have not been used as measurements. Only external instruments to the UAV of high quality and with well-known accuracies have been used instead.

UAV platform

The UAV platform used in this project is an octocopter *MULTIROTOR G4 Eagle*. Its main characteristics are detailed in table 2.1.

Table 2.1 – Main specifications of the MULTIROTOR G4 Eagle. * Note: The endurance is highly affected by the wind speed and the payload.

MULTIROTOR G4 Eagle specs	
Number of rotors	8
Diameter of rotors	40 cm
Maximum airspeed	60 km/h
UAV weight	3.5 kg
UAV weight + payload	5.6 kg
Maximum take-off weight	6.0 kg
Range	2000 m
Diameter (to center of rotors)	88 cm
Height	49 cm
Endurance*	10-20 min
Battery charge	2 x 12 Ah

All the external sensors described below, except the fast-response pressure probe and thermocouple, are mounted fixed to the UAV structure and below its main body for maximum protection from the rotors downwash. The extension of the area of influence of the downwash of the rotors has been measured with the help of auxiliary tests and using the same pressure probe in a controlled laboratory environment. The pressure probe as well as the thermocouple have been mounted horizontally on a carbon fiber beam that extends 115 cm upstream

in front of the UAV in order to avoid any influence of the rotors downwash. The beam has been rigidified with two auxiliary trusses in order to minimize the vibrations and for it to be as solid as possible to the UAV platform, therefore reducing a potential source of error or contamination of the velocity measurements. The complete setup can be seen in figure 2.1.



Figure 2.1 – Image of the UAV platform in stationary flight photographed from the ground. The fast-response pressure probe and the thermocouple are mounted at the extremity of a carbon fiber beam and at a distance of 115 cm from the UAV center in order to avoid the rotor downwash. The rest of the equipment is mounted on a platform below the main UAV body.

Fast-response pressure probe

The wind velocity vector is measured with a custom-made 4-hole fast-response pressure probe developed by Turbulent Flow Instrumentation (shown in figure 2.2) with a measurement range of $2\text{-}30\text{ ms}^{-1}$ and certified for frequency responses up to 600 Hz. The probe features a 10 cm long cylindrical body with a 5 cm long and 2 mm diameter head, which sets the spatial resolution of the measurement technique. The analog signal of all the four pressure transducers is filtered with a 250 Hz first-order analog low-pass filter in order to eliminate potential high-frequency noises on the signal. These voltages are then read with a 16-bit analog to digital converter (ADC) on a $\pm 10\text{ V}$ range following the instructions of the manufacturer in order to improve the velocity resolution for this particular application. A thorough description of an earlier, but similar model of the pressure probe is provided in [Hooper and Musgrove \(1997\)](#).

The acceptance cone of the pressure probe is $\pm 45^\circ$. This implies that the main direction of the wind should be known in advance and the pressure probe pointed against that direction.

Chapter 2. Multirotor UAV-based platform for the measurement of atmospheric turbulence: validation and signature detection of tip vortices of wind turbine blades.

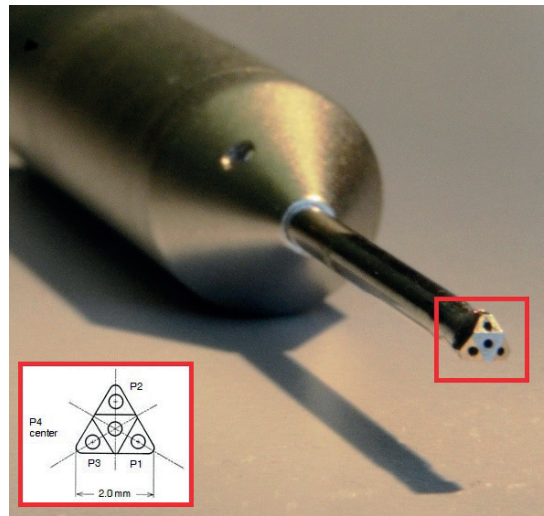


Figure 2.2 – Image of the fast-response pressure probe. The cylindrical body of the probe can be seen in the back and the four pressure tap locations on the 2 mm wide faceted head are highlighted. On the bottom left part of the image, a schematic of the front view of the faceted head is presented.

To that end, a rough estimation of the direction of the flow can be easily obtained if the UAV is allowed to drift with the wind for a few seconds. The limitation of the acceptance cone of the pressure probe, nevertheless, makes this technique not suitable for the measurement of atmospheric flows that can present extreme turbulence intensity and/or flow reversal. However, it should be noted that these conditions are not commonly encountered in most atmospheric turbulent flows. Example of these conditions can be found inside urban canopies or in highly convective ABL in conjunction with very low wind speeds.

Temperature, pressure and humidity sensor

The fast-response pressure probe needs a good characterization of the air density in order to convert the pressures measured into wind velocities. The air density and the virtual potential temperature are calculated using a temperature, pressure and humidity (TPH) sensor BME280 manufactured by Bosch. The accuracy of temperature, pressure and humidity is ± 1 °C, ± 1 hPa and $\pm 3\%$ RH respectively.

Thermocouple

A fine-wire thermocouple has been used in order to obtain temperature measurements at the same location of the pressure probe in order to be able to calculate turbulent heat fluxes in the atmosphere. The distance between the pressure probe and the thermocouple is approximately 2 cm perpendicular to the flow. This ensures the coherence of the synchronous measurements of temperature and wind velocity up to very small scales. The thermocouple is mounted

without any support or protection in order not to disturb the wind velocity measurements and at the same time minimize its response time.

High temperature resolution of the fine-wire thermocouple is crucial for a correct characterization of the turbulent heat fluxes. The selected thermocouple consists of an 80 μm diameter type-E Chromel-Constantan junction, which presents a very high sensitivity in the atmospheric temperature range compared with other common thermocouple types, yielding a temperature resolution of 68 $\mu\text{V} / ^\circ\text{C}$. Although these kind of thermocouples are widely used for the measurement of temperature fluctuations in the atmosphere in order to calculate the vertical turbulent transport of heat, their frequency response characteristics beyond a few Hertz are often object of controversy. The time constant of the thermocouple used in this experiment is estimated to be in the order of a few tens of ms by Dupont et al. (1984) and Pandey (1985). Response compensation techniques are normally used to mitigate this effect and increase their validity range in the frequency domain as shown by Tagawa et al. (2005) and Kato et al. (2007) so that the thermocouples are able to capture the most energetic scales that contribute to the heat transport. If the complete description of very fine scales is needed, the thermocouple can be substituted by a faster sensor such as a fast-response platinum wire thermometer. Nevertheless, the fragility of this sensor makes its manipulation much more delicate.

Inertial measurement unit (IMU)

The IMU used is an Ellipse N-G4A2-B1 manufactured by SBG systems and features a 3-axis accelerometer, a 3-axis gyroscope, a 3-axis magnetometer and a GPS module. The maximum output rate is 200 Hz. The raw measurements of each sensor are processed internally by the IMU processing board. The latter makes use of an extended Kalman filter which fuses inertial data with a Global Navigation Satellite System (GNSS), Odometer, and GPS information in order to output, among others, Euler angles, angular velocities, translation velocities and position.

The accuracy is $\pm 0.2^\circ$ for the pitch and roll angles and $\pm 0.5^\circ$ for the yaw angle. As the magnetic environment is highly affected by the UAV rotors, the yaw angle is subject to bias errors that are estimated to be within $\pm 5^\circ$ as seen in some tests. The accuracy of the translation velocity is 0.1 ms^{-1} .

Data acquisition system

The data collection of all the instruments detailed above is implemented using a *myRIO-1900* real-time embedded evaluation board from National Instruments which runs LabVIEW Virtual Instruments software. The data acquisition is performed at a maximum sampling rate of 50 Hz. This frequency threshold, which is imposed by the limits in processing power of both the MyRIO data acquisition system and the IMU, ensures synchronous acquisition of all

Chapter 2. Multirotor UAV-based platform for the measurement of atmospheric turbulence: validation and signature detection of tip vortices of wind turbine blades.

instruments' readings at each time step.

The Kolmogorov spatial scales in atmospheric turbulent flow can be determined by $\eta/l_o \sim Re^{-3/4}$, where l_o denotes the integral length scale (in the order of 1000 m), and the Reynolds number Re is based on l_o and the wind velocity u_o . The Kolmogorov temporal scale could then be estimated as $\tau_{z\eta} = \eta/u_o$ as defined by Pope (2000). Common values are 0.1 mm for the spatial scale and 0.1 ms for the temporal scale, which corresponds to a frequency of 1 kHz. This implies that, even though the spatial resolution of the pressure probe improves by two orders of magnitude and the maximum frequency achievable with the current setup doubles that of sonic anemometers, it is still not possible to resolve the smallest turbulence scales present in the atmosphere. Nevertheless, the resolution achieved is enough to capture the most energetic scales of atmospheric turbulence.

2.2.2 Data processing

The objective of the data processing is the retrieval of the wind velocity vector in any stationary frame of reference. In the current case it will be a horizontal frame of reference fixed to the ground, which is the most commonly used in atmospheric science applications. The subscript **geo** will denote all variables that are relative to this geographical stationary frame of reference and the subscript **uav** will denote all those which are relative to the frame of reference fixed to the body of the UAV, which is in nature non-inertial.

The wind velocity vector is first measured by the pressure probe as a three-component time-dependent vector in the UAV frame of reference $\mathbf{u}_{\text{uav}}(t)$. The rotational velocity of the tip of the pressure probe is then added to the latter. This rotational velocity is calculated as the cross product of the UAV's angular velocity $\omega_{\text{uav}}(t)$ vector and the position vector from the center of mass of the UAV to the tip of the pressure probe \mathbf{r}_{uav} . The resultant is transformed into the geometrical frame of reference with the help of the rotation matrix $\mathbf{R}(t)$. This matrix is calculated using the Euler angles, which determine the attitude of the UAV, provided by the IMU. This method provides a singularity at an angle of attack of 90° , although this situation is extremely unlikely to happen. Finally, the translational velocity of the UAV in the geographical frame of reference $\mathbf{t}_{\text{geo}}(t)$ is added in order to retrieve the wind velocity vector relative to the ground $\mathbf{u}_{\text{geo}}(t)$.

The process described above can be mathematically expressed as follows:

$$\mathbf{u}_{\text{geo}}(t) = \underbrace{\mathbf{R}(t)}_{\text{rotation uav} \rightarrow \text{geo}} \left(\underbrace{\mathbf{u}_{\text{uav}}(t)}_{\text{measured velocity}} + \underbrace{\omega_{\text{uav}}(t) \times \mathbf{r}_{\text{uav}}}_{\text{probe rotational velocity}} \right) + \underbrace{\mathbf{t}_{\text{geo}}(t)}_{\text{translational velocity}} \quad (2.1)$$

and it is similar to the one described in Williams and Marcotte (2000).

2.3 Results

In this section we present the validation of the developed measurement technique against sonic anemometry, as well as an example of its capabilities by measuring the signature of tip vortices shed by the blades of a full-scale wind turbine.

2.3.1 Validation of the measurement technique

The ideal validation test would consist of a comparison of the proposed UAV-based technique and a perfectly accurate flow measurement technique able to measure time series of the wind speed vector and temperature at the same frequency and the same location of the UAV. However the UAV will always feature translation and rotation motion even in the case of hovering flight and low wind velocity. Since such a measurement technique does not exist, an alternative validation test as close as possible to the previous requirements is proposed: it consists of the comparison of the measurements of a sonic anemometer installed in a meteorological tower with the measurements of the UAV-based technique during a hovering flight. Two potential sources of disagreement for this validation test come from the fact that the flow measurements are not taken at the same exact same location in space, and that the spatial resolution of the pressure probe is approximately two orders of magnitude higher than that of the sonic anemometer. The first one has been minimized by flying as close as possible to the sonic anemometer and the second one by downsampling the pressure probe frequency to match that of the sonic anemometer (20 Hz in this case). They are both discussed in more detail below.

The validation of the proposed technique has been carried out with measurements of the UAV hovering at the same height as a Gill WindMaster 3D Sonic Anemometer and at a horizontal distance of approximately 5 m from it in the cross-wind direction in order to avoid any wake effect from one measurement technique on the other. The anemometer chosen is situated at a height of 25 m and is the highest of seven anemometers installed on a meteorological tower inside the campus of the École polytechnique fédérale de Lausanne (EPFL) as shown in figure 2.3. The tower is situated inside a patch of grass-covered ground south of a building of approximately 10 m in height.

The results from the validation tests are presented in table 2.2. All validation tests have been conducted on a sunny day with northerly winds since it is the least obstructed wind direction. A slight three-dimensional effect is expected due to the influence of the nearest building on the incoming flow. This effect will create a horizontal inhomogeneity of the flow and therefore a source of disagreement between the wind measured by the UAV and the sonic anemometer. This disagreement will be smallest for the highest of the sonic anemometers mounted on the tower (i.e. the one chosen for this validation), and diminish the closer the UAV is able to fly to the sonic anemometer without affecting its measurements. Since the stability of the UAV, even at high wind speeds, allows to hover and measure safely at distances from 3 m to 5 m horizontally and less than 50 cm vertically to the sonic anemometer, it has been

Chapter 2. Multirotor UAV-based platform for the measurement of atmospheric turbulence: validation and signature detection of tip vortices of wind turbine blades.

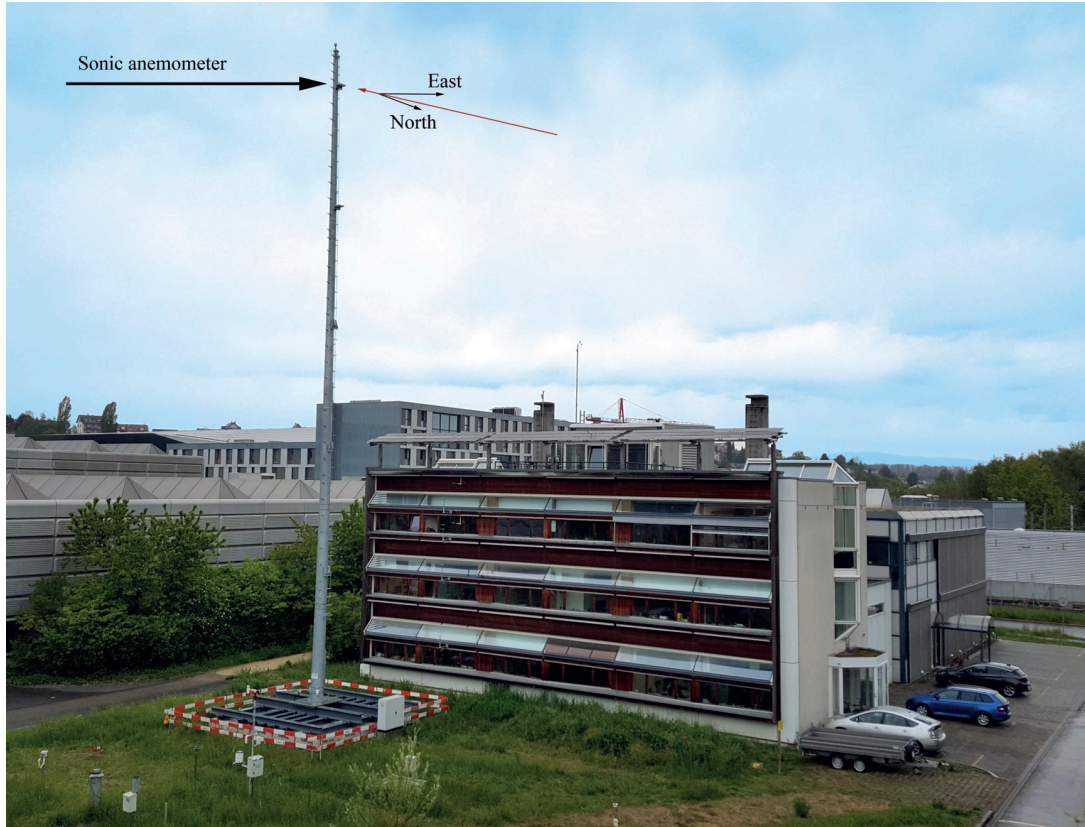


Figure 2.3 – Photographic view of the meteorological tower inside the EPFL campus. The red arrow represents the incoming wind direction during the tests. The sonic anemometer is located at 25 m height. The nearest building is 10 m high.

considered that the inhomogeneity of the flow has a negligible impact on our validation. This has been further proven by the good agreement between the measurements from the proposed technique and those from the sonic anemometer shown in this section.

The validation presented here consists in the comparison of some of the most important variables that characterize atmospheric turbulence measured by the proposed technique and the sonic anemometer. The four validation test cases correspond to different moments of the same day - morning and afternoon. The comparison of these four cases is shown in table 2.2, where u_{str} and v_{str} indicate, respectively, the streamwise and transversal components of the wind speed vector. It is worth noting that the duration of the tests is limited by the autonomy of the UAV, which diminishes with increasing wind speed, and that the high horizontal turbulence intensity levels are due to fact that the meteorological mast is located inside the campus and therefore surrounded by buildings.

The comparison of the flow statistics computed from the measurements shows a good general agreement between the proposed technique and the sonic anemometer for all variables presented. Average wind speeds measured by the proposed technique show consistently a

Table 2.2 – Comparison of flow statistics obtained with the UAV platform and a sonic anemometer at a height of 25 m over the EPFL campus.

	Test 1		Test 2		Test 3		Test 4	
	UAV	Anem	UAV	Anem	UAV	Anem	UAV	Anem
duration [s]	500	500	500	500	600	600	720	720
\bar{u}_{str} [ms^{-1}]	8.8	9.1	8.0	8.2	6.8	7.1	6.4	6.6
$\sigma(u_{str})$ [ms^{-1}]	2.44	2.60	2.65	2.73	2.81	3.08	1.87	2.10
$\sigma(v_{str})$ [ms^{-1}]	2.19	2.07	2.14	2.12	1.74	1.72	1.92	1.93
\bar{w} [ms^{-1}]	0.08	0.12	0.37	0.29	0.37	0.03	0.15	0.17
$\sigma(w)$ [ms^{-1}]	1.41	1.37	1.47	1.36	1.33	1.22	1.28	1.23
$\overline{u'_{str}w'}$ [m^2s^{-2}]	-1.18	-1.34	-1.60	-1.49	-1.64	-1.65	-0.72	-0.70
\overline{dir} [$^\circ$]	23.8	20.2	19.8	20.5	13.8	16.9	15.7	13.8
$\sigma(dir)$ [$^\circ$]	15.3	14.8	17.0	17.0	16.8	17.4	17.1	17.1
\bar{T} [$^\circ\text{C}$]	13.9	14.5	12.4	13.0	14.6	14.9	14.5	14.9
$\overline{w'T'}$ [mKs^{-1}]	0.19	0.17	0.11	0.18	0.28	0.21	0.11	0.12

slightly lower u_{str} in terms of average -between 2 and 4%- and standard deviation -between 3 and 10%. The temperature shown by the thermocouple shows a bias of approximately 0.5°C , which lies within the accuracy of $\pm 2^\circ\text{C}$ given by the manufacturer of the sonic anemometer used. The agreement in terms of vertical turbulent fluxes of streamwise momentum ($\overline{u'_{str}w'}$) and heat ($\overline{w'T'}$) is very good considering the difficulty of the calculation of these quantities with the proposed technique. It must be noted that small errors in the measurement of the instantaneous fluctuations of temperature T' , streamwise wind speed u'_{str} and especially vertical wind speed w' , together with the synchronization of the wind speed and temperature, can lead to large differences in these turbulence quantities. Differences of similar nature and quantity can be found in [Mauder and Zeeman \(2018\)](#) when comparing the measurements of friction velocity and buoyancy flux from different anemometer systems, among which, the sonic anemometer used for this study.

Despite the differences mentioned above, the technique is able to capture with a good degree of accuracy the characteristics of evolving atmospheric conditions during a sunny day. These include higher turbulence intensity and momentum and heat fluxes during the middle of the day, when the solar radiation heats up the ground and enhances turbulent mixing (tests 2 and 3), and lower values at the beginning of the morning and the end of the afternoon (tests 1 and 4).

As discussed before, a perfect time series comparison will never be possible due to the inherent

Chapter 2. Multirotor UAV-based platform for the measurement of atmospheric turbulence: validation and signature detection of tip vortices of wind turbine blades.

sources of disagreement between both techniques discussed above, but an example is still pertinent and illustrative. Figure 2.4 shows an example of the first 300 s of the variables measured by the IMU unit and that are used in the wind speed retrieval in the geographical frame of reference for test 1 shown in table 2.2. The angular velocities show high frequency components due to the speed of the control system of the UAV and the corrections in attitude needed for a stable hovering flight in a highly turbulent environment. The amplitude of the angular velocities rarely exceeds 0.25 ms^{-1} and it is highest for the roll angular velocity and smaller for the pitch and yaw. The distance from the pressure probe position is 3 cm to the roll axis and 115 cm to the pitch and yaw axis. Therefore the roll angular velocity introduces minimal angular velocity corrections. In this case the pitch and yaw angular velocity corrections rarely exceed 0.2 ms^{-1} .

The Euler angles show much lower frequency components and can be easily linked to the three components of the velocity vector of the wind for a hovering flight. Since the UAV was aligned with the wind direction for all tests, the roll shows an average of zero while the pitch is positive.

The translation velocities of the UAV for this highly turbulent case oscillate normally in the range $\pm 1 \text{ ms}^{-1}$ with peaks around $\pm 2 \text{ ms}^{-1}$. The barometric control makes the UAV more reactive to minor changes in altitude and limits the vertical velocity values as well as height changes to $\pm 0.5 \text{ m}$ while the maximum horizontal displacement is limited to a radius of 2.5 m for these wind conditions.

Figure 2.5 shows a comparison in terms of wind speed and temperature between the sonic anemometer and the proposed UAV-based technique for the first 300 s of test 1 presented in table 2.2 and corresponds to the IMU measurements of figure 2.4. Due to the slightly different spatial location of both instruments, the agreement of both measurements is better when bigger structures dominate the flow, although the agreement is still good for time scales as small as one second. It is also visible here the bias of the temperature discussed before.

Figure 2.6 shows the comparison of both techniques for test 1 presented in table 2.2 in terms of spectra of the streamwise and vertical components of the wind velocity vector, the temperature and the cospectra of vertical velocity and temperature. The spectra have been computed using Hanning windows of 30 s and 50% overlapping. The figure shows good agreement between both techniques. The spectra of the velocity components show the characteristic $-5/3$ slope of the inertial subrange of atmospheric turbulence. The spectra of temperature and $w'T'$ shows that the sonic anemometer presents a faster response at higher frequencies. Nevertheless, the contribution of the bigger scales or lower frequencies to the total vertical turbulent transport of heat is the determining factor, as proved by the agreement of the statistics shown in table 2.2. The rest of the test periods show similar levels of agreement in terms of time series and spectra.

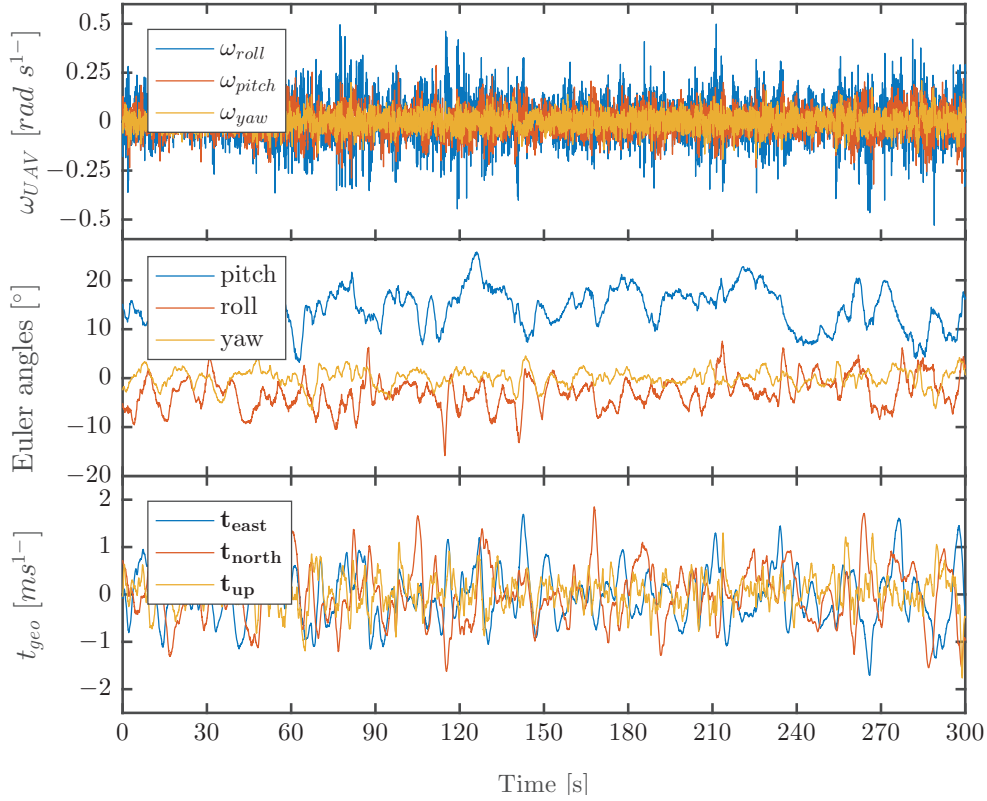


Figure 2.4 – Example of time series of the IMU variables used for the retrieval of the wind velocity in the geographical fixed frame of reference, as explained in equation 2.1 and in section 2.2. The variables shown correspond to test 1 of table 2.2 and figure 2.5. Top: angular velocity of the UAV in its frame of reference; center: Euler angles in the geographical frame of reference; bottom: translation velocity of the UAV in the geographical frame of reference.

2.3.2 Wind turbine blade tip-vortex signature detection

As discussed already, the proposed technique is particularly useful when measuring turbulence and flow characteristics where it is not possible to place sonic anemometers or other standard sensors used in atmospheric sciences. Furthermore, its high spatial and temporal resolution opens new possibilities for the study of small and fast flow features in the atmosphere. The objective of this section is to illustrate the capabilities of the technique in such cases, and one particularly suitable example is the detection the signature of tip vortices shed by full-scale wind turbine blades. Due to the highly dynamic nature of these vortices, their advection velocity and their relatively small size, their characterization requires an accurate measurement of the three components of the wind velocity vector at a high temporal resolution and close to the rotor of the wind turbine, where the installation of a meteorological mast is not possible. To our knowledge, the only example of measurements of near-wake full-scale wind turbine vortices in the literature has been performed by [Subramanian et al. \(2016\)](#).

Chapter 2. Multirotor UAV-based platform for the measurement of atmospheric turbulence: validation and signature detection of tip vortices of wind turbine blades.

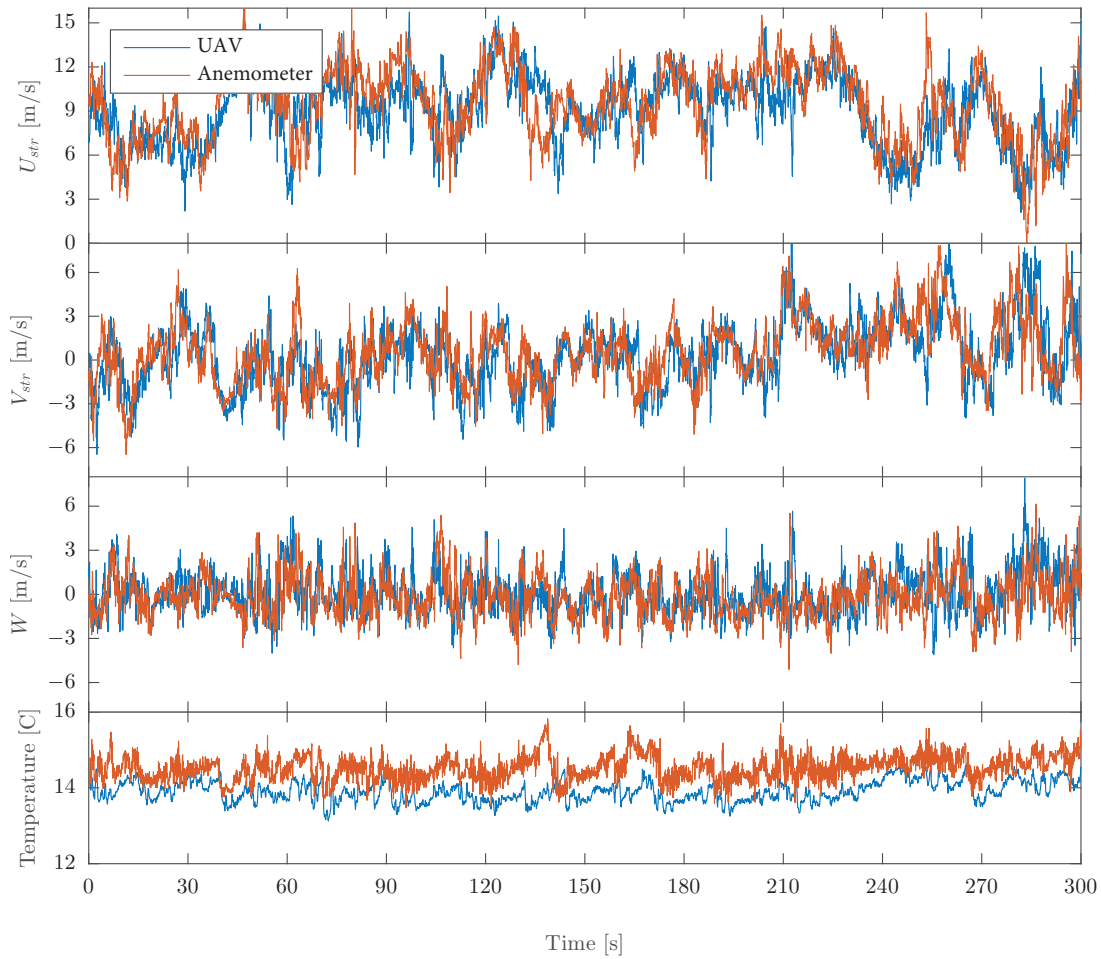


Figure 2.5 – Comparison of wind speed and temperature time series of the sonic anemometer and the UAV-based technique for the first 300 s of test 1 presented in table 2.2. The UAV-based measurements have been downsampled to match the 20 Hz frequency of the sonic anemometer.

The measurements shown in this section have been carried out around a 2.3 MW Enercon E-70 wind turbine situated between the villages of Collonges and Dorénaz, in the canton of Valais in Switzerland. This turbine features a hub height of 98 m and a rotor diameter of 71 m. The wind turbine is situated in a 13 km long, 2000 m deep and 1 km wide straight section of the Rhone valley. This valley section presents a flat bottom covered with agricultural crops. Due to the particular orography of the valley, the dominant winds are clearly bi-directional (northerly or southerly wind) and thermally-driven. The measurements were carried during a northerly wind period. An aerial view of the section of the valley and the situation of the wind turbine is shown in figure 2.7.

The inflow has been characterized with two UAV flights at 3 diameters upstream of the wind turbine rotor. The first one consisted of a hovering flight, similar to any of the validation

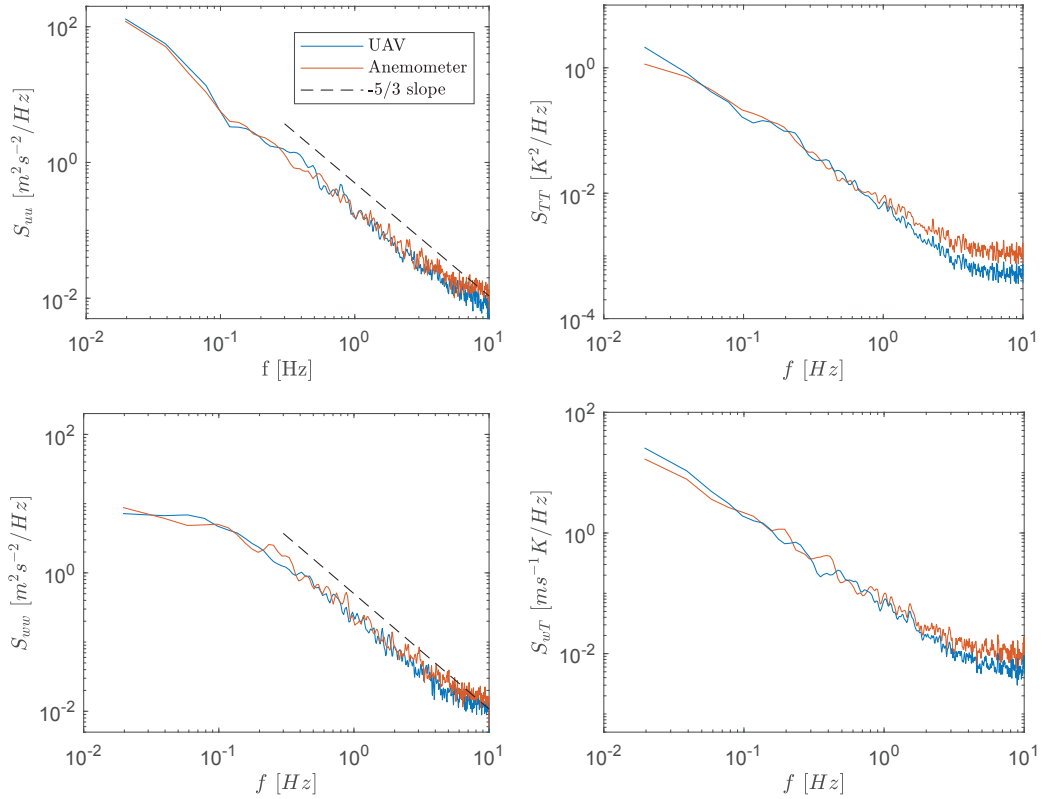


Figure 2.6 – Spectra of the streamwise and vertical wind velocity components, the temperature and $w'T'$. The sonic anemometer and the UAV platform results are shown for the test 1, whose statistics are presented in Table 2.2. The spectrum has been computed using Hanning windows of 30 s and 50% overlapping. The UAV-based measurements have been downsampled to match the 20 Hz frequency of the sonic anemometer.

tests, dedicated to the measurement of the incoming wind flow statistics at hub height, and the second flight was dedicated to an estimation of the wind shear in front of the wind turbine. These two flights were performed 40 and 20 minutes, respectively, before the tip vortex measurements. As a consequence, they cannot be considered as actual measurements of the inflow at the time of the measurements, but rather an indication of the overall flow conditions during the test since the evolution of the ABL is not expected to change significantly in such a period of time. A further indication of the steadiness of the ABL is the fact that the wind turbine supervisory control and data acquisition (SCADA) system shows constant wind speed and power throughout the whole test. All measurements were taken between 4 and 5 pm on April 12, 2017 (local time).

The hovering flight had a duration of 5 minutes and measured an average horizontal wind speed of 8.1 ms^{-1} and longitudinal, transversal and vertical turbulence intensities of 11.6%,

Chapter 2. Multirotor UAV-based platform for the measurement of atmospheric turbulence: validation and signature detection of tip vortices of wind turbine blades.



Figure 2.7 – Perspective view of the flat section of the Rhone valley in which the E-70 wind turbine is located ($46^{\circ}09'35''\text{N } 7^{\circ}02'14''\text{E}$), as well as the villages of Collonges and Dorénaz. Map data: Google, DigitalGlobe.

7.8% and 7.0% respectively. The average temperature measured was 14.2°C and the vertical turbulent transport of heat 0.03 mKs^{-1} . This indicates a near-neutral thermal stability of the boundary layer, which is expected at this time of the day during the month of April.

The second flight consisted in a vertical ascent-descent trajectory over 8 minutes from 25 to 170 m effectively covering the rotor height. When plotting the streamwise wind speed, the wind direction and the virtual potential temperature against the height for this flight (see figure 2.8) one can get relevant information about the ABL. As mentioned before, this approximation is only consistent if the flow is reasonably steady during the flight. The shear, veer and atmospheric stability of the ABL are not expected to play a significant role on the signature of blade tip vortices at very short distances from the rotor disk; nevertheless, it can be concluded that figure 2.8 gives an indication that the wind speed, direction and virtual potential temperature across the rotor disk are close to constant, minimizing the aforementioned effects on this study.

The blade tip vortex detection flight consisted of a hovering flight carried out at hub height and at the right extremity of the rotor disk when looking from behind, and at a downstream

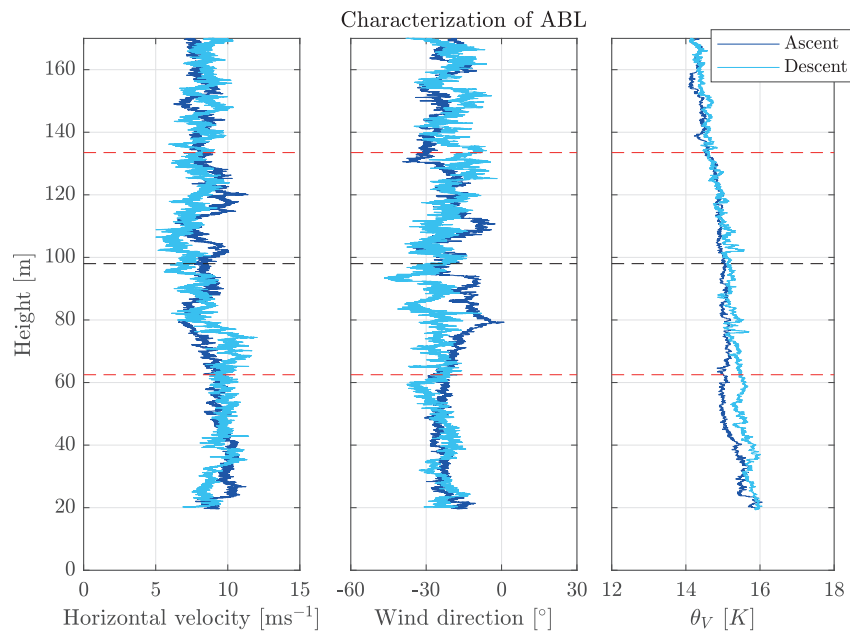


Figure 2.8 – Horizontal wind speed, wind direction and virtual potential temperature measured during an ascent-descent flight three rotor diameters upstream of the wind turbine. The dark blue and light blue lines present, respectively, the data obtained during the ascent and descent flights. The black dashed line represents the wind turbine hub height and the red dashed lines the upper and lower limits of the turbine rotor. The ABL shows small variations of all variables across the rotor disk during the tests.

distance of approximately 35 m from the rotor (half a diameter). It is important to note that the sense of rotation of the wind turbine (as in all commercial utility-scale wind turbines) is counterclockwise when looking from downstream, which means that at the right extremity, the blade tip moves upwards. The axis of rotation of the tip vortices shed by the wind turbine blades at the point where the measurements were taken should be vertical and their sense of rotation clockwise when looking from above. The measurement frequency used for the vortex signature detection is 50 Hz.

The dynamic nature of full-scale blade tip vortices and their relatively small size makes difficult its detection with a point-wise measurement instrument even when the latter is easy to position at any point in space. The trajectory of the vortices is greatly affected by, among other factors, transversal atmospheric turbulence and even minor changes in the wind turbine yaw, which occur constantly in full-scale wind turbines. Therefore the center of the vortices will not pass through exactly the same position in space every time. The transversal dispersion of vortex centers increases with the longitudinal distance, making more difficult, although still perfectly possible, their detection further downstream as shown by [Grant et al. \(2000\)](#).

During the hovering flight carried out, it has been possible to detect the signature of many

Chapter 2. Multirotor UAV-based platform for the measurement of atmospheric turbulence: validation and signature detection of tip vortices of wind turbine blades.

tip vortices. Due to the lateral or transversal dispersion of the vortex centers, the signature of each of them is different, but two particularly illustrative cases of vortex pairs have been selected to showcase the potential of the developed technique. They consist of vortex pairs that are aligned with the wind direction (in line) and vortex pairs that have been laterally displaced with respect to the wind direction (out of line). Two very similar vortex pairs have been isolated for both the in-line and out-of-line cases and they are presented in figure 2.9.

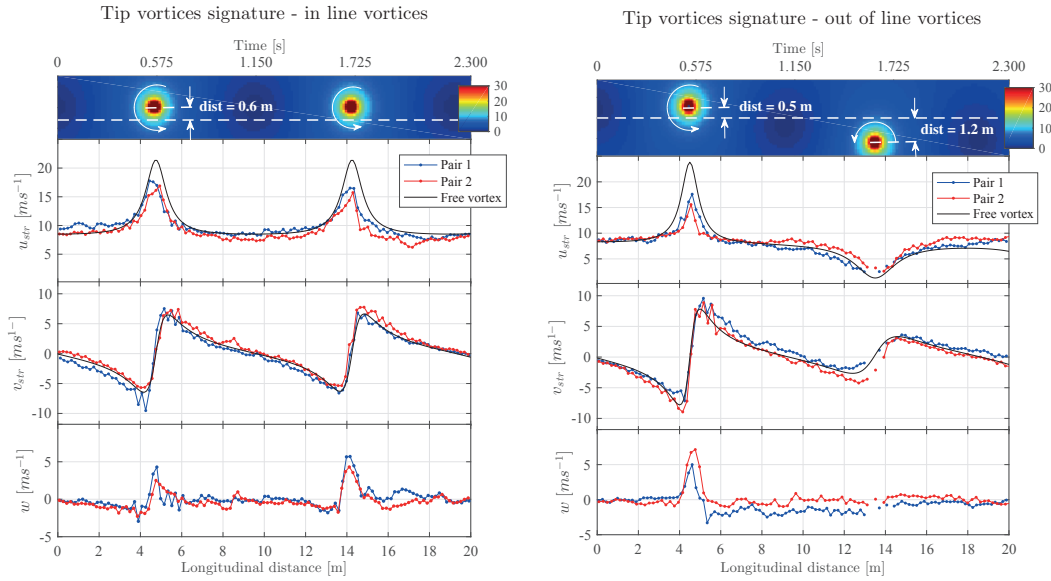


Figure 2.9 – Signature of detected tip vortex pairs. Top: tangential velocity in ms^{-1} of two consecutive 2D free vortices separated approximately 9 m in the longitudinal direction and with a strength $\Gamma = 50 \text{ m}^2\text{s}^{-1}$. Their lateral distance to the measurement point (long dashed white line) is indicated. Bottom: velocity components of the vortex pairs measured together with the signature of the 2D free vortices depicted on the top part. Taylor’s frozen approximation has been used in order to convert time series to spatial measurements.

Figure 2.9 shows in dotted blue and red lines the time series of the three components of the velocity vector of the in-line and out-of-line vortex pairs. The time series of the velocity components have been converted into space using Taylor’s frozen turbulence approximation with an advection velocity corresponding to the free-stream velocity at hub height indicated by the SCADA data of the wind turbine.

The distance in time between consecutive vortices is 1.15 s, which corresponds to the blade passage period, or one third of the wind turbine rotation period. The wind turbine rotation speed during the measurements was 23 rpm. When converting this period to space using Taylor’s hypothesis the separation between vortices results in approximately 9 m.

The time series of the transversal velocity v_{str} shows an undulating behavior that can be well approximated by free or potential two-dimensional vortices of strength $\Gamma = 50 \text{ m}^2\text{s}^{-1}$ at different lateral distances from the measurement point (dashed white line in the figure).

The approximation of the signature of turbine blade tip vortices to that of a two-dimensional free vortex has been common in the past as shown by [Vermeer \(2001\)](#). For the case of in-line vortices the distance is 0.6 m to the right and for the out-of-line vortices the distances are 0.5 m to the right and 1.2 m to the left of the measurement point. The signature of the free vortices is shown as a continuous black line for the longitudinal and transversal components.

The effect of the vortex induction in the transversal velocity v_{str} is the same regardless of the side in which the vortices are found. In contrast, the effect in the longitudinal velocity u_{str} shows as either a sudden increase or a sudden decrease when the vortex core passes close to the sensor, similar to what has been shown in wind tunnel measurements by [Vermeer \(1994\)](#) and [Mast et al. \(2004\)](#).

The signature of the longitudinal velocity component agrees well with the measurements except when the core is very close to the measurement point. The velocity is lower than that of a two-dimensional free vortex exactly where the axial (vertical) velocity component w shows positive values. This is probably an indication of axial velocity in the vortex core in the same direction as the rotation of the blade caused to the viscous drag of the latter. This effect has been noticed by [Lignarolo et al. \(2014a\)](#) using phase-locking averaging analysis on their PIV measurements of near-wake flow of a two-bladed wind turbine in a wind tunnel.

When vortices pass to the left of the fast pressure measurement sensor, the reduction in the longitudinal velocity component and the increase in the transversal one causes an increase of the relative angle between the velocity vector and the pressure probe. This can result in the velocity vector escaping the acceptance cone of $\pm 45^\circ$ and therefore not providing any readings for a brief period of time. This can be seen in the out-of-line vortex signature example.

2.4 Summary

The measurement technique presented in this study consists of a multirotor UAV platform capable of hovering flight and carrying a series of instruments that allow the measurement of time series of the three components of the velocity vector and the air temperature with a high accuracy and at a high spatial and temporal resolution. The main advantage of using a hovering-capable UAV platform is the flexibility to measure at points in space where it is difficult or impossible to place meteorological towers with standard equipment such as cup or sonic anemometers.

The main component of the new measurement technique is a multihole fast pressure probe sensor that measures the velocity vector relative to the UAV platform, which is a non-inertial frame of reference. The addition of a 3-axis gyroscope, accelerometer and magnetometer as well as a GPS, allows for the reconstruction of the velocity vector relative to a fixed frame of reference (commonly a geographical frame of reference).

The technique has been validated against sonic anemometry for the most relevant flow statis-

Chapter 2. Multirotor UAV-based platform for the measurement of atmospheric turbulence: validation and signature detection of tip vortices of wind turbine blades.

tics in atmospheric turbulence studies. The test cases presented have shown good agreement in terms of average wind speed and direction, turbulence intensity and other particularly difficult to measure quantities such as vertical turbulent fluxes of momentum and heat.

The capabilities of the technique to measure complex flow phenomena is illustrated with the example of the detection of the signature of blade tip vortices in the near wake of a full-scale wind turbine. The accuracy is comparable to that of a sonic anemometer while featuring a higher temporal and spatial resolution that allows to resolve the signature of the vortices in terms of the three components of the velocity vector. The signature of the tip vortices agrees with previous studies carried out in the wind tunnel with other techniques such as PIV and LDV.

3 3D turbulence measurements using three synchronous wind lidars: validation against sonic anemometry¹

Abstract

This paper presents a technique to measure time series of the three components of the wind vector at a point in space from synchronous measurements of three scanning Doppler wind lidars. Knowing the position of each lidar on the ground and the orientation of each laser beam allows to reconstruct the three components of the wind velocity vector. The laser beams must intersect at the desired point in space and their directions must be non-coplanar so that trigonometric relationships allow the reconstruction of the velocity vector in any coordinate system.

This technique has been tested during a measurement campaign carried out at Cabauw's experimental site for atmospheric research (CESAR) in the Netherlands and compared against measurements from sonic anemometers installed in a meteorological mast. The spatial resolutions of both measurement techniques differ by one order of magnitude. Therefore, in order to properly compare the results, a pseudo-spatial filter which mimics the attenuation induced by the lidar technology at small scales of turbulence has been applied to the velocity time series provided by the sonic anemometer.

Good agreement between both measurement systems is found in terms of the measured instantaneous velocity vector, turbulence statistics, Reynolds stresses and the spectra of the three components of the velocity and the turbulent kinetic energy. These results provide a successful validation of the proposed technique.

¹The contents of this chapter are published in: F. Carbajo Fuertes, G.V. Iungo and F. Porté-Agel. 3D turbulence measurements using three synchronous wind LiDARs: validation against sonic anemometry. *Journal of Atmospheric and Oceanic Technology*, 31:1549-1556, 2014.

3.1 Introduction

Researchers and industry in the fields of wind engineering and meteorology demand extensive and accurate measurements of atmospheric boundary layer turbulence for a better understanding of its role in a wide range of onshore and offshore applications: wind resource evaluation, wind turbine wakes, weather forecast, pollutant transport, urban climate studies, etc. Remote sensing techniques, and especially light detection and ranging (lidar) technologies are becoming increasingly popular for the study of atmospheric flow due to their flexibility regarding transportation, installation and operation in any type of terrain when compared to traditional meteorological masts.

Single and dual-lidar techniques have already been successfully used to reconstruct two or three-component wind velocity fields inside a planar or volumetric domain for a diverse range of applications, as in [Newsom and Banta \(2004\)](#), [Newsom et al. \(2005\)](#), [Drechsel et al. \(2010\)](#), [Hill et al. \(2010\)](#) or [Kongara et al. \(2012\)](#), and more specifically in the field of wind turbine wake measurements by [Bingöl et al. \(2010\)](#), [Trujillo et al. \(2011\)](#) and [Jungo et al. \(2013a\)](#). Especially relevant in the field of turbulence measurement with lidars is the recent work of [Mann et al. \(2010\)](#), [Sathe et al. \(2011\)](#), [Sathe and Mann \(2012\)](#), [Angelou et al. \(2012\)](#), in which different difficulties associated to the measurement of atmospheric turbulence with a single lidar are discussed.

Nevertheless, up to this day, the use of three synchronous Doppler lidars with intersecting beams (hereinafter, triple-lidar technique) seems to be the only viable approach to accurately provide time series of the three components of the velocity vector at a point in space so that turbulence statistics such as *TKE*, turbulent stresses and velocity spectra can be calculated ([Mann et al., 2008](#)).

3.2 Experimental set-up

The measurements presented in this study were carried out during the month of December 2012 in Cabauw, the Netherlands.

3.2.1 CESAR observatory and meteorological mast

The Cabauw Experimental Site for Atmospheric Research (CESAR) observatory is located in the province of Utrecht (the Netherlands) in a polder 0.7 m below mean sea level. The surrounding terrain can be considered as flat and mainly covered with grass. This experimental site is equipped with a large set of instruments for the study of the atmosphere and its interaction with the land surface. Their publicly available databases provide not only turbulence measurements, but also many other relevant data like radiation, cloud height and precipitation, which were used to assess the quality of the sonic anemometer and lidar measurements.

The central element of the research site is a 213 m tall meteorological mast. The mast is a

closed cylinder of 2 m diameter which is guyed at four levels. Equipment is mainly placed on 9.4 m long booms that point out horizontally from the mast at three different directions (10°, 130° and 250° from North direction) every 20 m in height. Gill R3 sonic anemometers measuring 3D turbulence at a frequency of 10 Hz are available in the booms situated at 60, 100 and 180 m that point towards 130° direction. The booms are long enough to reduce flow interference by the mast to about 1% at the upwind side. The boom construction itself also disturbs airflow, therefore the actual sensor is placed at least 0.8 m above the slender boom end in order to get flow deviations which are routinely corrected, to $\pm 1\%$ for velocity and $\pm 1\%$ for wind direction (Wyngaard, 1981).

More information about the site, the meteorological mast and the instrumentation can be found in Ulden and Wieringa (1996) and Verkaik and Holtslag (2007).

3.2.2 LiDAR system

Wind velocity measurements were performed using three StreamLine lidars, manufactured by Halo Photonics. These instruments are infrared pulsed Doppler wind lidars which emit wave trains with a wavelength of 1.5 μm and a frequency of 15 kHz. They measure the velocity component parallel to the laser beam direction, which is denoted as line-of-sight or radial velocity, with a resolution of 3.82 cm s^{-1} . The laser beam can be oriented towards any direction thanks to a steerable head. A pulsed wind Doppler lidar measures an average of the radial velocity along a series of equidistant gates whose length can be adjusted at will. An important characteristic of this system is its high spatial resolution; the gates can be shortened to a minimum length of 18 m. The minimum distance at which measurements are available is 45 m and its maximum range can be extended to about 3 km depending on aerosol concentration. The maximum sampling frequency is 0.77 Hz.

3.2.3 Positioning system

Relative positions between the mast and each lidar have been determined using a Topcon's GRS-1 GPS receiver. The declared precision is 30 cm working in differential GPS (DGPS) network, but in practice the uncertainty in the position of each element has been noticed to be somewhat higher, probably around 1 m, and it varies depending on the number of satellites available at each time.

3.2.4 Configuration

The three lidars used are placed on the ground, equidistant to the sonic anemometer, forming an equilateral triangle. The lidar heads stare their respective beams so that they intersect as close as possible to the sonic anemometer situated at 60 m high with an approximate 45° elevation angle. The three laser beams form a sort of regular triangular pyramid-like configuration as shown in figure 3.1.

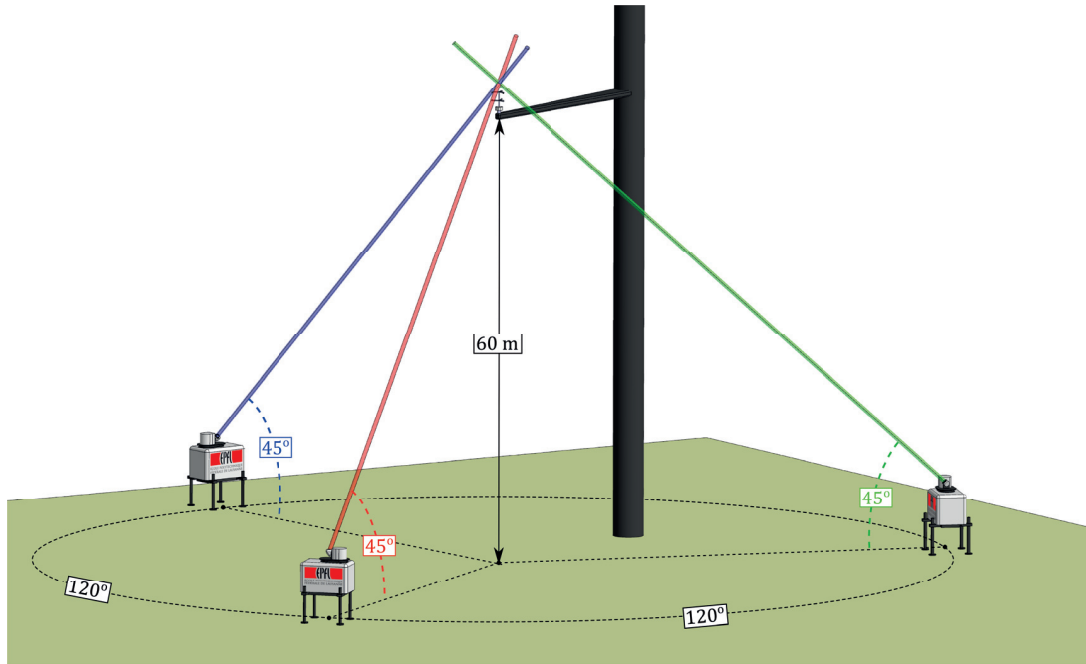


Figure 3.1 – Sketch of the configuration of the lidars, together with the meteorological mast and the sonic anemometer.

3.3 Technique and data analysis

The objective of this section is to explain the processing of the measurements of the three lidars in order to calculate the three components of the wind velocity and turbulence at a point in space, and the validation of this process by comparing these results to the measurements of a sonic anemometer.

3.3.1 The meteorological coordinate system and the transformation matrix

As mentioned before, a Doppler lidar provides a measurement of the component of the velocity parallel to the laser beam V_r , which can be mathematically expressed as the projection of the actual wind velocity vector \mathbf{V} in the direction of the laser beam \mathbf{n} :

$$V_r = \mathbf{V} \cdot \mathbf{n}. \quad (3.1)$$

A meteorological coordinate system is used in order to express the three components of the wind vector. These are U_m (towards East), V_m (towards North) and W_m (vertical, positive upwards). The direction of the laser beam can be expressed with two angles: the elevation θ -angle between the horizontal plane and the laser beam- and the azimuth φ -angle between the orthogonal projection of the beam direction on the horizontal plane and the North, e.g. North=0°, East=90° - as sketched in figure 3.2. Equation 3.1 for the first of the three lidars

becomes:

$$V_{r1} = U_m \cos(\theta_1) \sin(\varphi_1) + V_m \cos(\theta_1) \cos(\varphi_1) + W_m \sin(\theta_1). \quad (3.2)$$

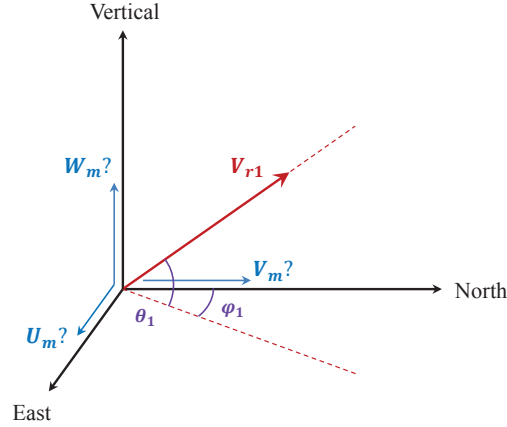


Figure 3.2 – Sketch of the meteorological coordinate system and an arbitrary radial velocity measured by a wind Doppler lidar

If the wind velocity vector is known, it can be projected on the lidar's beam direction, but a single lidar measurement is unable to reconstruct the three unknown components U_m , V_m and W_m . lidars number 2 and 3 provide the other two equations needed to calculate them. Expressing everything in matrix form yields:

$$\begin{bmatrix} V_{r1} \\ V_{r2} \\ V_{r3} \end{bmatrix} = \begin{bmatrix} \cos(\theta_1) \sin(\varphi_1) & \cos(\theta_1) \cos(\varphi_1) & \sin(\theta_1) \\ \cos(\theta_2) \sin(\varphi_2) & \cos(\theta_2) \cos(\varphi_2) & \sin(\theta_2) \\ \cos(\theta_3) \sin(\varphi_3) & \cos(\theta_3) \cos(\varphi_3) & \sin(\theta_3) \end{bmatrix} \begin{bmatrix} U_m \\ V_m \\ W_m \end{bmatrix}. \quad (3.3)$$

Equation 3.3 terms are: on the left hand side, the radial velocity measurements of the three lidars contained in vector \mathbf{V}_r and on the right hand side, the geometrical information in the transformation matrix \mathbf{M}_{tr} and the velocity vector in meteorological coordinates \mathbf{V}_m . Using this notation, the previous equation can be written as:

$$\mathbf{V}_r = \mathbf{M}_{tr} \mathbf{V}_m. \quad (3.4)$$

This equation projects the meteorological velocity vector into each lidar direction, allowing to check individually the deviations for each lidar. The inverse of the transformation matrix (denoted only as \mathbf{M}_{tr}^{-1} since its analytical form is cumbersome to express) allows the reconstruction of the meteorological velocity vector from the lidar measurements by:

$$\mathbf{V}_m = \mathbf{M}_{tr}^{-1} \mathbf{V}_r. \quad (3.5)$$

Equation 3.5 calculates the wind velocity vector \mathbf{V}_m as a simple vector-matrix multiplication

Chapter 3. 3D turbulence measurements using three synchronous wind lidars: validation against sonic anemometry

providing that the three lidars perform synchronous measurements and the laser beams are intersecting and non-coplanar, otherwise the transformation matrix \mathbf{M}_{lr} becomes non-invertible and the wind velocity vector \mathbf{V}_m cannot be reconstructed.

By analyzing equations 3.3 and 3.5, it becomes straightforward that the error sources for the geometrical reconstruction are the measured radial velocities V_{r_i} and the orientation angles of each lidar θ_i and φ_i . It should be noted that the inversion of the transformation matrix \mathbf{M}_{lr}^{-1} and its multiplication by the radial velocity vector \mathbf{V}_r will have the effect of propagating any of the aforementioned error sources to all the three components of the velocity vector in meteorological coordinates U_m , V_m and W_m .

3.3.2 Comparison with sonic anemometry

Spatial and temporal resolution of sonic anemometers normally ranges from 10 to 30 cm and from 10 to 100 Hz, respectively. The spatial resolution and the sampling frequency for the lidar measurements have been set to 18 m and 0.5 Hz respectively. Therefore, it is important to correctly filter and downsample the sonic anemometer data in order to be directly comparable to the lidar measurements.

Given the spatial weighting function of the lidar system $\beta(r)$, the velocity measured by a single lidar inside an arbitrary gate at a given instant can be expressed as:

$$V_{r\text{ lidar}} = \int_{-L/2}^{L/2} \mathbf{V}((D+r)\mathbf{n}) \cdot \mathbf{n} \beta(r) dr, \quad (3.6)$$

in which \mathbf{V} is the wind velocity vector field, \mathbf{n} is the unit vector in the direction of the laser beam, L is the length of the gate, D is the distance from the lidar to the gate center and r represents a distance from the gate center along the laser beam direction.

The reconstruction of the three components of the velocity vector is obtained from a combination of three one-dimensional convolutions (equation 3.6) corresponding to the three lidars, which is difficult to deal with. Therefore, a single three-dimensional convolution window $\psi(r)$ has been used to substitute the effect of combining three one-dimensional convolutions and the uncertainty in the position of the lidars, δ . In practice $\psi(r)$ treats the three lidars as a single system and therefore assumes a single spherical measuring volume of diameter $L + 2\delta$ represented by a Gaussian convolution window:

$$\psi(r) = e^{-\frac{1}{2} \left(2.5 \frac{r}{L+2\delta} \right)^2}, \quad (3.7)$$

where r is the distance from the center of the window, i.e. the point where the laser beams intersect. Then, the spatial filtering induced by the triple-lidar technique can be expressed as:

$$\mathbf{V}_{\text{lidar}} = \int_{-(L+2\delta)/2}^{(L+2\delta)/2} \int_0^{2\pi} \int_0^{\pi/2} \mathbf{V}(\mathbf{R} + \mathbf{r}) \psi(r) dr d\varphi d\theta, \quad (3.8)$$

where \mathbf{R} indicates the position of the center of the Gaussian convolution window and \mathbf{r} is a vector with origin in the center of the same window expressed in spherical coordinates r , φ and θ .

Currently there is not such a measurement technique that allows an instantaneous measurement of the wind velocity vector field \mathbf{V} in three dimensions inside a sphere of ~ 20 m diameter with an acceptable resolution -at least one order of magnitude smaller than the lidar resolution- that would allow the calculation of the three-dimensional convolution proposed in equation 3.8. Therefore, two more assumptions are used: flow homogeneity inside the spherical domain where the laser beams cross and Taylor's hypothesis. This allows the three dimensional Gaussian convolution window in space to become a single Gaussian convolution window in time. Then the measurements from a single sonic anemometer can be convolved to be directly comparable to the triple-lidar technique by:

$$\mathbf{V}_{lidar}(t) \approx \mathbf{V}_{Sonic, filt}(t) = \int_{-(L+2\delta)/(2\bar{U}_h)}^{(L+2\delta)/(2\bar{U}_h)} \mathbf{V}_{Sonic}(t + \tau) \psi(t) d\tau, \quad (3.9)$$

where $t = r/\bar{U}_h$. Equation 3.9 is in fact a pseudo-spatial filtering (time filtering in practice) of the sonic data. This process is sketched in figure 3.3.

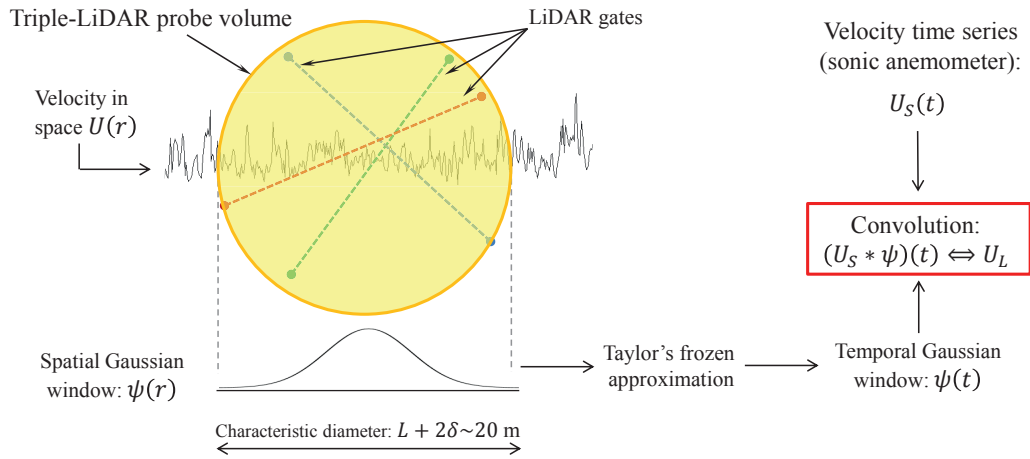


Figure 3.3 – Graphical concept of the pseudo-spatial filtering applied one of the velocity components measured by the sonic anemometer

3.4 Results

The triple-lidar technique described above has been used to measure remotely the wind velocity close to a sonic anemometer installed in Cabauw's meteorological mast at a height of 60 m on the 14 December 2012 from 00 to 01 UTC+1. Wind direction during the test oscillated between 120° and 150° guaranteeing no flow perturbation of the incoming wind by the mast (see section 3.2). The three components of the velocity vector have been calculated

Chapter 3. 3D turbulence measurements using three synchronous wind lidars: validation against sonic anemometry

in meteorological coordinates U_m , V_m and W_m first. Then the horizontal components have been transformed to streamline coordinates longitudinal U_{str} and transversal V_{str} by a simple rotation using the average wind direction measured by the sonic anemometer.

3.4.1 Instantaneous velocity vector

Figure 3.4 presents a comparison of the three components of the wind velocity vector in time measured by the sonic anemometer and the triple-lidar technique. The unfiltered sonic signal shows higher variance due to its higher spatial and temporal resolution. Those measurements have been filtered as explained in the previous section and downsampled to match the sampling frequency of the lidars, 0.5 Hz. There is a good agreement between both techniques.

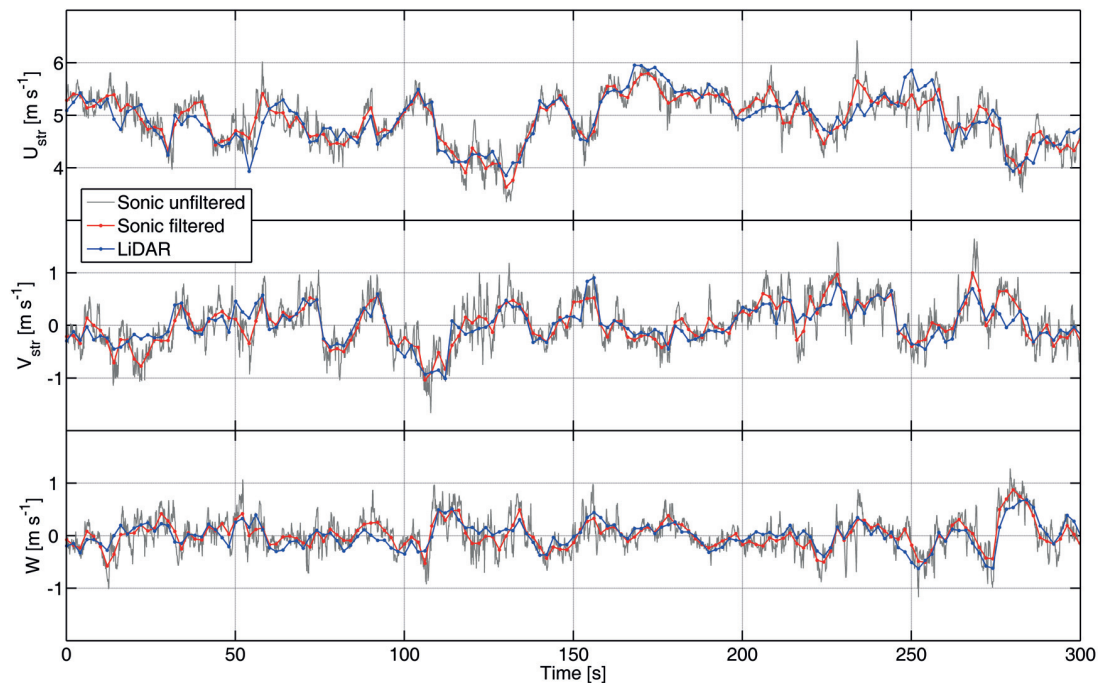


Figure 3.4 – Example of the reconstructed components of the velocity vector in streamwise coordinates with triple-lidar technique against filtered and unfiltered measurements by the sonic anemometer (only 5 minutes presented)

3.4.2 Turbulence statistics

The differences between the statistics calculated from the sonic and the lidar measurements are presented in table 3.1. Differences between sonic and lidar averages in terms of wind velocity or direction are very small, below the velocity resolution of the lidar system, 3.8 cm s^{-1} . This is possible if there is no bias in the measurements and the velocity fluctuations are bigger than the lidar resolution itself.

Averages				
	Sonic filtered & unfiltered	lidar	Difference	
\overline{U}_{str} [m s ⁻¹]	5.03	5.06	0.03	
\overline{V}_{str} [m s ⁻¹]	0.00	0.01	0.01	
\overline{W} [m s ⁻¹]	0.02	0.02	0.00	
Wind direction [°]	135.34	134.32	-1.02	
Standard differences (instantaneous values)				
	Sonic filtered - lidar			
$SE U_{str}$ [m s ⁻¹]	0.17			
$SE V_{str}$ [m s ⁻¹]	0.13			
$SE W$ [m s ⁻¹]	0.09			
Wind direction [°]	1.64			
Turbulence intensities				
	Sonic unfiltered	Sonic filtered	lidar	Difference
$I_{U_{str}}$ [%]	10.3	9.6	9.9	0.3
$I_{V_{str}}$ [%]	8.3	6.9	5.9	-1.0
I_W [%]	6.3	4.8	4.7	-0.1
Other turbulence quantities				
	Sonic unfiltered	Sonic filtered	lidar	Difference
$\overline{u'v'}$ [m ² s ⁻²]	-0.0217	-0.0219	-0.0241	-0.0023
$\overline{v'w'}$ [m ² s ⁻²]	0.0351	0.0243	0.0177	-0.0066
$\overline{u'w'}$ [m ² s ⁻²]	-0.0431	-0.0396	-0.0515	-0.0119
TKE [m ² s ⁻²]	0.274	0.206	0.198	-0.008

Table 3.1 – Differences in statistics of wind speed and direction between the sonic anemometer measurements and the lidar technique proposed. Note that the differences calculated are always between the filtered sonic data and the lidar measurements.

The standard differences for the instantaneous velocity components and direction between the filtered sonic measurements and the lidar ones show also a good agreement. The standard errors are in the order of 0.1~0.2 m s⁻¹ for the velocities and less than 2° for the direction.

The turbulence intensities show that, as expected, the filter applied to the sonic measurements and the inherent spatial filter of the lidar technique attenuates the turbulence fluctuations for all three components of the velocity. There is good agreement between the turbulence intensities calculated using the filtered sonic measurements and the lidars, with a maximum of 1% underestimation in the transversal component V_{str} by the lidars. The rest of the turbulence quantities calculated agree well too, finding the biggest difference on the $\overline{u'w'}$ turbulent flux and the smallest on the TKE .

3.4.3 Turbulence spectra

Figure 3.5 shows the turbulence spectra for each velocity component as well as for the turbulent kinetic energy. It is possible to observe the anisotropy of the big scales of the flow and also the characteristic $-5/3$ slope of the inertial subrange at smaller scales. The unfiltered sonic anemometer measurements resolve several decades of the inertial subrange, whereas in this case the lidar spatial and temporal resolution covers only around one decade. This range might be slightly wider or narrower depending on several factors like, for instance, the mean advection velocity, the Reynolds number, the measurement height or the atmospheric stability.

The filtered sonic and lidar spectra agree very well for the whole range of frequencies and decay in the same manner for frequencies higher than 0.1 Hz. This indicates that the pseudo-spatial filtering performed on the sonic measurements mimics well the real behavior of the spatial filtering induced by the lidar technique for turbulence scales in the order of 20 m and less.

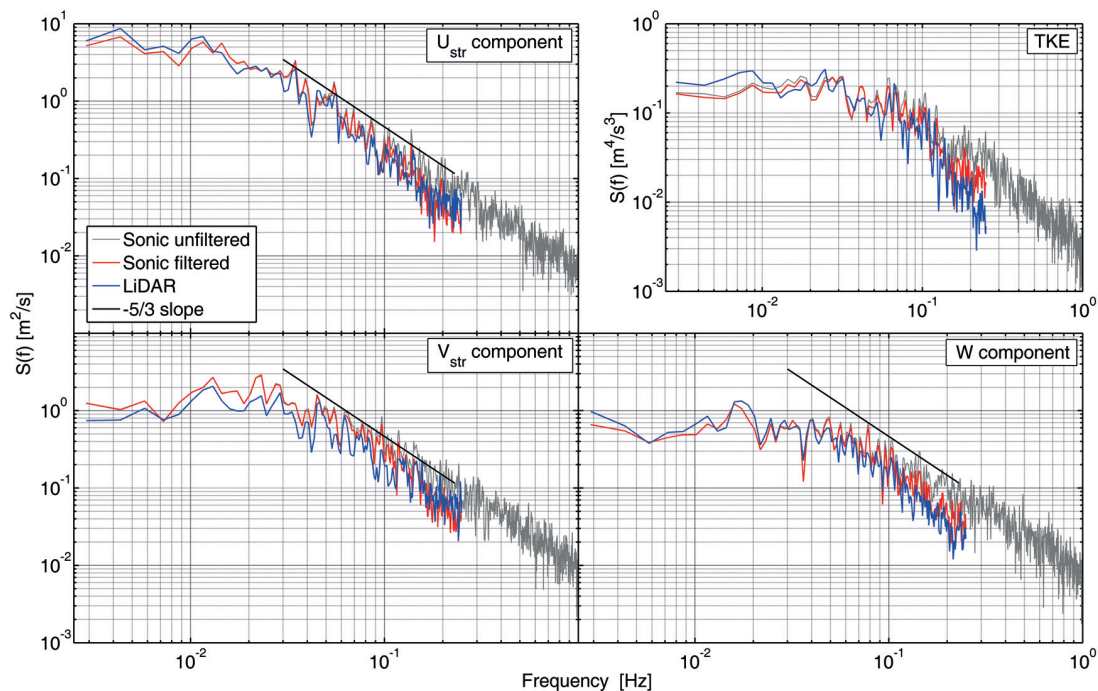


Figure 3.5 – Spectra of the longitudinal, transversal and vertical components of the wind velocity as well as turbulent kinetic energy measured with triple-lidar technique against filtered and unfiltered measurements by the sonic anemometer

3.5 Summary

The present work describes a technique for the measurement of the three components of the instantaneous wind velocity vector at a point in space. It is based on a trigonometrical reconstruction procedure applied to simultaneous measurements of three Doppler lidars

whose beams are intersecting.

The results of the technique have been compared to sonic anemometer measurements at a height of 60 m over flat terrain. Because of the different spatial and temporal resolutions of both measurement techniques, the sonic anemometer measurements have to be filtered and downsampled in order to be comparable to the lidar measurements for validation purposes. This is done via a convolution of the time series of the velocity measured by the sonic anemometer and a Gaussian spatial convolution window that represents the lidar attenuation of the turbulence at small scales. In order to apply properly this convolution, the spatial window is converted to a time window using Taylor's hypothesis and assuming flow homogeneity inside the measurement volume. The good agreement between both triple-lidar and sonic anemometer measurements in terms of averages, instantaneous values, different turbulent quantities as well as turbulence spectra provides a validation of the proposed technique.

4 Using a virtual lidar approach to assess the accuracy of the volumetric reconstruction of a wind turbine wake.¹

Abstract

Scanning Doppler lidars are the best tools for acquiring 3D velocity fields of full scale wind turbine wakes, whether the objective is a better understanding of some features of the wake or the validation of wake models. Since these lidars are based on the Doppler effect, a single scanning lidar normally relies on certain assumptions when estimating some components of the wind velocity vector. Furthermore, in order to reconstruct volumetric information, one needs to aggregate data, perform statistics on it and, most likely, interpolate to a convenient coordinate system, all of which introduce uncertainty in the measurements. This study simulates the performance of a virtual lidar performing stacked step-and-stare plan position indicator (PPI) scans on large-eddy simulation (LES) data, reconstructs the wake in terms of the average and the standard deviation of the longitudinal velocity component, and quantifies the errors. The variables included in the study are: the location of the lidar (ground-based and nacelle-mounted), different atmospheric conditions and varying scan speeds, which, in turn determine the angular resolution of the measurements. Testing different angular resolutions allows to find an optimum which balances the different error sources and minimizes the total error. An optimum angular resolution of 3° has been found to provide the best results. The errors found when reconstructing the average velocity are low (less than 2% of the freestream velocity at hub height), which indicates the possibility of high quality field measurements with an optimal angular resolution. The errors made when calculating the standard deviation are similar in magnitude, although higher in relative terms than for the mean, thus leading to a poorer quality estimation of the standard deviation. This holds true for the different inflow cases studied and for both ground-based and nacelle-mounted lidars.

¹The contents of this chapter are currently under review: F. Carbajo Fuertes and F. Porté-Agel. Using a virtual lidar approach to assess the accuracy of the volumetric reconstruction of a wind turbine wake. *Remote Sensing*.

4.1 Introduction

Wind power growth worldwide is a result of an ever increasing demand for renewable energy. With upper limits of rated power for single turbines reaching the order of 10 MW, the common solution to keep increasing the generated power is by installing a larger number of wind turbines. Due to space limitations, in most cases wind turbines are clustered together in wind farms and effectively this means higher number of turbines in each wind farm. In big wind farms, most of the wind turbines are affected by the wake flow of others, resulting in a reduction of incoming wind speed and an increase of turbulence (Vermeer et al., 2003). Therefore, a careful evaluation of the wind resource is needed for an accurate estimation of not only produced power from a future wind farm (Barthelmie et al., 2010; Hansen et al., 2012), but also the power losses and increased fatigue loads associated with the wind turbine wakes (Thomsen and Sørensen, 1999). Accurate wake models are needed to that end as well as to optimize the location of each of the wind turbines inside the farm in order to minimize the losses (Herbert-Acero et al., 2014; Gebraad et al., 2017).

There are a number of strategies to model the wake of a wind turbine: numerical models (Sørensen and Shen, 2002) discretize the Navier-Stokes (N.S.) equations, either in the physical space or the Fourier space, and solve them with the help of various turbulence models; analytical models (Bastankhah and Porté-Agel, 2014) use certain assumptions (e.g. the shape of the wind velocity deficit in the wake) and combine them with the N.S. equations either in 1D or 3D; lastly, empirical models can be based on either measurements alone or a mixture between important simplifications of the Navier-Stokes equations and empirical parameters (Crespo et al., 1999). All of them must, inevitably, be contrasted to measurements of wind turbine wakes in order to estimate their accuracy and, if applicable, be validated under certain conditions.

The interaction between the atmospheric boundary layer (ABL) and a full scale wind turbine is a three-dimensional, dynamic flow phenomenon that extends from approximately two diameters in front of the rotor to several hundred meters, possibly a few kilometers, downwind (Vermeer et al., 2003). The ideal measurement set for a characterization of a single wind turbine wake would include the three components of the wind velocity vector, at all times and at all positions in space within the region of influence. Unfortunately, no measurement technique is able to provide such data. Different instruments provide different sets of measurements, with varying levels of suitability for the characterization of a wind turbine wake.

The standard instrument for turbulence measurements in the atmosphere, the sonic anemometer, is not well suited for the measurement of turbine wake flows. Sonic anemometers only offer point-wise information and it is not practical to cover an extensive volume by mounting them on meteorological masts. Alternatives to the sonic anemometer and the meteorological mast are, in some cases, unmanned aerial vehicle platforms, since they are able to fly and measure in any point in space (Kocer et al., 2011; Reuder and Jonassen, 2012; Wildmann et al., 2014a; Subramanian et al., 2015a,b). Nevertheless, they have important limitations: most of

them are still mostly in prototype phase, they are not suitable for long-term statistics, and covering a volume with point-wise measurements would imply thousands of hours of flight.

As an alternative, remote sensing techniques are increasingly popular in atmospheric flows because of their ability to measure where other sensors cannot. Among these, Doppler light detection and ranging (lidar) is the preferred remote sensing technique for atmospheric turbulence measurements due to its accuracy and relatively high spatial resolution and long range. As of today, it is the most suitable measurement technique to study the different characteristics of wind turbine wakes (Käsler et al., 2010; Iungo et al., 2013b; Smalikho et al., 2013; Iungo and Porté-Agel, 2014; Banta et al., 2015; Aitken et al., 2014; Doubrawa et al., 2016; El-Asha et al., 2017; Bodini et al., 2017).

One limitation of the lidar technique arises from the fact that it is based on the Doppler effect and uses backscattered light from aerosol. Therefore, it can only measure the velocity component parallel to the laser beam (radial velocity). A scanning Doppler lidar can orient its laser beam in any direction; this implies that, unless the laser beam is completely vertical or aligned with the direction of the flow or transversal to it, the measured velocity is normally a mixture of the three components of the wind velocity vector. As a consequence, most lidar measurements rely on some assumptions when calculating the relevant variables such as horizontal wind speed, vertical wind speed or the different turbulence quantities (Sathe et al., 2011; Sathe and Mann, 2012; Newman and Clifton, 2017). Multiple-lidar techniques exist and can overcome this limitation (Carbajo Fuertes et al., 2014; Newman et al., 2016; Vasiljević et al., 2016) although they multiply the cost, are more cumbersome to use, and require a significantly higher degree of expertise to be properly operated. The use of a single lidar and the necessary assumptions is a source of uncertainty that needs to be estimated.

Another limitation of the lidar technique is the speed of the measurements. A scanning pulsed lidar emits several thousand laser pulses in a particular direction or line-of-sight (LoS), evaluates the backscattered signal, calculates the Doppler shift at different distances from the lidar and then proceeds to the next laser beam orientation. Since a wind turbine wake is inherently dynamic, in order to cover a volume with lidar measurements, a scanning strategy is needed in order to balance angular resolution and number of measurements at each orientation. This translates into finding a compromise between a spatial interpolation error and a statistical uncertainty. These two need as well to be estimated.

As discussed above, no technique is able to provide the velocity field in order to estimate the errors and uncertainties associated with a volumetric lidar scan of a wind turbine wake. Therefore a good strategy is to use a *virtual lidar technique* to perform a *virtual experiment*. Specifically, a turbulence-resolving large-eddy simulation (LES) is performed and then the characteristics and scanning pattern of a virtual instrument can be programmed to extract information or virtual measurements from LES simulated velocity field. These virtual measurements can be post-processed with the same algorithms used to treat real measurements in order to reconstruct the desired flow feature (in this case the far wake of the wind turbine)

Chapter 4. Using a virtual lidar approach to assess the accuracy of the volumetric reconstruction of a wind turbine wake.

and then it can be compared to the original velocity field from the LES simulation. A virtual lidar technique allows the estimation of the different sources of uncertainties or errors separately. In this manuscript the sources of error studied are three: the assumptions used to convert the radial velocity to longitudinal velocity, the statistical error and the interpolation error. Finally, testing different scanning patterns allows to find an optimum which minimizes the errors. The error magnitude, in turn, will determine the quality of future real (time and resource-consuming) field experiments.

Most of the literature regarding virtual lidar studies is very recent. [Stawiarski et al. \(2013\)](#) created a virtual lidar measurement simulator based on LES results in which lidar characteristics such as range gate length, pulse length, total range and measurement frequency are adjustable. In their simulator they include the effect of the convolution of the laser pulse as a cylindrical volume centered around the range gate center and they use a weighted averaging function over the LES data points inside that volume. They discuss extensively the different kinds of errors connected with single and double-lidar measurements and provide the methodology to study the sources of errors and the optimization of dual-Doppler scan patterns. [Stawiarski et al. \(2015\)](#) further performed virtual planar dual-lidar experiments to study the reconstruction and detection of planar turbulent structures.

[Lundquist et al. \(2015\)](#) studied the uncertainty of the Doppler beam swinging (DBS) technique, used by many commercial profiling lidars, when calculating horizontal and vertical velocities while violating the assumption of horizontally homogeneous flow that the technique requires. The calculation of the vertical profiles of horizontal velocity is done using virtual measurements obtained from LES simulations of a wind turbine wake. Similarly, [Mirocha et al. \(2015\)](#) have simulated the effect of the inhomogeneity on profiling lidar measurements using a virtual lidar technique approach under different atmospheric stability conditions.

[van Dooren et al. \(2016\)](#) used virtual lidar experiments to explore the possibilities and uncertainty of wind turbine wake reconstruction with ground-based dual-lidar plan position indicator (PPI) scans. For that, they obtained non-synchronous dual-Doppler lidar measurements from LES simulations and they improved the accuracy of the reconstructed wind field by including a correction based on the mass continuity equation.

[Meyer Forsting et al. \(2017\)](#) developed a novel validation methodology for computational fluid dynamics (CFD) models over the wind turbine induction zone using measurements from three synchronous lidars. The validation procedure relied on making the CFD simulation results comparable with the triple lidar data. To that end, they discretized in space the probability density function of the measured free-stream wind speed. Then they reproduced those distributions numerically by weighting the steady-state Reynolds averaged Navier-Stokes simulations. As a last step, the spatial and temporal uncertainty of the triple lidar measurements were quantified and propagated through the data processing.

Lastly, and although the virtual lidar technique is not used, it is worth mentioning the work of [van Dooren et al. \(2017\)](#) in which they studied the uncertainty of synchronous short-range

continuous dual-lidar measurements for the measurement of scaled wind turbine wakes placed inside a wind tunnel. They were able to compare the estimated uncertainty of some of their configurations by comparing the lidar measurements to those taken by a triple hot-wire probe.

In this study, a virtual lidar technique based on LES simulations, similar to what has been used in some of the above-mentioned references, is used to calculate different error sources for a single pulsed lidar performing volumetric scans of a full scale wind turbine wake under different atmospheric conditions and for two different lidar locations: nacelle-mounted and ground-based. The technique allows to optimize the scanning of the wake and evaluates the quality of the measurement strategy and the assumptions used for the treatment of the data.

There are a number of practical advantages of using nacelle-mounted lidars over ground based ones. Arguably the most important one is the fact that a lidar fixed to the structure of the nacelle of a wind turbine always maintains the same angular orientation with respect to the rotor. This means that it does not need any reorientation with a changing wind direction and it never gets blocked by the tower of the turbine. Nevertheless, practical considerations of this kind are out of the scope of this study.

4.2 Methodology

A virtual lidar approach is based on the idea of performing *virtual experiments* on a flow field in which the three components of the wind velocity vector $\mathbf{v}(x, y, z, t)$ are calculated at each point in space and at each point in time. A convenient way of creating such a flow field is through LES simulations. The results of these simulations can be interpreted as a *virtual reality* from which lidar *virtual measurements* can be extracted, knowing the characteristics of a particular lidar (spatial resolution, repetition rate, range, etc.), its scanning pattern and that it measures only the projection of the wind velocity vector onto the laser beam direction or LoS. The lidar *virtual measurements* obtained can then be processed by the same algorithm used to treat real lidar measurements in order to reconstruct a particular flow feature. Some examples are vertical wind profiles in the ABL, 2D horizontal velocity fields of atmospheric surface layer flow, or 3D velocity fields of wind turbine wakes. The reconstructed flow features can be compared to those obtained from the complete three-dimensional, unsteady LES flow fields as a way to estimate the errors introduced by the assumptions used in the algorithm, by the spatial interpolation and by the limited number of samples in time (statistical error). This also allows for the optimization of scanning patterns in order to minimize the uncertainty for a particular type of experiment.

Next, details are provided about the LES simulations used in this study, the characteristics of the virtual lidar and its scanning strategy, the algorithm for the reconstruction of the 3D flow field, and the optimization process.

Chapter 4. Using a virtual lidar approach to assess the accuracy of the volumetric reconstruction of a wind turbine wake.

4.2.1 LES simulations

The *virtual measurements* are extracted from the results of LES simulations of the interaction of a single turbine with atmospheric boundary layer flow on flat terrain. The WiRE-LES code, described in detail in [Porté-Agel et al. \(2011\)](#) and [Wu and Porté-Agel \(2011, 2015\)](#) was used for the simulations.

Turbulence model, boundary conditions and numerical methods

LES solves the spatially filtered Navier-Stokes equations and, therefore, it solves explicitly all the scales of turbulence bigger than the filter scale (same as the grid scale for implicit filters) while the subgrid-scale stresses (SGS) are parameterized using a subgrid-scale model. In the case of the WiRE-LES code, the spatial derivatives are discretized using a pseudospectral representation for the horizontal directions (hence, periodic lateral boundary conditions) and second-order finite differences for the vertical direction, with a wall modeling based on the log law for the bottom boundary. The top boundary condition is a fixed stress-free lid. The code is fully dealiased using the 3/2 rule and the temporal advancement of the simulation uses a second-order accurate Adams-Bashforth scheme. The SGS turbulence model is the Lagrangian scale-dependent dynamic model detailed in [Porté-Agel et al. \(2000\)](#) and [Stoll and Porté-Agel \(2006\)](#).

Domain size and resolution

The domain size is 3200 m in the longitudinal direction (x), 800 m in the transversal direction (y) and 500 m in the vertical direction (z). The domain is divided uniformly into 160x60x64 grid points, respectively, which yields a spatial resolution of 20 m in x , 13.3 m in y and 7.8 m in z .

Since in the horizontal direction there are periodic boundary conditions, a buffer zone upstream of the wind turbine is required in order to create an undisturbed incoming flow. The inflow condition is obtained via a separate precursor simulation.

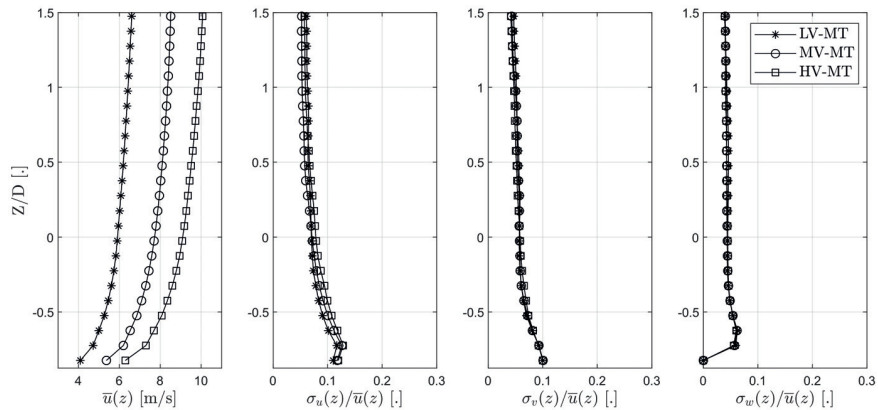
Inflow

The boundary-layer flow in the simulations is driven by a constant streamwise pressure gradient over flat homogeneous surfaces and it is neutrally stratified. Five inflow conditions are used in order to study the influence of different wind speeds and different turbulence intensities. The different turbulence intensities are recreated by using different surface roughness lengths. They are chosen to cover a very wide range between the lowest value corresponding to water or sand (0.0002 m) to grass covered land (0.005 m) and finally the highest roughness corresponding to suburban or forestal land (0.5 m) ([Wieringa, 1992](#)). Different wind speeds at hub height are achieved by modifying the forcing longitudinal pressure gradient dP/dx . The wind speeds selected (6, 7.5 and 9 m/s) cover the range in which the turbine operates at maximum efficiency $C_p \approx 0.42$ and maximum thrust $C_T \approx 0.80$.

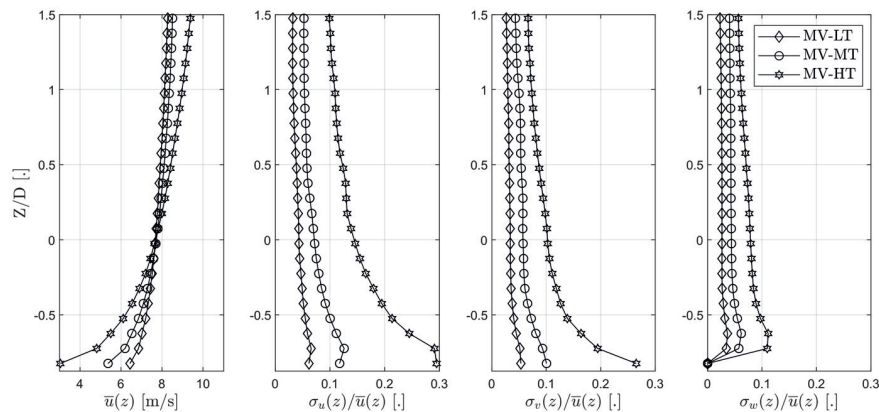
The nomenclature of the different inflow cases is (X)V-(X)T, where V denotes wind velocity, T denotes turbulence intensity and finally (X) can be L-low, M-medium or H-high (e.g. MV-HT

indicates medium wind speed and high turbulence intensity). Figure 4.1 shows the different inflow conditions for the five simulations.

The coordinate system used in this manuscript has its origin at the center of the rotor, and the longitudinal, transversal and vertical directions are represented by X,Y, and Z, respectively. Distances appear normalized by the rotor diameter D, which is 80 m, as described in the section below.



(a) Different wind speeds.



(b) Different turbulence intensities.

Figure 4.1 – Inflow conditions in terms of average horizontal wind speed and longitudinal, transversal and vertical turbulence intensity. The panels on top (a) show three cases with the same turbulence intensity (medium) but different wind speeds, while the panels at the bottom (b) show three cases with the same wind speed (medium) at hub height but different turbulence intensities. The resulting average transversal and vertical velocities from the LES simulations are negligible.

Turbine modeling

The simulation of the aerodynamic forces of the wind turbine and their interaction with the ABL flow is done through an actuator disk model that includes rotation as described in [Porté-](#)

Chapter 4. Using a virtual lidar approach to assess the accuracy of the volumetric reconstruction of a wind turbine wake.

Agel et al. (2011) and Wu and Porté-Agel (2011), where the lift and drag forces of the wind turbine blades are calculated using Blade-Element Momentum theory (BEM) and distributed in a Gaussian manner by convolving the local load and a regularization kernel (Mikkelsen, 2003) and integrated over the spatial and temporal resolution of the simulation.

The wind turbine simulated is a V80-2.0 MW Vestas wind turbine with a hub height of 70 m and a rotor diameter of 80 m. All the details of the modeling of the wind turbine can be found in Wu and Porté-Agel (2015). The results of the simulations are shown in figure 4.2 as vertical planes at $Y=0$ of the temporal average of the longitudinal component of the wind speed \bar{u} and its standard deviation σ_u .

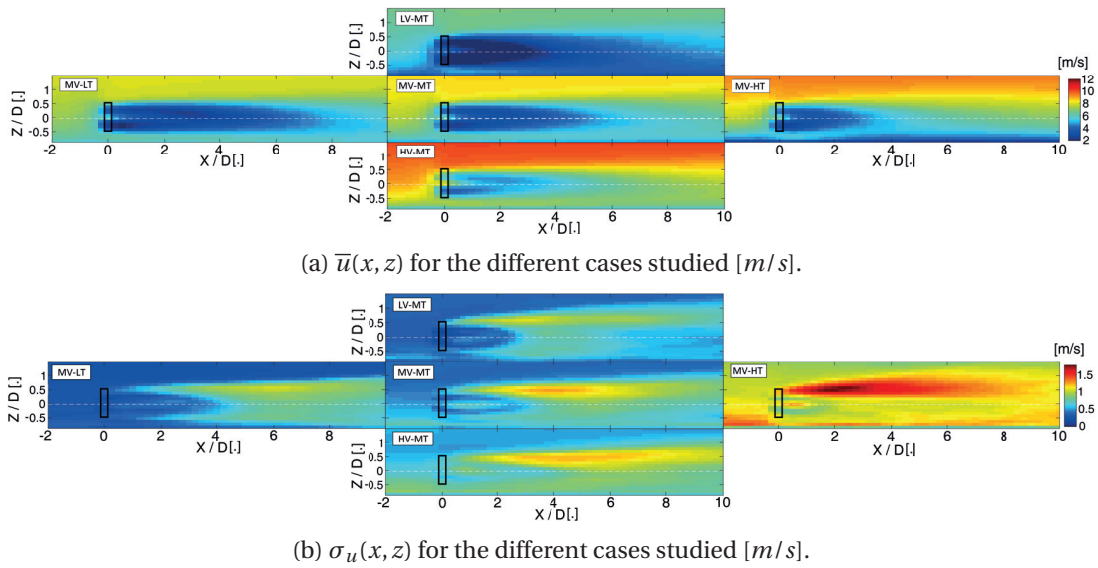


Figure 4.2 – Flow statistics of the simulated wind turbine wakes for the five different inflow cases studied. The figures present vertical symmetry planes of the longitudinal component of the wind velocity in terms of its average (a) and its standard deviation (b). The black boxes correspond to the location of the wind turbine rotor.

The simulations were first run for a period of time long enough to achieve stationary flow conditions, and then a period of 30 minutes was used to sample the simulation results at a resolution of 2 Hz.

4.2.2 Lidar virtual measurements

The lidar simulated in this study is a Halo-Photonics Streamline lidar. It is a pulsed Doppler scanning lidar, which means that it provides measurements of the radial velocity V_r (the projection of the wind velocity into the LoS) at regular distance intervals along the laser beam direction. In this case, the Streamline lidar is able to provide a spatial resolution of 18 m along its LoS, at an acquisition frequency of 2 Hz. The range has been set to infinite since, on our own experience, it exceeds 1.5 km under most atmospheric conditions.

The virtual radial velocity measurements taken by the lidar are then calculated as:

$$Vr(t) = u(x, y, z, t)\cos(\theta(t))\cos(\varphi(t)) + v(x, y, z, t)\cos(\theta(t))\sin(\varphi(t)) + w(x, y, z, t)\sin(\theta(t)), \quad (4.1)$$

where u , v and w are the components of the wind velocity vector field from the LES simulations, and are defined in space (x, y, z) and time (t) ; φ is the azimuth angle (angle between the laser beam and the vertical plane at $Y=0$ of the wake) and θ is the elevation angle (angle between the laser beam and a horizontal plane) that define the orientation of the laser beam in time.

The formally correct calculation of the virtual radial velocity for each laser gate of 18 m would be a convolution of the envelope of the laser pulse on the simulated and projected velocity field (Sathe and Mann, 2013). In this study the convolution is not calculated and the result is instead a point-wise calculation in the linearly interpolated projected field every 18 m. The reason for this is that the resolution of the LES simulation (20 m in the longitudinal direction) is almost the same as the lidar one. This means that the lidar convolution is similar to the spatial filtering already performed by the LES.

The effect of the spatial convolution of high-resolution (20 m) lidar measurements in the attenuation of the longitudinal turbulence intensity has been studied by comparing lidar measurements to sonic anemometry (Carbajo Fuertes et al., 2014). These experiments, under arguably less favorable conditions than the virtual setup presented here, have shown that the attenuation is in the order of a few tenths of a percentage point, since most of the energy-containing scales are resolved at that resolution. These results may not be extended to lower resolution measurements. No significant effect is expected when reconstructing average velocity fields.

It must be noted that in this study the accuracy of the lidar (instrument error) is neglected. The virtual measurement of the radial velocity (equation 4.1) could include a random error that varies for each instrument and that it depends on the signal-to-noise ratio (SNR) of each measurement. This, in turn, depends on the quality of the different optical parts of the instrument, the power of the laser pulse, the aerosol content, the humidity and other parameters related to the processing of the Doppler signal such as the length of the laser gate or the number of pulses averaged. It has been shown that a similar pulsed Doppler lidar to the one discussed in this study can achieve, with favorable SNR, accuracies in the order of ± 0.1 m/s or lower (Pearson et al., 2009). In theory, the effect of simulating this error for any particular instrument will have the effect of slightly increasing the statistical error (in a random manner, therefore no bias introduced) and slightly increasing the standard deviation measurements (therefore, inducing a small bias). Nevertheless, the instrument error of an accurate lidar should be significantly smaller than the turbulent velocity fluctuations found in the wake of a wind turbine and can, in most of the cases, be neglected.

Finally, if a continuous scanning strategy is chosen, the radial velocity calculation has to

Chapter 4. Using a virtual lidar approach to assess the accuracy of the volumetric reconstruction of a wind turbine wake.

include the convolution along the arc that the lidar gate covers between two consecutive measurements. This effect can be particularly important when calculating the standard deviation of the radial velocity for locations far downstream and for low angular resolutions of the measurements. On the other hand, a step-and-stare scan avoids this convolution and arguably provides a better estimation of the turbulent fluctuations. This is why only step-and-stare scans are considered in this study.

4.2.3 Scanning strategy and reconstruction of 3D fields

Depending on the position of the lidar, the ranges of the azimuth and elevation angles are calculated in order to cover the whole volume of interest and are shown in table 4.1. A pulsed scanning lidar can only measure along a particular direction each time, which implies that there will have to be a compromise between the number of measurements at each point and the angular resolution. Once a particular angular resolution is set, the virtual lidar scans the volume of interest in consecutive step-and-stare swipes at constant elevation angles (equivalent to PPI scans) at a frequency of 2 Hz between measurements until the end of the 30 minutes period of each simulation.

Table 4.1 – Ranges of the azimuth and elevation angles needed to cover the whole volume of interest for both lidar locations

	Nacelle-mounted	Ground-based
Azimuth angle range	−16.7° to +16.7°	−16.7° to +16.7°
Elevation angle range	−16.7° to +16.7°	+1.3° to +34.0°

The reconstruction of the longitudinal velocity field at the volume of interest is similar to the procedure described in [Iungo et al. \(2013a\)](#) and [Iungo and Porté-Agel \(2014\)](#) and starts by calculating the average of the radial velocity measurements $\overline{Vr}(\varphi, \theta, r)$ for each laser beam orientation determined by the angles φ and θ and distance r , creating a regular spherical grid with the origin at the lidar location. It continues with the assumption of a negligible effect of the average transversal and vertical components of the velocity into the projection on the laser beam direction: $\overline{v}(x, y, z) \cos(\theta) \sin(\varphi) = 0$; $\overline{w}(x, y, z) \sin(\theta) = 0$. This allows to reconstruct the longitudinal component of the velocity from the radial velocity measurement simply by:

$$\overline{u}(\varphi, \theta, r) = \frac{\overline{Vr}(\varphi, \theta, r)}{\cos(\theta) \cos(\varphi)}. \quad (4.2)$$

The error of this assumption is simply calculated as:

$$\varepsilon = \overline{v}(x, y, z) \cos(\theta) \sin(\varphi) + \overline{w}(x, y, z) \sin(\theta). \quad (4.3)$$

The reconstruction of the standard deviation field of the longitudinal velocity component uses a different assumption (stronger than the previous one) which directly equates the variations

of the instantaneous radial velocity to those of the longitudinal velocity component:

$$\sigma_u(\varphi, \theta, r) = \sigma_{Vr}(\varphi, \theta, r). \quad (4.4)$$

Lastly the values in the regular spherical grid (φ, θ, r) are converted to the original Cartesian grid of the LES simulations (x, y, z) via a linear interpolation. These values constitute the final reconstructed velocity fields from virtual lidar measurements that can be compared directly to the original LES fields.

4.2.4 Optimization

The approach detailed in this section allows to study three different error sources:

- The error of the assumption of unidirectional flow, which depends on the average spanwise and vertical velocity components $\bar{v}(x, y, z)$, $\bar{w}(x, y, z)$ of the wake flow field and the position of the lidar which determines the angles θ and φ at which, in turn, the laser beam operates.
- The statistical error when calculating the average radial velocity at each point in the spherical grid $\bar{Vr}(\varphi, \theta, r)$, which depends on the number of independent lidar measurements for each orientation of the laser beam.
- The interpolation error when converting $\bar{u}(\varphi, \theta, r)$ in the spherical grid to $\bar{u}(x, y, z)$ in the original Cartesian grid, which depends on the angular resolution between consecutive laser beam orientations.

The error associated with the unidimensional average flow assumption is independent from the other two and the only possibility to minimize it is by locating the lidar in a different position, effectively changing the orientation angles θ and φ of the laser beam, as expressed in equation 4.3. Two lidar locations are tested in this study: ground-based at the tower base and nacelle-mounted.

The statistical error and the interpolation error are linked by the fact that the lidar can only measure at one laser beam orientation at a time. A coarser angular resolution will mean more measurements along each orientation (thus, a higher interpolation error but lower statistical one) and vice versa. An optimum compromise can be found in which the sum of both errors is minimum. Seven different angular resolutions are tested, and they imply a number of measurements along each orientation during a 30 minute period for a 2 Hz sampling rate, as shown in table 4.2. For both lidar locations (ground and nacelle) the range of angles that the lidar has to cover in order to scan the whole region of interest is the same (see section 4.2.3) and therefore the number of repetitions is the same in both cases. For each of these cases, the total error is studied and an optimum compromise is found.

As detailed above, this study does not include other sources of error, such as the effect of

Chapter 4. Using a virtual lidar approach to assess the accuracy of the volumetric reconstruction of a wind turbine wake.

Table 4.2 – Angular resolutions used for the 3D scan optimization and corresponding number of repetitions for each laser beam orientation.

Angular resolution	1°	1.5°	2°	2.5°	3°	4°	5°
Number of repetitions	3	7	12	21	29	44	73

the laser pulse convolution, other errors associated with possible non-stationarity and non-uniformity of the atmospheric flow or the error on the radial velocity measurement (instrument error).

4.3 Results

This section presents the results of all the calculations of the errors for the reconstruction of the longitudinal velocity field in terms of its average value $\bar{u}(x, y, z)$ and standard deviation $\sigma_u(x, y, z)$. All errors calculated in this study are presented as absolute values (no difference between positive and negative values), whether they are expressed dimensionally (in m/s) or as a percentage value. The average of the real values of the errors within the volume of interest is close to zero, excluding significant biases in the reconstruction of the different cases.

4.3.1 Error of the average longitudinal velocity component

The error associated with the reconstruction of the average longitudinal velocity component has, as discussed in section 4.2.4, three sources. The first one, which is the assumption of unidirectional average flow, is independent from the other two and it can be treated separately. The remaining two are the statistical and interpolation errors, which are linked by the lidar measurement frequency, as described previously. Together, the three error sources conform the total error.

Error associated with the assumption of unidirectional average flow

The calculation of the error associated with the assumption of unidirectional average flow has three steps: The first step is fixing the location of the lidar as a point in the virtual flow field and calculating the angles φ and θ that correspond to the laser orientation from the lidar to every point in the flow field. The second one is calculating the radial velocity \overline{Vr} from equation 4.1 using the average values $\bar{u}, \bar{v}, \bar{w}$ instead of the instantaneous ones. The third one is applying the assumption of unidirectional average flow and reconstructing the longitudinal velocity field by using equation 4.2. Since the error is evaluated at exactly the same grid points as the LES simulation, there is no interpolation error, and since the average velocity components are used, there is no statistical error.

One example of error fields for the inflow case MV-MT is shown in figure 4.3 for a nacelle-

mounted lidar and for a ground-based lidar situated at the base of the tower. The origin of the error within the volume of interest can be divided into two: first, the deviation from the assumption of unidirectional average flow (i.e. non-zero spanwise and vertical average velocity components) which is bigger in the near wake due mostly to the tangential induction of the rotor and, second, the angle between the laser beam orientation and the x axis (given by φ and θ), whose magnitude is larger for those points at the most upstream outer edges of the region of interest, and it is smaller for the nacelle-mounted lidar case. Therefore, it is easy to notice that the errors are bigger when measuring with a ground-based lidar and it is particularly well illustrated in the transversal planes at a downstream distance of $3D$, as shown in figures 4.3a and 4.3b. While the \bar{v} and \bar{w} components are the same in both cases, a ground-based lidar requires higher elevation angles (θ). This is responsible for errors reaching up to 1.5%, while for the nacelle-based lidar they never exceed 0.25%.

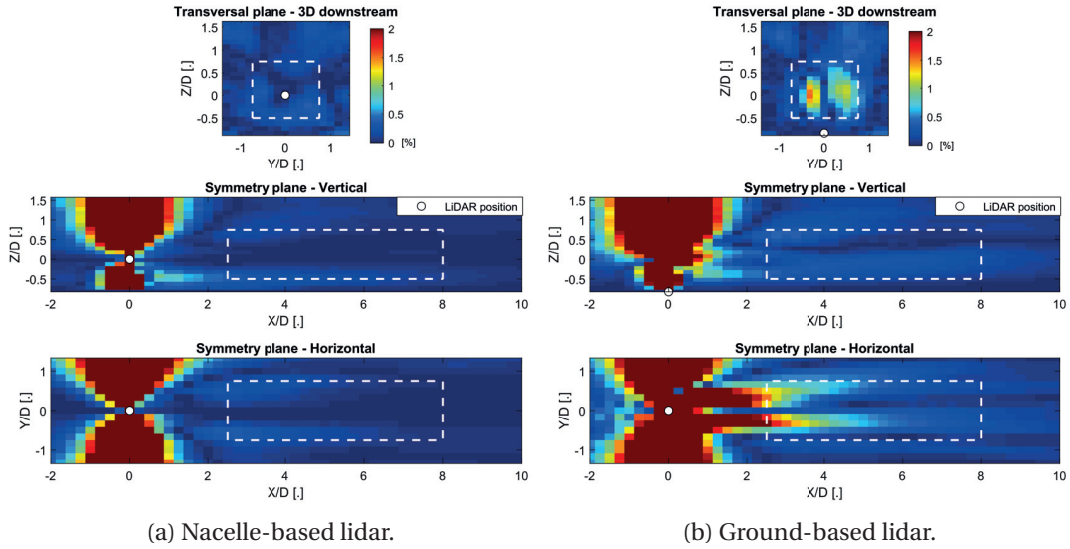


Figure 4.3 – Example of errors in the reconstruction of the longitudinal average velocity component associated only with the assumption of unidimensional flow. The errors correspond to the MV-MT inflow case and for the lidar installed on the nacelle **(a)** and at the base of the tower **(b)**. The volume of interest is delimited by the white dashed line. The figures show the error as a percentage of the undisturbed wind speed at hub height (see section 4.2.1).

One example of error fields for the inflow case MV-MT is shown in figure 4.3 for a nacelle-mounted lidar and for a ground-based lidar situated at the base of the tower. The origin of the error can be divided into two: first, the deviation from the assumption of unidirectional average flow (i.e. non-zero spanwise and vertical average components) which is bigger in the near wake due mostly to the tangential induction of the rotor and, second, the angle between the laser beam orientation and the x axis (given by φ and θ), whose magnitude is large close to the wind turbine, decreases with downstream distance, and it is always smaller for the nacelle-mounted lidar case. Therefore, it is easy to notice that the errors are bigger when measuring with a ground-based LIDAR and it is particularly well illustrated in the transversal

Chapter 4. Using a virtual lidar approach to assess the accuracy of the volumetric reconstruction of a wind turbine wake.

planes 3D downstream of figures 4.3a and 4.3b. While the \bar{v} and \bar{w} components are the same in both cases, a ground-based lidar requires higher elevation angles (θ). This is responsible for errors reaching up to 1.5%, while for the nacelle-based lidar they never exceed 0.25%.

Table 4.3 shows the errors associated with the assumption of unidirectional average flow for the five different inflow cases studied and for both nacelle-mounted and ground-based lidars. The table shows average and maximum errors for the volume of interest already defined in section 4.2.3. It is possible to extract three main conclusions from it:

- The assumption of unidirectional average flow when reconstructing the average longitudinal component of the wind velocity \bar{u} is a good approximation, because of the low average and maximum errors, for the study of the far wake for all inflow cases and both lidar locations.
- The nacelle-mounted lidar yields lower average and maximum errors (between two and five times lower) than the ground-based lidar situated at the bottom of the tower.
- Different inflow conditions do not affect significantly the relative magnitude of the error associated with the assumption of unidirectional average flow.

Table 4.3 – Errors in the reconstruction of the average longitudinal velocity component associated only with the assumption of unidimensional flow. The errors are presented for the different inflow cases studied in terms of average and maximum values found within the volume of interest (see section 4.2.3 and white dashed lines in figure 4.3) for both nacelle-mounted and ground-based lidars. Percentages are based on the undisturbed wind speed at hub height (see section 4.2.1)

	Average error [%]		Maximum error [%]	
	Nacelle	Ground	Nacelle	Ground
MV-MT	0.09	0.29	0.29	1.73
MV-LT	0.10	0.29	0.28	1.87
MV-HT	0.12	0.24	0.59	1.23
LV-MT	0.16	0.25	0.72	1.47
HV-LT	0.06	0.22	0.30	1.44

From the results presented in this section, it can be concluded that the best option to minimize only the error associated with the assumption of unidimensional average flow is to use a nacelle-mounted lidar, although it does not give a very significant advantage since both lidar positions provide acceptably low errors for most analysis purposes.

Total error

The total error includes, on top of the error discussed in the previous section, the effects of the limited number of samples for statistics calculations and the error made when interpolating

back from a spherical grid to a Cartesian one. The calculation of the total error follows these steps:

1. For a given lidar position (nacelle or ground) the range of maximum and minimum values of the azimuth φ and elevation θ angles is calculated. Then, for a given angular resolution, the laser beam performs consecutive PPI scans until the end of the 30 minute periods. This determines the evolution of the elevation and azimuth angles in time $\theta(t)$ and $\varphi(t)$. The number of repetitions or samples for each orientation is shown in table 4.2.
2. For each time step, the virtual lidar measurement is simulated by calculating the radial velocity Vr at each point along the laser beam using equation 4.1.
3. The average of the radial velocity is calculated at each point in space in which the virtual lidar obtains the measurements, creating a spherical regular grid with its origin at the lidar location $\overline{Vr}(\varphi, \theta, r)$.
4. The assumption of unidirectional average flow is used to calculate the average longitudinal component of the wind speed $\overline{u}(\varphi, \theta, r)$ as shown in equation 4.2.
5. The data in the spherical grid are interpolated linearly to the original Cartesian grid to obtain $\overline{u}(x, y, z)$.
6. The difference between the reconstructed $\overline{u}(x, y, z)$ and the same variable obtained from the original LES results conforms the error at each point in space. The average and maximum values of the error inside the volume of interest are computed.

The statistical uncertainty of the average of the radial velocity is inversely proportional to the square root of the number of independent samples \sqrt{N} (Benedict and Gould, 1996). Since the measurement frequency of the lidar has an upper limit, a higher angular resolution means less measurements at each point in space for a given period and vice versa. Thus, a higher angular resolution yields a lower interpolation error, but a higher statistical error. This holds true until the time between measurements at each point in space approaches the integral time scale, which is considered the time between statistically independent measurements. It must be noted, though, that samples along the same laser beam are correlated and those corresponding to the same PPI scans are unlikely to be independent from each other since they are consecutive measurements in time.

The linear interpolation error, in turn, is proportional to the gradient of the spatial derivative of the average flow field and proportional to the distance between the measurement points of the spherical grid. The horizontal gradient of the wind speed is bigger close to the wind turbine, while the distance between measurement points increases with increasing distance to the lidar location and decreasing angular resolution.

Chapter 4. Using a virtual lidar approach to assess the accuracy of the volumetric reconstruction of a wind turbine wake.

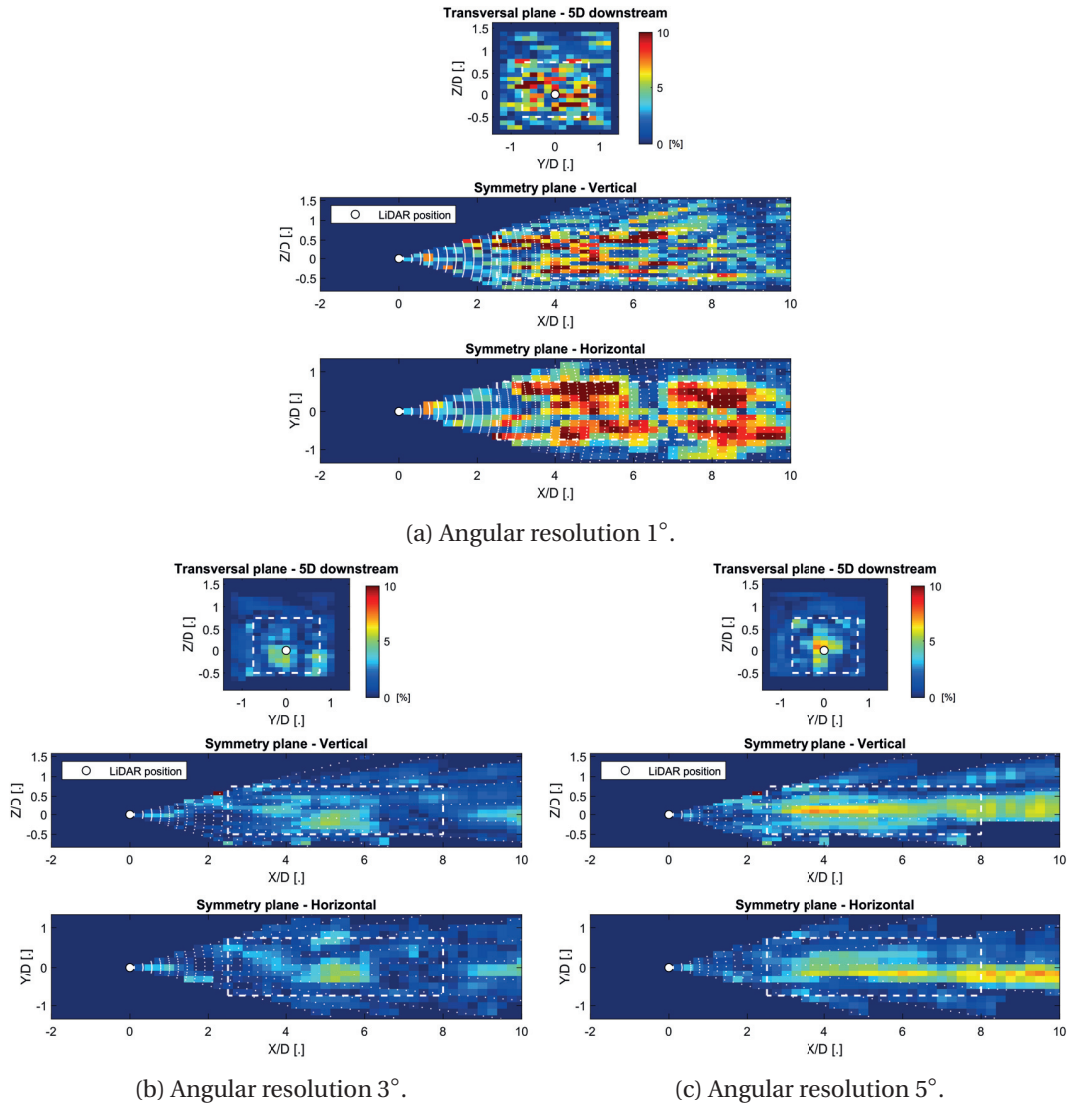


Figure 4.4 – Example of total errors in the reconstruction of $\bar{u}(x, y, z)$ for three different angular resolutions. The errors correspond to the MV-MT inflow case with the nacelle-mounted lidar. The volume of interest is delimited by the white dashed line, and spherical grid points are marked as white dots. The figures show the error as a percentage of the undisturbed wind speed at hub height (see section 4.2.1).

Figure 4.4 shows an example of the total errors for different angular resolutions for the case MV-MT and a nacelle-based lidar. The first noticeable fact is that the angular resolution of 3° (figure 4.4b) shows the lowest errors, and therefore is a good compromise between angular resolution and number of samples or repetitions at each point. On the other hand, a resolution of 1° (figure 4.4a) shows high statistical error, evident by the fact that the errors are randomly distributed (except in the horizontal plane, since it is based on the same PPI scan as explained above) while a resolution of 5° (figure 4.4c) shows high interpolation error, visible in between the white dots that represent the points at which the virtual lidar measures and then interpolates from (this is most noticeable at approximately $Z/D=0.1$ and $Y/D=-0.1$).

Table 4.4 presents an example of an optimization of the angular resolution for the inflow case MV-MT for both lidar locations. As discussed in the previous paragraphs, when scanning the wake with either a high angular resolution (1°) or a low one (5°) the errors are bigger than when using a compromise resolution. The optimum value in the two cases presented is 3° , which balances the statistical errors and the interpolation errors. An extension of this table for all inflow cases studied is presented at the end of this section in table 4.7, where it is possible to identify the optimum angular resolution for each case. For most cases, the optimum value is still 3° , while for a few cases it is 2.5° or 4° , although the error is not significantly sensitive in this range of angular resolutions. It can therefore be concluded that 3° is the overall optimum angular resolution.

Table 4.4 – Example of optimization of the angular resolution for one inflow case and both lidar locations. The table presents the average and maximum total errors for the reconstruction of the average longitudinal velocity component inside the volume of interest. The errors are shown as a percentage of the undisturbed wind speed at hub height (see section 4.2.1).

Angular resolution	1°	1.5°	2°	2.5°	3°	4°	5°
MV-MT nacelle-mounted							
Average error [%]	5.2	2.6	1.6	1.8	1.5	1.7	2.5
Maximum error [%]	18.6	12.2	5.8	6.9	5.4	5.7	8.0
MV-MT ground-based							
Average error [%]	4.7	2.5	1.7	1.7	1.6	1.8	2.5
Maximum error [%]	18.9	15.3	7.7	7.8	6.3	6.9	8.5

Table 4.5 shows the error associated with each inflow case when using an optimum angular resolution of 3° . It can be seen that the errors are reasonably low for most analysis purposes and similar for all inflow cases. Contrarily to what is discussed in section 4.3.1, the nacelle-mounted and ground-based lidars show similar results when considering the total error.

Four main conclusions can be derived from all the information presented in this section:

- An optimum angular resolution can be found which balances the statistical error and the interpolation error.

Chapter 4. Using a virtual lidar approach to assess the accuracy of the volumetric reconstruction of a wind turbine wake.

- The optimum angular resolution is nearly the same for all inflow cases and both lidar locations, and the overall optimum value is 3° .
- Different inflow cases or lidar locations do not affect significantly the optimized total error.
- The total errors found inside the volume of interest are low (average error smaller than 2% and maximum error lower than 8%), which are deemed acceptable for most applications.

Table 4.5 – Total average and maximum errors for the reconstruction of $\bar{u}(x, y, z)$ inside the volume of interest for all inflow cases studied and both lidar locations with the overall optimum angular resolution of 3° . The errors are shown as a percentage of the undisturbed wind speed at hub height (see 4.2.1). The optimum values found in table 4.4 correspond to the first column of this table.

	Nacelle-mounted				
	MV-MT	MV-LT	MV-HT	LV-MT	HV-MT
Average error [%]	1.5	1.9	1.4	1.6	1.7
Maximum error [%]	5.4	7.1	5.7	5.8	5.4
	Ground-based				
	MV-MT	MV-LT	MV-HT	LV-MT	HV-MT
Average error [%]	1.6	2.0	1.8	1.5	1.4
Maximum error [%]	6.3	7.6	6.5	7.0	6.6

4.3.2 Error of the standard deviation of the longitudinal velocity component

The total error of the reconstruction of the standard deviation of the longitudinal velocity component includes the error of the assumption detailed in equation 4.4, the statistical error and the interpolation error. The calculation follows the same steps presented in section 4.3.1, except for point 3, where $\sigma_{Vr}(\varphi, \theta, r)$ is calculated instead of $\bar{u}(\varphi, \theta, r)$, and point 4, in which equation 4.4 is used instead of equation 4.2. The same considerations regarding the statistical uncertainty and the interpolation error explained previously are also valid for the reconstruction of the standard deviation of the longitudinal velocity component.

Figure 4.5 illustrates the impact of the total error on the reconstruction of the standard deviation of the longitudinal velocity component field $\sigma_u(x, y, z)$ for different angular resolutions for the case MV-MT and the nacelle-based lidar. It must be noted that in this figure, for the sake of clarity, the magnitude of $\sigma_u(x, y, z)$ is used instead of the error. It can be seen that a high angular resolution (figure 4.5b) results in a poor performance, while coarser resolutions (figures 4.5c, and 4.5d) yield visibly lower errors.

All the errors associated with each inflow case and both lidar locations are shown at the end of this section in table 4.8. The minimization of the average and maximum errors found inside

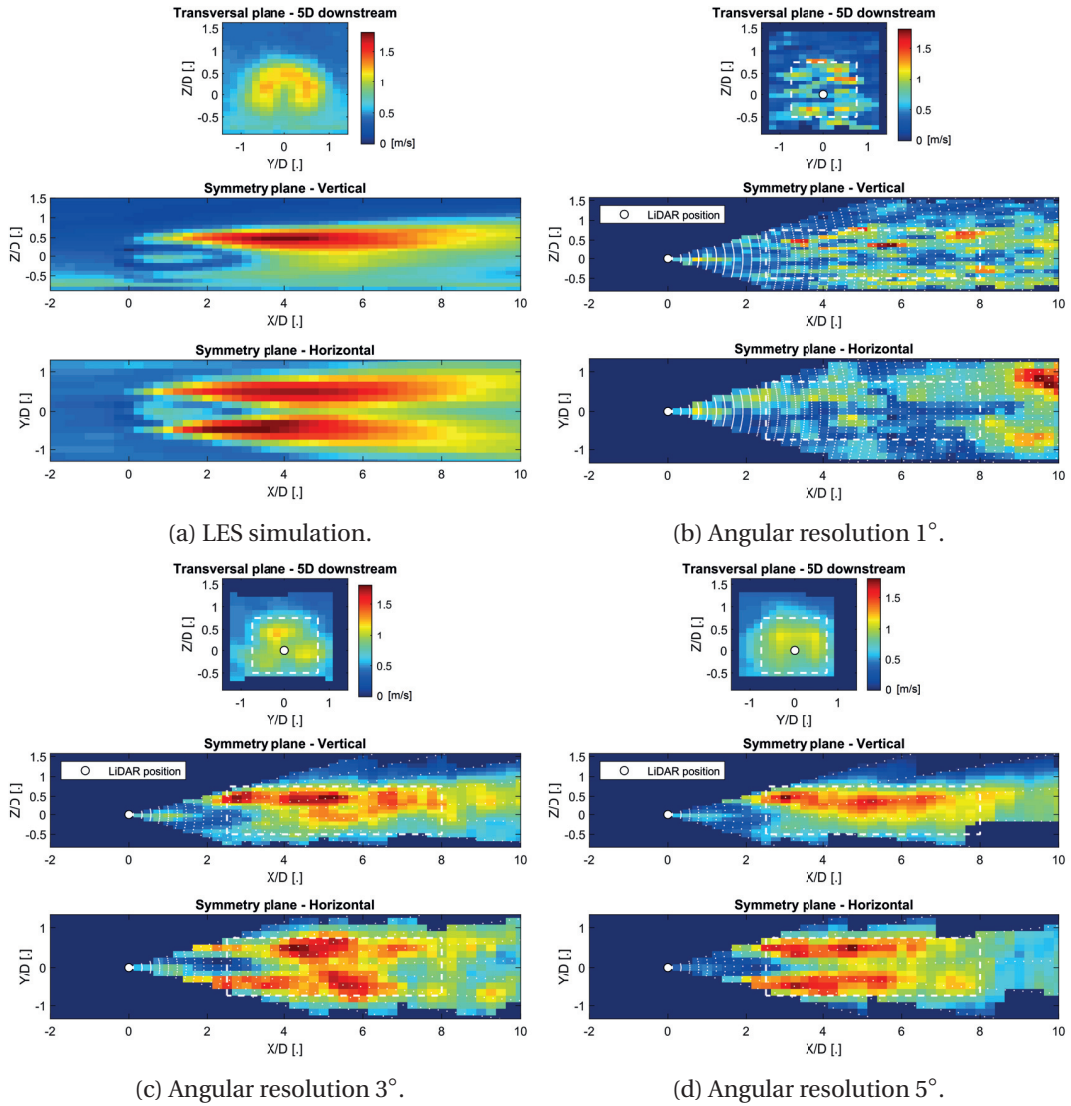


Figure 4.5 – $\sigma_u(x, y, z)$ from LES simulations (a) and example of its reconstruction. The example corresponds to the MV-MT inflow case and to the nacelle-mounted lidar. The volume of interest is delimited by the white dashed line, and spherical grid points are marked as white dots. The figures show the magnitude of $\sigma_u(x, y, z)$ in m/s.

Chapter 4. Using a virtual lidar approach to assess the accuracy of the volumetric reconstruction of a wind turbine wake.

the volume of interest indicates that the optimum values for the angular resolution are always between 2.5° and 4° , therefore 3° is chosen again as an overall optimum angular resolution.

Table 4.6 shows only the errors associated with an angular resolution of 3° . The errors are close in magnitude, although slightly higher, to the errors of $\bar{u}(x, y, z)$ (see table 4.5). This fact might induce some confusion when comparing them. However it should be noted that the values of σ_u are significantly smaller than the values of \bar{u} and, therefore, the accuracy of the calculation of the standard deviations is considerably poorer than that of the mean velocity. It can also be observed that a nacelle-mounted lidar offers a slightly better performance than a ground-based one.

Table 4.6 – Total average and maximum errors for the reconstruction of $\sigma_u(x, y, z)$ inside the volume of interest for all inflow cases studied and both lidar locations with the overall optimum angular resolution of 3° . The errors are shown as a percentage of the undisturbed wind speed at hub height (see section 4.2.1).

	Nacelle-mounted				
	MV-MT	MV-LT	MV-HT	LV-MT	HV-MT
Average error [%]	1.9	1.7	1.9	2.1	1.6
Maximum error [%]	6.0	6.4	6.7	7.2	5.7
	Ground-based				
	MV-MT	MV-LT	MV-HT	LV-MT	HV-MT
Average error [%]	2.4	2.0	2.9	2.5	2.0
Maximum error [%]	7.1	6.5	8.9	8.1	5.8

The findings in this section can be summarized in three main points:

- The overall optimum angular resolution for the reconstruction of σ_u is also 3° .
- The reconstruction of the $\sigma_u(x, y, z)$ field is of worse quality than that of $\bar{u}(x, y, z)$.
- A nacelle-mounted lidar offers a slight advantage over a ground-based one.

Table 4.7 – Total average and maximum errors for the reconstruction of $\bar{u}(x, y, z)$ inside the volume of interest for all inflow cases studied and both lidar locations. The errors are shown as a percentage of the undisturbed wind speed at hub height (see section 4.2.1). The errors corresponding to an optimum angular resolution for each case are identified with an asterisk.

Angular resolution	1°	1.5°	2°	2.5°	3°	4°	5°	1°	1.5°	2°	2.5°	3°	4°	5°
	MV-MT nacelle-mounted							MV-MT ground-based						
Average error [%]	5.2	2.6	1.6	1.8	1.5*	1.7	2.5	4.7	2.5	1.7	1.7	1.6*	1.8	2.5
Maximum error [%]	18.6	12.2	5.8	6.9	5.4*	5.7	8	18.9	15.3	7.7	7.8	6.3*	6.9	8.5
	MV-LT nacelle-mounted							MV-LT ground-based						
Average error [%]	3.9	2.4	2.5	1.7*	1.9	2.5	3.7	3.4	2.4	2.4	1.9*	2	2.5	3.6
Maximum error [%]	17.2	10.7	12.1	5.2*	7.1	8.5	11.7	21.9	10.4	11.2	7.3*	7.6	8.9	11.5
	MV-HT nacelle-mounted							MV-HT ground-based						
Average error [%]	5.8	3.3	2.5	2.1	1.4	1.3*	1.5	6.2	3.6	3	1.8	1.8	1.3*	1.5
Maximum error [%]	21.7	20.7	10.6	7.1	5.7	5*	12.6	26.9	15.6	11.2	6.3	6.5	5.9*	6.6
	LV-MT nacelle-mounted							LV-MT ground-based						
Average error [%]	4.6	3.5	2.8	2	1.6	1.4*	2.2	4.4	3.8	2.7	2.5	1.5*	1.6	2.3
Maximum error [%]	24.8	21.2	11	7.5	5.8*	6.3	9	20.7	18	11.7	11.2	7	6.2*	8.8
	HV-MT nacelle-mounted							HV-MT ground-based						
Average error [%]	4.1	3.3	2	1.8	1.7	1.6*	2.3	4.7	2.6	2.2	1.8	1.4*	1.7	2.2
Maximum error [%]	28.7	17.6	8.3	8.6	5.4*	6.3	9.2	18	13.2	9.6	7.4	6.6	6.1*	8.7

Table 4.8 – Total average and maximum errors for the reconstruction of $\sigma_u(x, y, z)$ inside the volume of interest for all inflow cases studied and both lidar locations. The errors are shown as a percentage of the undisturbed wind speed at hub height (see section 4.2.1). The errors corresponding to an optimum angular resolution for each case are identified with an asterisk.

Angular resolution	1°	1.5°	2°	2.5°	3°	4°	5°	1°	1.5°	2°	2.5°	3°	4°	5°
	MV-MT nacelle-mounted							MV-MT ground-based						
Average error [%]	5.5	2.9	2.2	2.0	1.9*	2.0	2.1	5.2	3.2	2.5	2.4	2.4	2.2*	2.5
Maximum error [%]	15.0	11.9	8.5	6.6	6.0	5.0*	5.3	14.6	11.3	9.8	8.8	7.1	6.4*	6.5
	MV-LT nacelle-mounted							MV-LT ground-based						
Average error [%]	4.2	3.1	2.5	1.7*	1.7*	1.9	2.1	4.4	2.7	2.8	2.0*	2.0*	2.0*	2.3
Maximum error [%]	12.7	9.2	8.8	6.4*	6.4*	6.7	7.7	13.5	9.3	8.3	7.2	6.5	6.4*	7.2
	MV-HT nacelle-mounted							MV-HT ground-based						
Average error [%]	6.3	3.6	2.9	2.0	1.9	1.7*	2.0	6.9	3.9	3.6	2.8	2.9	2.6*	2.7
Maximum error [%]	19.8	12.8	11.5	8.1	6.7	6.1	5.4*	19.6	13.3	13.4	9.4	8.9	7.2*	8.2
	LV-MT nacelle-mounted							LV-MT ground-based						
Average error [%]	5.3	3.5	2.8	2.3	2.0*	2.1	2.3	5.9	3.8	2.8	2.7	2.5	2.4*	2.7
Maximum error [%]	16.0	12.2	9.2	7.2	8.0	7.2	6.8*	16.8	13.4	11.0	10.0	8.1	7.2*	8.0
	HV-MT nacelle-mounted							HV-MT ground-based						
Average error [%]	4.6	2.7	1.8	1.6*	1.6*	1.6*	1.7	4.7	2.7	2.3	2.0	2.0	1.9*	2.1
Maximum error [%]	14.2	10.8	6.7	5.6	5.7	5.7	5.1*	13.9	9.7	8.1	5.9	5.8*	5.9	6.0

4.4 Summary

This study exploits the potential of the virtual lidar technique to explore the uncertainty associated with a volumetric scan of the wake of a wind turbine. When performing a succession of PPI scans, an optimum angular resolution can be found which minimizes the errors when calculating the longitudinal velocity field in terms of its average and its standard deviation. This kind of analysis is important during the experiment design part, prior to a lidar measurement campaign, in order to optimize the scanning pattern. First, the optimization dictates the best way to perform the scan, and the quantification of the error estimates the expected quality of the measurements, which will determine if they are acceptable (accurate enough) or not for a particular purpose.

Our analysis has found that, when performing a volumetric scan of the far wake of an 80 m diameter wind turbine, an angular resolution close to 3° provides the best overall results. This holds true for a lidar with a measurement frequency of 2 Hz and a spatial resolution of 18 m. The accuracy of experiments with lidars with different characteristics can be studied using the same methodology. The study has also shown that different turbulence intensity conditions and different wind speeds do not seem to affect the quality of the measurements significantly. The location of the lidar does not seem to play a significant role on the magnitude of the errors, although a nacelle-mounted lidar has a slight advantage over a ground-based one. Other practical advantages associated with a nacelle-mounted lidar, such as a constant angular orientation with the turbine rotor, are not discussed in this study.

Finally, the errors found when reconstructing the average longitudinal velocity component are low, regardless of the configuration or inflow case studied. This fact suggests that full scale measurements using the setup and data processing detailed previously should be of high quality and potentially acceptable for most applications. On the other hand, the error associated with the reconstruction of the standard deviation of the longitudinal velocity component is almost identical in magnitude to that of the average velocity, which means that, in relative terms, it is higher. This should be considered when assessing the acceptability or not of the lidar measurement of this variable, depending on its final purpose.

Future studies could address the effect of thermal stability of the ABL, wind veer, non-stationary conditions or horizontal inhomogeneity of the undisturbed boundary layer within the wind turbine wake region.

5 Wind turbine wake characterization with nacelle-mounted wind lidars for analytical wake model validation.¹

Abstract

This study presents the setup, methodology and results from a measurement campaign dedicated to the characterization of full-scale wind turbine wakes under different inflow conditions. The measurements have been obtained from two pulsed scanning Doppler lidars mounted on the nacelle of a 2.5 MW wind turbine. The first lidar is upstream oriented and dedicated to the characterization of the inflow with a variety of scanning patterns, while the second one is downstream oriented and performs horizontal planar scans of the wake. The calculated velocity deficit profiles exhibit self-similarity in the far wake region and they can be fitted accurately to Gaussian functions. This allows for the study of the growth rate of the wake width and the recovery of the wind speed, as well as the extent of the near-wake region. The results show that a higher incoming turbulence intensity enhances the entrainment and flow mixing in the wake region, resulting in a shorter near-wake length, a faster growth rate of the wake width and a faster recovery of the velocity deficit. The relationships obtained are compared to analytical models for wind turbine wakes and allow to correct the parameters prescribed until now, which were obtained from wind-tunnel measurements and large-eddy simulations (LES), with new, more accurate values directly derived from full-scale experiments.

¹The contents of this chapter are published in: F. Carbajo Fuertes, C. D. Markfort and F. Porté-Agel. Wind Turbine Wake Characterization with Nacelle-Mounted Wind Lidars for Analytical Wake Model Validation. *Remote Sensing*, 2018, 10, 668.

5.1 Introduction

The wind flow around the rotating blades of a wind turbine creates aerodynamic forces that result in a torque on the rotor axis, which ultimately generates electrical energy, and an axial thrust force, which pushes back the rotor. Following Newton's third law, these actions are compensated with reactions on the wind flow, altering its characteristics within a volume downstream of the wind turbine that is called the wake region (Vermeer et al., 2003). The reaction force of the thrust creates an axial induction opposite to the air motion direction which reduces the kinetic energy of the flow, causing a reduction in velocity. The reaction torque, instead, creates a tangential induction which causes the flow to spin in the opposite sense of the rotation of the blades. Since the reaction aerodynamic forces have a dynamic nature and they generate important shear locally in the flow, they result as well in increased levels of turbulence. A wind turbine wake has two main negative effects on surrounding wind turbines within its area of influence. First, the kinetic energy deficit results in a decrease in energy production (Barthelmie et al., 2010; Hansen et al., 2012), and second, the higher turbulence levels result in higher fatigue loads and a potential life time reduction (Thomsen and Sørensen, 1999).

The correct understanding, characterization, and accurate modeling of wind turbine wakes is of utmost importance for accurate power prediction of wind farms (Markfort et al., 2012; St. Martin et al., 2016) as well as layout optimization (Herbert-Acero et al., 2014; Gebraad et al., 2017). Wind turbine wake models may also play a key role in the control of wind farms (Torben Knudsen and Automation, 2014; Chehouri et al., 2015).

Wind turbine wake models can be analytical (Bastankhah and Porté-Agel, 2014), numerical (Sørensen and Shen, 2002), empirical, or a mixture of them (Crespo et al., 1999). In all cases the wake models need to be validated with experimental data. Wind tunnel experiments present some advantages for validation purposes (e.g., repeatability, flow control, wind turbine control, wind farm layout, etc.) (Chamorro and Porté-Agel, 2009, 2011; Zhang et al., 2013; Lignarolo et al., 2014b; Iungo, 2016; Bastankhah and Porté-Agel, 2016; Bastankhah et al., 2017) but it is very challenging to ensure complete flow similarity for scaled tests (Miller et al., 2016). Ideally, the validation would include a comparison of model prediction under different conditions of the atmospheric boundary layer (ABL) with measurements of full scale wind turbine wakes. The measurement technique best suited to measurements of the wake is the wind lidar (Light Detection and Ranging), which is a remote sensing measurement technique based on the Doppler effect of reflected laser light from aerosol. A pulsed wind lidar, in particular, is able to measure wind speed with relatively high spatial and temporal resolutions (around 20 m and 10 Hz can be easily achieved with state-of-the-art systems under normal atmospheric conditions) up to distances of a few kilometers.

Comparing full-scale measurements of wind turbine wakes and model predictions is particularly challenging and presents a number of difficulties, especially given the limited amount of data available during the experiments. The discussion presented by Barthelmie et al. (2009) is

particularly interesting and relevant for this manuscript. They address the issues related to correctly establishing the free stream flow characteristics (i.e., horizontal wind speed, wind direction, nacelle orientation and yaw misalignment, turbulence intensity and atmospheric stability), to the accuracy of the site specific power curve and thrust coefficients, and to ensuring equivalent time averaging in models and measurements. These difficulties often arise from two important sources, which are the horizontal inhomogeneity and the non-stationarity of the atmospheric flow (i.e., the horizontal gradients and the natural fluctuations in the wind speed and direction in any period).

Recently, an increasing number of studies have investigated wind turbine wakes either via planar or volumetric scans with ground-based scanning lidars (Käsler et al., 2010; Iungo et al., 2013b; Smalikho et al., 2013; Iungo and Porté-Agel, 2014; Banta et al., 2015; Aitken et al., 2014; Doubrawa et al., 2016; El-Asha et al., 2017; Bodini et al., 2017) using different scanning strategies and post-processing algorithms. Nevertheless, nacelle-based lidar experiments (Trujillo et al., 2011; Aitken and Lundquist, 2014; Machefaux et al., 2015, 2016; Herges et al., 2017) have inherent advantages when measuring wakes. Some of these advantages are: the lidar always has the same alignment with the rotor, this alignment is independent from the wind direction, the errors due to the assumption of unidirectional average flow are smaller, and it can perform horizontal planar scans of the wake.

The objective of this study is to present an experimental setup and data post processing methodology for the characterization of single wind turbine wakes under different atmospheric conditions based on two nacelle-mounted lidars. The first lidar is upstream-looking and it is dedicated to the characterization of the inflow conditions in terms of average wind speed, turbulence intensity, yaw and vertical wind shear. The second lidar is downstream-looking and executes horizontal plan position indicator (PPI) scans of the wake. This allows accurate measurements of the velocity deficit in the wake and is ideal for the comparison with the predictions from wake models.

5.2 Methodology

This section describes the characteristics of the site where the tests were performed, as well as the meteorological tower, the wind turbine, the lidar setup, and the methodology used to analyze the data.

5.2.1 Test site

The selected test site is located at the Kirkwood Community College campus, in the state of Iowa. The wind turbine studied is a 2.5 MW Liberty C96 model, manufactured by Clipper Windpower. It is equipped with a Supervisory Control And Data Acquisition (SCADA) system which continuously collects data at 10 min intervals about the wind turbine operation. The main characteristics of the wind turbine are detailed in Table 5.1.

Chapter 5. Wind turbine wake characterization with nacelle-mounted wind lidars for analytical wake model validation.

Table 5.1 – Wind turbine main characteristics.

Clipper Windpower - Liberty C96	
Rated power	2.5 MW (at 15 m/s)
Rotor diameter	96 m
Tower height	80 m
Minimum rotor speed	9.5 rpm
Maximum rotor speed	15.5 rpm
Cut-in wind speed	4 m/s
Cut-off wind speed	25 m/s

Figure 5.1 shows the power coefficient of the wind turbine and the blade pitch angle imposed by the control system as function of the incoming wind speed as registered by the SCADA system. This information helps determining the range of usable wind speeds for the analysis of the wake. The power coefficient C_P is quasi-constant and close to a value of 0.37 for velocities between 5 and 10 m/s. This is the range of velocities where the wind turbine operates optimally and therefore the aerodynamic forces are most important. Once the wind velocity reaches 10 m/s the control system changes the pitch angle of the blades, reducing the aerodynamic efficiency of the rotor and effectively decreasing the thrust forces. We consider that the thrust coefficient C_T is close to constant within the same range of wind speeds, which is common in most wind turbines, and limit the study of the wake to this range. In the absence of manufacturer’s data, and given the similarity in terms of thrust coefficient from commercial wind turbines, a value of $C_T = 0.82$ is estimated for the 5–10 m/s wind speed range.

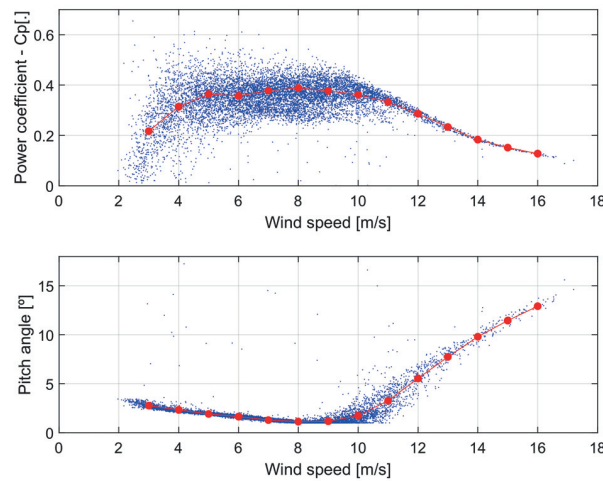


Figure 5.1 – Power coefficient and blade pitch angle as function of the wind speed for the 2.5 MW Liberty C96 wind turbine obtained from SCADA data. 10-minute values are shown in blue dots and binned averages in red. A quasi constant power coefficient is observed for wind speeds from 5 to 10 m/s.

Figure 5.2 shows a satellite image of the Kirkwood Community College campus and its sur-

roundings with the location of the wind turbine and the meteorological tower. The predominant wind directions in the area are NW and SSE as shown in Figure 5.3. The wind turbine is situated at an elevation of 246 m and the surrounding terrain can be considered as rolling terrain. In an area of 3 km around the turbine the maximum elevation difference does not exceed 30 m and the terrain slope rarely exceeds 1%. The surface roughness, which plays a role in the ambient turbulence of the ABL, changes from higher roughness lengths associated to the suburban area of the city of Cedar Rapids (W to N directions) to lower values associated to agricultural fields (NE to SW directions). The campus is equipped with a 106 m tall meteorological tower situated at a distance of approximately 900 m from the wind turbine towards the SSW direction. The tower is equipped with sonic anemometers, cup anemometers and wind vanes—among other instruments—situated at heights of 10, 32, 80 and 106 m for the characterization of the ABL.

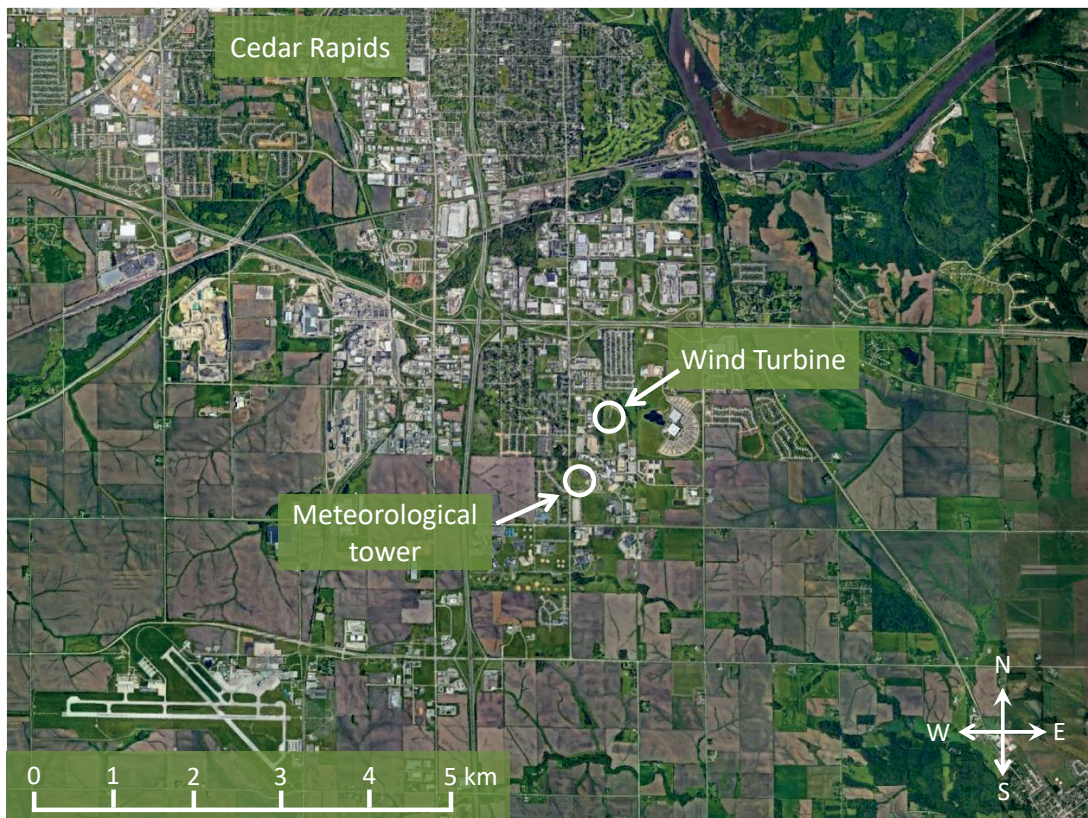


Figure 5.2 – Location of the wind turbine and the meteorological tower inside Kirkwood’s campus as well as the outskirts of Cedar Rapids. Map data: Google, Image NASA.

Figure 5.3 presents the wind rose for the last ten years obtained from measurements at the Eastern Iowa Airport, shown in the lower left corner of Figure 5.2. The airport is situated approximately 5 km to the SW of the test site. The wind presents two main directions: NW are affected by relatively high surface roughness of the suburban area of Cedar Rapids, while SSE are affected by the lower roughness of the agricultural fields.

Chapter 5. Wind turbine wake characterization with nacelle-mounted wind lidars for analytical wake model validation.

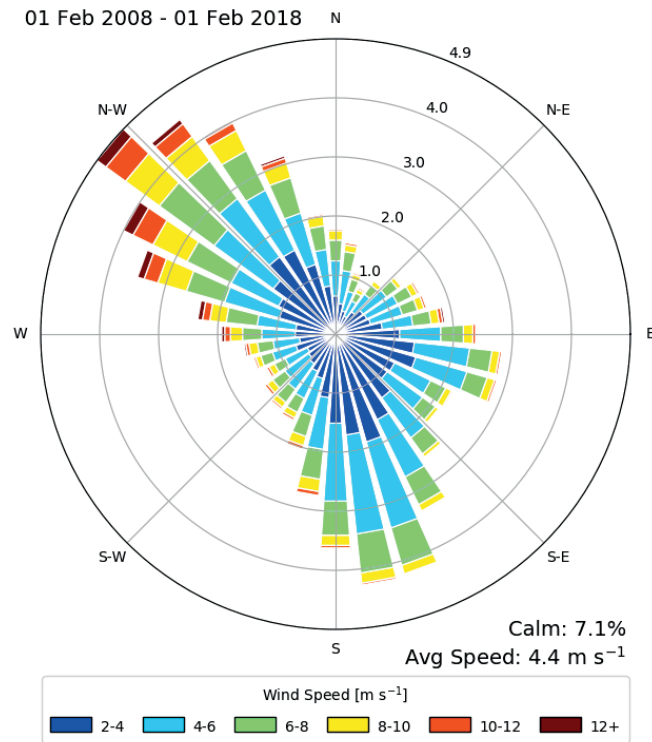


Figure 5.3 – Wind rose measured at the Eastern Iowa Airport for 10 years, situated approximately 5 km to the SW of the wind turbine and visible in Figure 5.2. The wind presents two main directions: NW and SSE. Data obtained from Iowa State University, Iowa Environmental Mesonet. The length of the bars indicate frequency in percentage units.

5.2.2 Lidar setup

The two lidar units used in the experiment are StreamLine models manufactured by Halo-Photonics. These instruments are infrared Doppler pulsed wind lidars which emit 1.5 μm wavelength pulses at a frequency of 10 kHz. They are scanning lidars, which means that the laser beam can be oriented towards any direction thanks to a steerable head. The units are able to provide measurements of the radial velocity with a resolution of 3.82 cm/s at intervals of 18 m along the laser beam direction or Line-of-Sight (LoS) and their measurement range extends from 63 m to more than 1000 m under most atmospheric conditions.

Both lidars are mounted on level platforms installed on the nacelle of the wind turbine. The first unit is an upstream-looking lidar dedicated to the characterization of the incoming flow conditions of the ABL and the second one is a downstream-looking lidar dedicated to the characterization of the wind turbine wake. A sketch of the lidar setup measurement configuration is presented in Figure 5.4. The forward-looking lidar laser beam is commonly blocked by the passage of the wind turbine blades and a quality check algorithm is implemented in order to filter out blocked measurements. Between 5 and 20% of the measurements are rejected under normal operating conditions, although this rarely compromises the analysis of the inflow data.

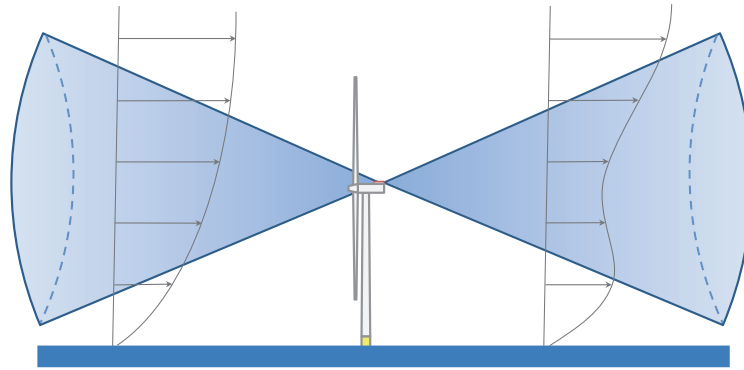


Figure 5.4 – Sketch of the lidar setup with one lidar dedicated to the measurement of the incoming flow conditions and another one dedicated to the characterization of the wake.

5.2.3 Upstream scanning

Both the inflow and the wake scans are grouped into synchronized periods of 30 min. The length of the periods is a compromise between the need for multiple samples in order to decrease the statistical error of the measurements and the requirement of stationarity of the flow. Each period of upstream scanning is divided into four successive scans that quantify different variables of the incoming flow. The calculations assume horizontally homogeneous flow in the region 250–600 m (2.6–6.25D) upstream of the rotor. Only measurements within this range are taken into consideration. Some of the measurements are redundant, such as the wind speed at hub height U_{hub} , yaw angle γ and longitudinal turbulence intensity TI_x , and they help to understand the degree of stationarity of the atmospheric conditions during the 30 min periods. The sub-indexes *ppi*, *rhi* and *st* indicate parameters obtained from Range Height Indicator (RHI), Plan Position Indicator (PPI) and staring-mode scans respectively.

An example of the characterization of the inflow conditions for the period between 22h30 and 23h00 (GMT-6) of 15 September 2017 is provided in the following subsections.

Yaw

The determination of the yaw angle γ_{ppi} and the wind speed at hub height $U_{hub,ppi}$ is done with upstream horizontal PPI scans of a $\pm 60^\circ$ range around the rotor axis direction. The scans are performed at an angular resolution of 4° and a measurement frequency of 3 Hz during 5 min. The yaw angle and the wind speed at hub height are determined by fitting a cosine function to the radial velocities as a function of the azimuth angle φ as detailed in the following equation:

$$Vr(\varphi) = U_{hub,ppi} \cos(\varphi - \gamma_{ppi}). \quad (5.1)$$

Chapter 5. Wind turbine wake characterization with nacelle-mounted wind lidars for analytical wake model validation.

The azimuth angle is defined as the horizontal angle between the laser beam orientation and the downstream axis of the rotor. An example of the wind speed is provided in Figure 5.5 where one can see all the radial velocity measurements taken in the upstream range previously described and plotted against the azimuth angle, the cosine fit and the calculated yaw angle.

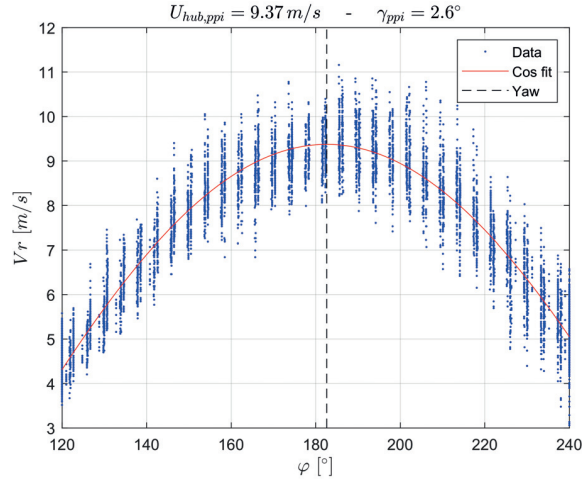


Figure 5.5 – Example of the estimation of the yaw angle and the horizontal wind speed at hub height with plan position indicator (PPI) scans. Data corresponding to the period 22h30–22h35, 15 September 2017.

Vertical profile of the horizontal velocity

The determination of the vertical profile of horizontal velocity is done with upstream vertical Range Height Indicator (RHI) scans aligned with the rotor axis direction of a $\pm 15^\circ$ around the horizontal plane. The scans are performed with an angular resolution of 1° in the elevation angle θ and a frequency of 3 Hz during 5 min. The measurements of radial velocity are corrected with the elevation angle and the yaw angle previously quantified in Section 5.2.3 in order to obtain an estimation of the undisturbed horizontal velocity at different heights:

$$u_\infty(z) = Vr(z) / (\cos(\theta) \cos(\gamma_{ppi})) . \quad (5.2)$$

The measurements of the horizontal component of the wind velocity are divided into blocks of 10 m in the vertical direction, and the average $U_\infty(z)$ and standard deviation $\sigma_{u,rhi}(z)$ are calculated. From these vertical profiles it is possible to extract the values at hub height of the mean horizontal velocity $U_{hub,rhi}$ and the longitudinal turbulence intensity $TI_{x,rhi} = \sigma_{u,rhi}(z_{hub}) / U_{hub,rhi}$. An example is provided in Figure 5.6. Figure 5.6a shows all the corrected horizontal wind speed measurements taken in the upstream range previously described and plotted against height, while Figure 5.6b shows the binned statistics for each block of 10 m in the vertical direction.

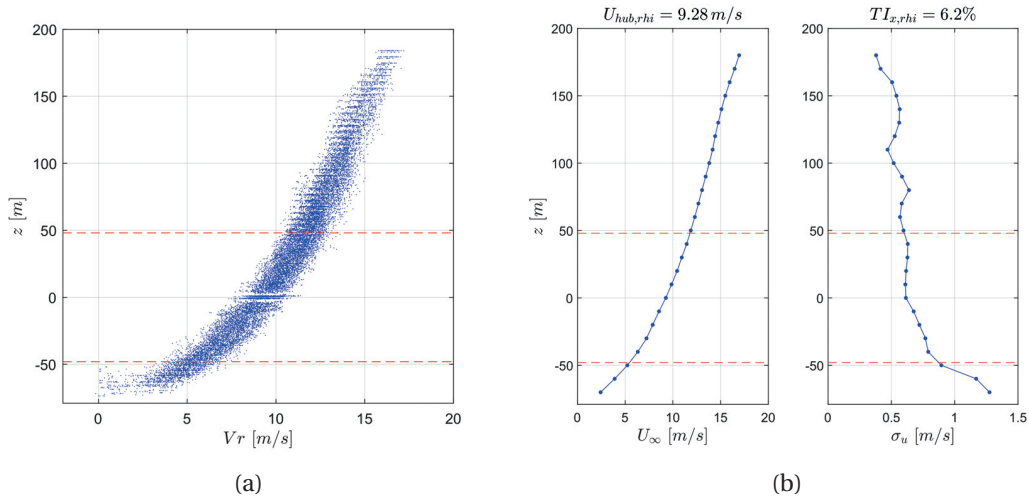


Figure 5.6 – Example of the characterization of the vertical profile of horizontal velocity with range height indicator (RHI) scans. The red dashed lines indicate the upper and lower limits of the rotor. (a) All measurements; (b) Binned statistics. 22h35–22h40, 15 September 2017.

Turbulence intensity

The determination of the longitudinal turbulence intensity $TI_{x,st}$ and a supplementary calculation of the wind speed at hub height $U_{hub,st}$ is done with a staring-mode scan aligned with the rotor axis direction for a duration of 10 min. Measurements are taken at a frequency of 1.5 Hz. Only the measurements of radial velocity in the mentioned upstream range are considered and their average and standard deviation calculated. The wind speed at hub height is corrected with the yaw angle previously calculated in Section 5.2.3:

$$U_{hub,st} = \overline{Vr}_{(\varphi=0^\circ)} / \cos(\gamma_{ppi}). \quad (5.3)$$

The standard deviations of the longitudinal component of the wind speed and the radial velocity are equated:

$$\sigma_u = \sigma_{Vr(\varphi=0^\circ)}, \quad (5.4)$$

and the longitudinal turbulence intensity is calculated as:

$$TI_{x,st} = \sigma_u / U_{hub,st}. \quad (5.5)$$

The transversal turbulence intensity calculation uses a horizontal staring-mode scan of the same duration at an angle of 90° with the rotor axis direction. The same relationship between the standard deviations of the longitudinal component of the wind speed and the radial

Chapter 5. Wind turbine wake characterization with nacelle-mounted wind lidars for analytical wake model validation.

velocity is used:

$$\sigma_v = \sigma_{Vr(\varphi=90^\circ)}, \quad (5.6)$$

Additionally, the transversal turbulence intensity is calculated as:

$$TI_{y,st} = \sigma_v / U_{hub,st}. \quad (5.7)$$

A supplementary estimation of the yaw angle can be obtained by:

$$\gamma_{st} = \tan^{-1} \left(\overline{Vr}_{(\varphi=90^\circ)} / U_{hub,st} \right) \quad (5.8)$$

The calculated values of the wind speed and longitudinal turbulence intensity for the period 22h40–22h50, 15 September 2017, are $U_{hub,st} = 9.12$ m/s and $TI_{x,st} = 5.7\%$. The values of the longitudinal turbulence intensity and yaw angle for the period 22h50–23h00 are $TI_{y,st} = 4.2\%$ and $\gamma_{st} = 2.17^\circ$.

5.2.4 Downstream scanning and reconstruction of planar velocity fields

The wake scanning consists of consecutive downstream horizontal PPI scans with a range of $\pm 20^\circ$ around the rotor axis direction. The scans are performed at an angular resolution of 2° and a frequency of 2 Hz during 30 min.

The reconstruction of the longitudinal velocity fields in terms of its average and standard deviation follows these steps:

1. The average radial velocity $\overline{Vr}(\varphi, r)$ and its standard deviation $\sigma_{Vr}(\varphi, r)$ for all PPI scans are calculated at each point in space separated 2° in the azimuth φ and 18 m in the radial direction r , conforming a regular polar grid .
2. The average radial velocity is corrected with the calculated yaw angle γ_{ppi} in order to estimate the longitudinal velocity component:

$$\overline{u}(\varphi, r) = \overline{Vr}(\varphi, r) / \cos(\gamma_{ppi} - \varphi). \quad (5.9)$$

3. The standard deviation of the streamwise velocity component and the radial velocity are assumed to be the same and are directly equated:

$$\sigma_u(\varphi, r) = \sigma_{Vr}(\varphi, r). \quad (5.10)$$

4. The values in the polar grid are interpolated linearly into a Cartesian grid of 10 m resolution obtaining $\overline{u}(x, y)$ and $\sigma_u(x, y)$, more suitable to the post-processing of the

data and the comparison with wake models.

An example of the average and standard deviation fields is provided in Figure 5.7, where it is possible to see the effect of the interpolation from polar coordinates to Cartesian. The interpolation from a polar grid with a resolution of 2° and 18 m into a Cartesian one with a resolution of 10 m means that the data will be slightly oversampled overall except closer to the rotor, where it will be slightly downsampled in the transversal direction. This should not affect the results obtained from the post-processing of the data. Although the turbulence fields of the wind turbine wake are not used in this study, the authors consider illustrative to show it as proof of the potential of the simple reconstruction technique used from PPI scans.

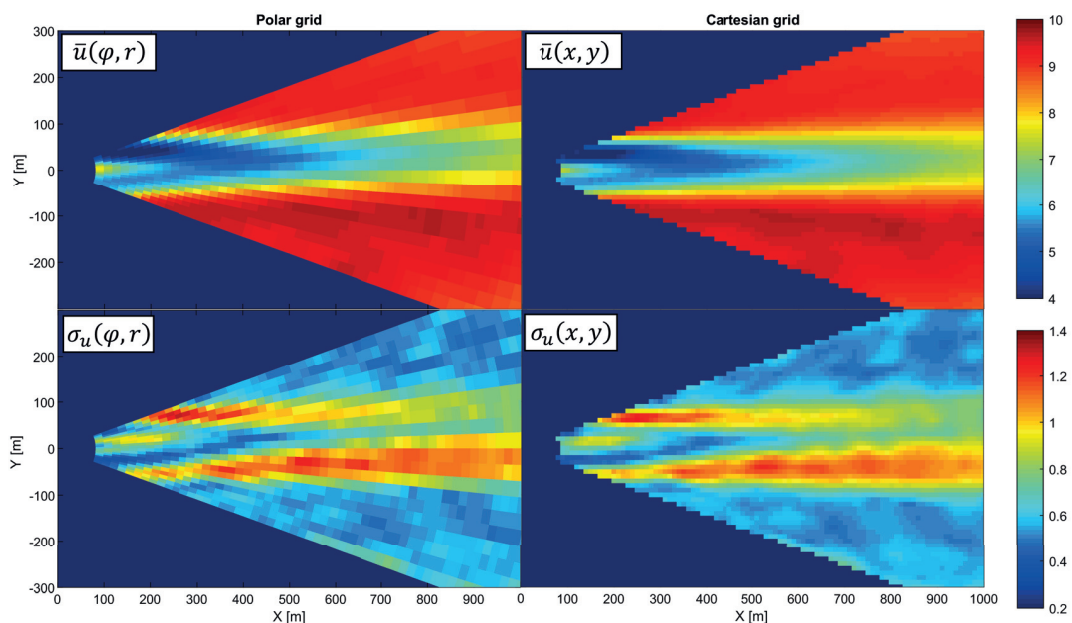


Figure 5.7 – Example of the average and standard deviation of the wake in polar and Cartesian coordinates. 22h30–23h00, 15 September 2017. Units in m/s.

5.2.5 Wake analysis

The analysis of the measurement of the wake of the wind turbine will vary depending on the objective of the study (e.g., wake meandering, yaw and skew angles, near/far wake determination, etc.). In this case the objective is the comparison with the predictions of the analytical model by [Bastankhah and Porté-Agel \(2014\)](#), who assumed Gaussian velocity deficit profiles in the far wake region and used mass and momentum conservation to link the growth rate of the wake and the recovery of the velocity deficit for different inflow conditions.

The local velocity deficit is defined as the difference between the local wind speed and the

Chapter 5. Wind turbine wake characterization with nacelle-mounted wind lidars for analytical wake model validation.

undisturbed wind speed at hub height:

$$\Delta \bar{u}(x, y) = U_{hub} - \bar{u}(x, y). \quad (5.11)$$

The far wake of the wind turbine is defined as the region of the wake that exhibits self-similar velocity deficit transversal profiles, which are well approximated by a Gaussian function of the form:

$$\Delta \bar{u}(x, y) = C(x) e^{-\frac{(y-y_c(x))^2}{2\sigma_y(x)^2}}, \quad (5.12)$$

where C is the amplitude in m/s and corresponds to the velocity deficit along the centerline, y_c corresponds to the deviation of the center of the wake in meters from the longitudinal rotor axis and, finally, σ_y is the standard deviation in meters and corresponds to the wake width. In order to avoid contamination from data outside the area of interest, such as horizontal inhomogeneities of the free stream wind flow, the Gaussian fit to measured data uses a weighted nonlinear least squares regression. The weighting function is the resulting Gaussian function, but 50% wider. The goodness of the fit has been estimated by calculating the correlation ρ between measured and Gaussian fitted velocity profiles. It gives an indication of the beginning of the far wake region, or, conversely, the length of the near wake ℓ_{nw} . A value of $\rho = 0.99$ has been selected in [Sorensen et al. \(2015\)](#) as the threshold to determine this distance.

An example of the analysis of a wind turbine wake is presented in Figure 5.8. In Figure 5.8a it is possible to see the velocity deficit vectors measured and the fitted Gaussian functions. It is noticeable the characteristic bimodal velocity deficit profile in the near wake, where a Gaussian function is not a good representation. In contrast, in the far wake the velocity deficit profile is self similar and shows an almost perfect fit to a Gaussian function. Figure 5.8b shows the longitudinal evolution of the Gaussian parameters of the fit. The first plot from the top shows the correlation coefficient between the measured velocity deficit and the Gaussian fit, together with the threshold $\rho = 0.99$ that indicates the beginning of the far wake ([Sorensen et al., 2015](#)). In the case depicted it occurs at a distance of 3.9D from the rotor. The second plot shows the growth of the wake width in the longitudinal direction. Several wake models assume a linear expansion of the wake and it is possible to observe that it is a good assumption for the far wake region. The figure shows the coefficients of the linear fit in the form:

$$\sigma_y(x) = \left(k^* \frac{x}{D} + \varepsilon \right) D, \quad (5.13)$$

where D is the rotor diameter, k^* is the longitudinal growth rate of the wake width and ε is the wake width at the rotor plane.

The third plot of Figure 5.8b shows the velocity deficit along the centerline C and its decrease in the longitudinal direction, corresponding to the recovery of the wake velocity. Based on conservation of mass and momentum, this parameter has been linked to the wake width in

the far wake by the following relationship (Bastankhah and Porté-Agel, 2014):

$$\frac{C(x)}{U_{hub}} = 1 - \sqrt{1 - \frac{C_T}{8(\sigma_y(x)/D)^2}}. \quad (5.14)$$

The plot also shows in a continuous red line the prediction of the C parameter by the analytical model, which shows good agreement for the far wake using the calculated wake expansion from the previous quadrant. It is also possible to observe that the prediction deviates substantially from the measured values when the Gaussian profile is not a good representation of the velocity deficit profile ($\rho < 0.99$). Finally, the last plot shows the deviation of the center of the Gaussian profile from the axis of rotation. The deviation follows a linear trend for the far wake as well and it is possible to calculate the skew angle of the wake by:

$$\chi = \tan^{-1}(\partial y_c / \partial x), \quad (5.15)$$

which, in the case presented, is 1.3° . This parameter could be useful to study the relationship between the yaw angle and the skew angle.

The analysis procedure described above is applied to all the 30 min periods in which the experiment has been divided and results are presented in Section 5.3.

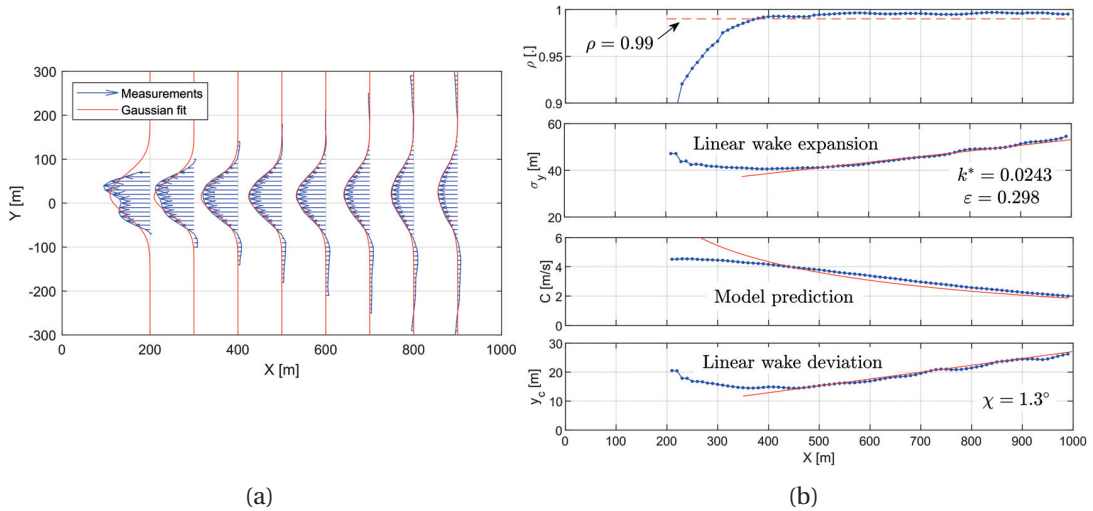


Figure 5.8 – Example of the analysis of the wake of the wind turbine. (a) Velocity deficit and Gaussian fits; (b) Downstream evolution of the fit parameters. 22h30–23h00, 15 September 2017.

5.3 Results

This section describes the first measurements used for the analysis of the wake of the wind turbine as well as the conditions which entail a removal of those periods which are not suitable.

Chapter 5. Wind turbine wake characterization with nacelle-mounted wind lidars for analytical wake model validation.

The aggregated results are then presented and compared to data used to further validate and calibrate the analytical model discussed in Section 5.2.5.

The experiment data consists of a series of 30 min periods obtained between 20 August and 16 October 2017. One 30 min period is obtained every two hours for a total number of approximately 700. The inflow conditions for each period have been thoroughly studied in order to filter out those not suitable for the analysis of the wake. Criteria that were used to filter out measurement periods include (although are not limited to):

- Down times of the wind turbine.
- Wind speed outside the 5–10 m/s range.
- Low signal-to-noise ratio of the lidar measurements due to precipitation.
- Non-stationary undisturbed wind speed at hub height (comparison of $U_{hub,st}$, $U_{hub,ppi}$, $U_{hub,rhi}$).
- Non-stationary undisturbed wind direction at hub height (comparison of γ_{st} , γ_{ppi}).
- Non-stationary undisturbed turbulence intensity at hub height (comparison of $TI_{x,st}$, $TI_{x,rhi}$).
- Horizontal inhomogeneity of the wind speed in the surroundings of the wind turbine (this horizontal inhomogeneity can be easily observed when reconstructing the average of the longitudinal velocity field $\bar{u}(x, y)$ and observing the regions not affected by the wake. It can be seen that the case presented in Figure 5.7 shows a horizontally homogeneous flow outside the area of influence of the wake).
- Changing orientation of the rotor by the control system of the wind turbine.
- Measured yaw angles above $\pm 10^\circ$.
- Disagreements among the inflow measured by the nacelle-mounted lidar, the data from the meteorological tower, and the SCADA data.

From all the collected data, only 44 periods have been selected as suitable for analysis, which yields a validity rate of around 6%. Three of the selected cases are shown for illustrative purposes in Figure 5.9. They are ordered in increasing inflow turbulence intensity at hub height from left to right. The top quadrants present the adimensional velocity deficit in the horizontal plane at hub height and it is observed that the wind speed recovery occurs significantly faster for higher turbulence conditions. It is also observed that lower turbulence conditions retard the occurrence of a self-similar Gaussian velocity deficit profile, indicating there is a significantly longer near wake region. The bottom quadrants present the longitudinal turbulence intensity in the horizontal plane at hub height. It is observed that the background turbulence intensity levels in those areas not affected by the wind turbine wake as well as the

turbulence generated by the shear, which is greatest in the mixing layers at the edge of the wake. The values of the incoming turbulence intensity, wake growth rate, wake width at the origin, and length of the near wake for these three cases are highlighted in Figures 5.10–5.12.

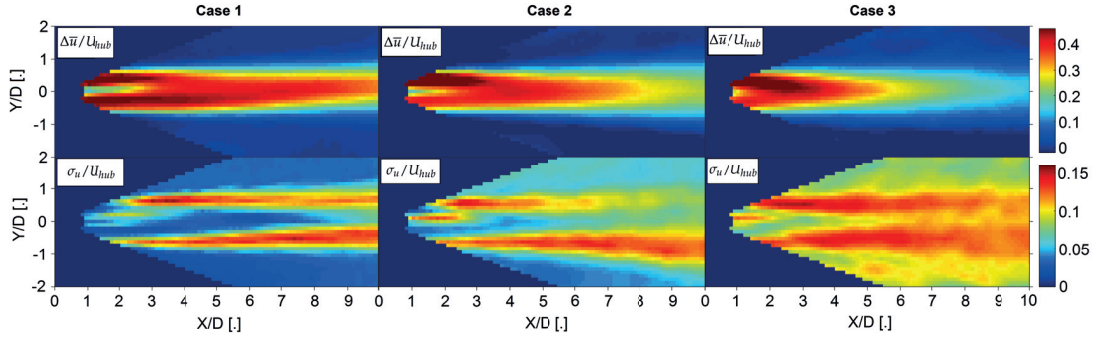


Figure 5.9 – Example of three cases of wakes for increasing different longitudinal turbulence intensity conditions at hub height (Case 1–2.2%; Case 2–4.6%; Case 3–9.9%). The top quadrants present the adimensional velocity deficit while the bottom quadrants present the longitudinal turbulence intensity in the horizontal plane at hub height. These three example cases are further referenced in Figures 5.10–5.12.

The relationship found between the wake width growth rate k^* and the longitudinal turbulence intensity TI_x is presented in Figure 5.10. The data from the full scale field experiment (blue stars) as well as data from validated LES simulations (black squares) and wind tunnel experiment (black circle), presented in Bastankhah and Porté-Agel (2014), agree well, taking into account the significant variability of the data. The data show clearly that the rate of growth of the wake width increases with the turbulence intensity. The growth of the wake is linked to the velocity recovery by mass and momentum conservation as already discussed. This implies a faster recovery of the velocity deficit for higher background turbulence since turbulence enhances flow mixing and the transfer of momentum from the undisturbed flow region into the wake. The linear fit to the full-scale field data is presented as a dashed red line in Figure 5.10, and it can be expressed as:

$$k^* = 0.35 TI_x . \quad (5.16)$$

The linear relationship of Equation (5.16) is similar to the one used in Niayifar and Porté-Agel (2016) by fitting a straight line to the data presented in Bastankhah and Porté-Agel (2014), $k^* = 0.383 TI_x + 0.0037$ (presented as a dashed black line in Figure 5.10). When using these relationships, it is important to take into account the variability of the data, which indicates that it is not uncommon to find wake growths that differ by a factor of two or three for very similar conditions of longitudinal turbulence intensity. This suggests that further experiments should be addressed to understand the role of other variables that could also play an important role on the development of the wind turbine wake.

Chapter 5. Wind turbine wake characterization with nacelle-mounted wind lidars for analytical wake model validation.

One particularly interesting effect to study is the occurrence of different wake growths in the vertical and horizontal directions, which makes the velocity deficit profiles not self-similar in the radial direction, leading to an elliptical profile instead of a circular one. Only considering the horizontal growth rate violates mass and momentum conservation and could be a reason for the variability of the results. Volumetric downstream scans with a similar setup have been performed during the same dates to further study this fact and preliminary analysis proves the occurrence of non circular velocity deficit profiles under certain atmospheric conditions. A more complete analysis can be provided in the future.

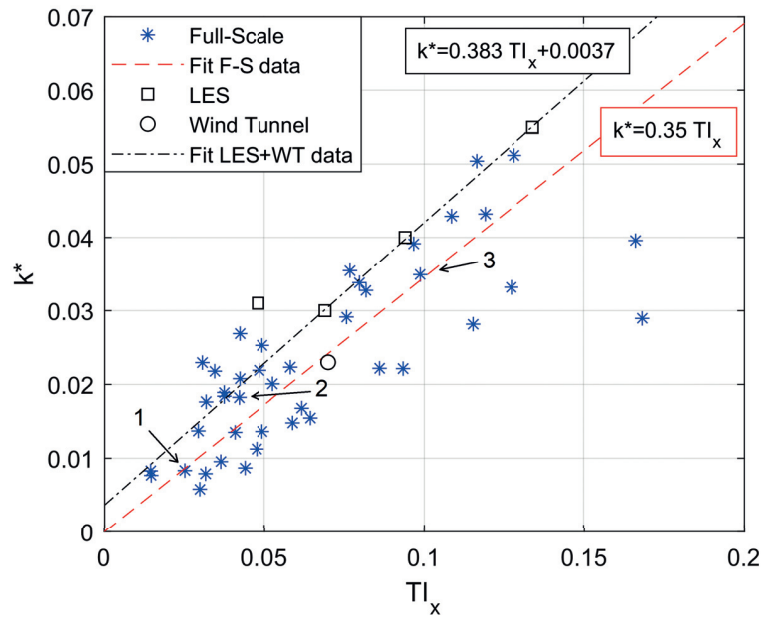


Figure 5.10 – Relationship between wake growth k^* and longitudinal turbulence intensity TI_x . In blue all the data collected during the experiment, in dashed red the linear fit to the full-scale field data presented in Equation (5.16). In black the data obtained from Bastankhah and Porté-Agel (2014) and the linear fit used in Niayifar and Porté-Agel (2016). Numbers 1 to 3 indicate the cases presented in Figure 5.9.

The relationship between the growth rate of the wake and the wake width at the rotor plane ϵ is presented in Figure 5.11. ϵ is not physical, but rather a theoretical parameter, which indicates the hypothetical wake width at the rotor plane when considering a Gaussian wake from its origin (i.e., no existence of a near wake region). The correlation is negative, which means that for a higher growth rate, the width at the rotor plane is smaller. The figure presents the data obtained during this experiment (blue stars) together with its linear fit, which allows for the calculation of the wake width at the origin for a particular wake growth rate is presented as a dashed red line:

$$\epsilon = -1.91k^* + 0.34. \tag{5.17}$$

The agreement between the full-scale field data and the data from the validated LES simulations (black squares) is good, but it is poor for the wind tunnel measurements (black circle).

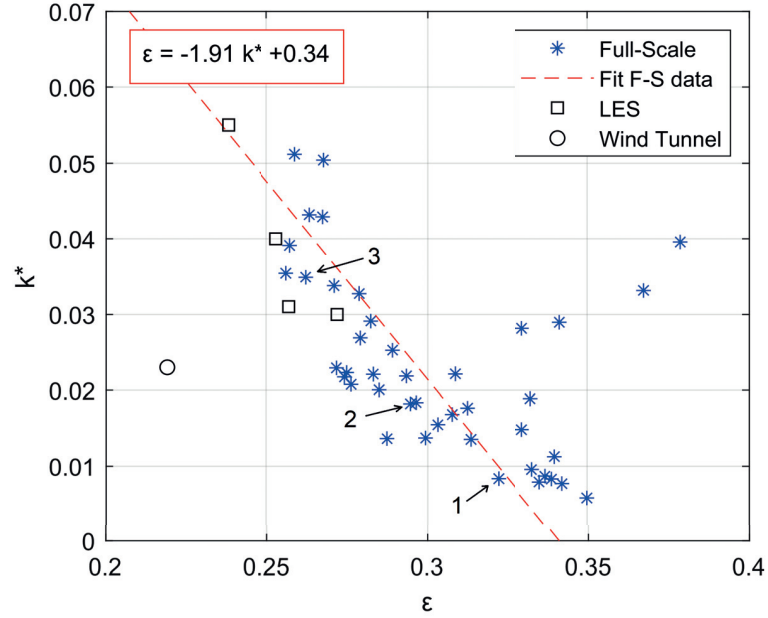


Figure 5.11 – Relationship between wake growth k^* and wake width at the rotor ε . In blue all the data collected during the experiment, in dashed red the linear fit to the full-scale field data presented in Equation (5.17). In black the data obtained from Bastankhah and Porté-Agel (2014). Labels numbered 1 to 3 indicate the cases presented in Figure 5.9.

Finally, the relationship between the length of the near wake ℓ_{nw} and the longitudinal turbulence intensity is presented in Figure 5.12. The setup used, and the range of the downstream PPI scans (see Section 5.2.4) does not allow for scans of the full width of the wake for shorter distances than approximately 200 m and, therefore, shorter near wake lengths are not included in the analysis. This is represented by the gray shaded area at the bottom of the figure. Similarly to the effect of the growth rate, a higher inflow turbulence intensity enhances flow mixing and this helps the wake reaching a self-similar state in a shorter distance. The length of the near wake reaches long distances, higher than six diameters in some cases, for particularly low turbulence flow. It can be observed that in this range of low turbulence intensities, the variability of the data becomes also greater.

A semi-analytical expression for the length of the near wake of a wind turbine under yaw conditions is presented in Bastankhah and Porté-Agel (2016). The corresponding relationship for zero or negligible yaw angles is:

$$\frac{\ell_{nw}}{D} = \frac{1 + \sqrt{1 - C_T}}{\sqrt{2}(\alpha T I_x + \beta(1 - \sqrt{1 - C_T}))}, \quad (5.18)$$

Chapter 5. Wind turbine wake characterization with nacelle-mounted wind lidars for analytical wake model validation.

where β is a parameter obtained from analogy with jet flows and has a value of 0.154 and α is obtained from experimental data. The value of $\alpha = 2.32$ prescribed in Bastankhah and Porté-Agel (2016) was obtained from wind-tunnel experiments. The expression for the length of the near wake using this value is represented in Figure 5.12 as a dashed black line. A value of $\alpha = 3.6$ provides a better fit to the full scale experimental data, as shown by the red dashed line in Figure 5.12. It should be noted that the experimental data used in order to obtain the value of 3.6 is more exhaustive in terms of range of turbulence intensities covered and number of independent data points obtained.

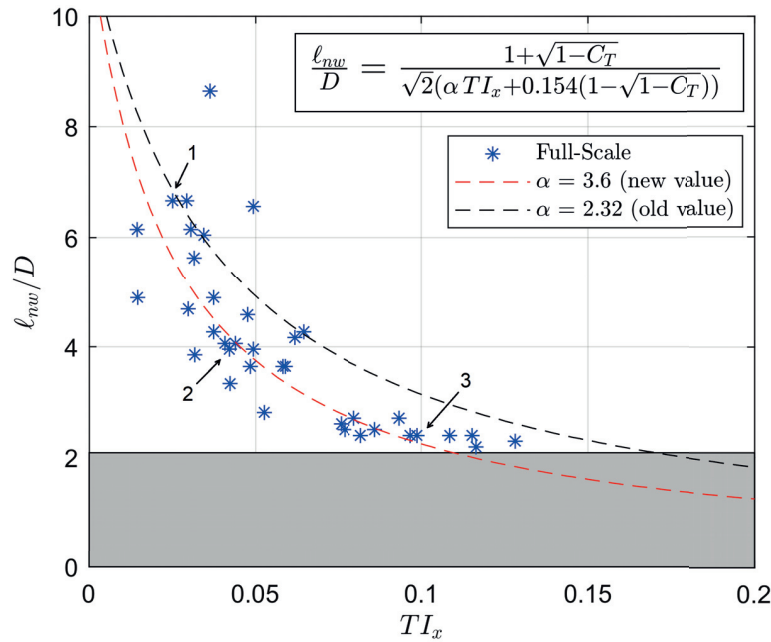


Figure 5.12 – Relationship between near wake length ℓ_{nw} and longitudinal turbulence intensity TI_x . In blue all the data collected during the experiment, in dashed black Equation (5.18) for the estimation of the near wake length with the value of $\alpha = 2.32$ prescribed in Bastankhah and Porté-Agel (2016) and in dashed red the same equation with the value of $\alpha = 3.6$ that provides a better fit to the full-scale field data. The grey rectangle at the bottom indicates the lowest bound for a possible calculation of the near wake length with the presented setup and analysis. Numbers 1 to 3 indicate the cases presented in Figure 5.9.

5.4 Summary

The study demonstrates that a measurement setup based on two nacelle-mounted lidars can be used to measure different characteristics of the incoming flow via RHI, PPI and staring-mode scans, while at the same time perform planar scans of the wake. The upstream oriented lidar data were processed with simple algorithms to calculate the vertical profile of horizontal velocity, the yaw angle of the incoming flow, and the longitudinal and transversal turbulence intensities. The downstream oriented lidar data were aggregated statistically and used to

reconstruct the longitudinal velocity field in terms of its average and standard deviation. The velocity deficit profiles were fitted to Gaussian functions and provide information about the wake width and the velocity deficit along the center line at different longitudinal distances.

With the calculated inflow and wake parameters described above, it is possible to study the relationships between wake growth rate, wake width at the rotor plane, length of the near wake, and longitudinal turbulence intensity. A higher incoming turbulence increases mixing and the transfer of momentum from the regions outside the wake into it, reduces the length of the near wake, and increases the velocity recovery. A higher wake growth rate, in turn, implies a smaller wake width at the rotor plane. Different relationships have been established for these relationships.

The presented data have been compared to the predictions of the analytical wake model based on Gaussian velocity profiles and mass and momentum conservation developed by [Bastankhah and Porté-Agel \(2014, 2016\)](#). It has been found that the model predicts the wake expansion and velocity deficit well, as well as the length of the near wake region. The empirical parameters prescribed in the original model have been updated with the field experiment data.

This study can be extended to use volumetric measurements of the wake and using a similar methodology, in order to understand the implications in the development of the far wake under certain atmospheric conditions when the velocity deficit profile is not self-similar in the radial direction (i.e., not circular).

6 Overall summary and future research perspectives

6.1 Overall summary

This thesis is focused in the development of measurement techniques for atmospheric boundary layer flows with a special emphasis in wind energy. The four studies that compose this work are summarized below.

- **Study 1:** presents a technique for the measurement of atmospheric turbulence and temperature at a point in space based on the integration of a fast-response multi-hole pressure probe and a thermocouple with an inertial measurement unit on a multirotor UAV-based platform. This technique allows for an accurate measurement of time series of the three components of the velocity vector and temperature at any point in space in which the UAV can fly within the limitations of its autonomy. The presented technique relies on an accurate correction of the three-component velocity vector measured by the pressure probe on the frame of reference of the UAV -non inertial- with the information provided by the inertial measurement unit. The study includes a validation of the technique against sonic anemometry and the measurement of the signature of tip vortices shed by the blades of a full-scale wind turbine as an example of its potential.
- **Study 2:** presents a technique to measure the time series of the three components of the wind vector at a point in space from synchronous measurements of three scanning Doppler wind lidars. Knowing the position of each lidar on the ground and the orientation of each laser beam allows for reconstructing the three components of the wind velocity vector. The laser beams must intersect at the desired point in space and their directions must be noncoplanar, so that trigonometric relationships allow the reconstruction of the velocity vector in any coordinate system. The technique is validated against sonic anemometry in terms of the measured instantaneous velocity vector, turbulence statistics, Reynolds stresses, and the spectra of the three components of the velocity and the turbulent kinetic energy.
- **Study 3:** investigates the performance of volumetric measurements of the wake of a

wind turbine by a single lidar. The study simulates the performance of a virtual lidar on synthetic LES data, reconstructs the wake in terms of the average and the standard deviation of the longitudinal velocity component, and quantifies the errors. Different inflow conditions and two lidar locations (nacelle-mounted and ground-based) are explored. This allows to test different scanning patterns and find an optimum which balances the three error sources studied -error inherent to the assumptions, statistical error and interpolation error- with the objective of minimizing the total error.

- **Study 4:** presents the setup, methodology and results from a measurement campaign dedicated to the characterization of full-scale wind turbine wakes under different inflow conditions. The measurements are obtained from two pulsed scanning Doppler lidars mounted on the nacelle of a 2.5 MW wind turbine. The first lidar is upstream oriented and dedicated to the characterization of the inflow with a variety of scanning patterns, while the second one is downstream oriented and performs horizontal planar scans of the wake. The calculated velocity deficit profiles show self-similarity in the far wake region and they can be fitted accurately to Gaussian functions. This allows to study the growth rate of the wind turbine width and the recovery of the wind speed, as well as the length of the near-wake region. The results show that a higher turbulence intensity enhances the entrainment and flow mixing in the wake region, resulting in a shorter near-wake length, a faster growth rate of the wake width and a faster recovery of the wind speed. The relationships obtained are compared to analytical models of wind turbine wakes and allow to correct the parameters prescribed until now, which were obtained from wind-tunnel measurements and LES simulations, with new, more accurate values directly derived from full-scale experiments.

6.2 Future research perspectives

Based on the developments and results presented in this thesis, the following areas are proposed for further research:

- **Study of wind turbine blade tip vortices:** the mutirotor UAV-based technique developed in chapter 2 has been proved suitable for the study and characterization of blade tip vortices of full-scale wind turbines. Further work may address the study of the signature of these vortices in terms of their intensity, advection velocity, trajectory and decay under different inflow conditions and turbine operation conditions in order to better understand their role in the flow entrainment and momentum exchange between the near wake of the wind turbine and the high energy outer region.
- **Uncertainty quantification of the triple lidar technique:** preliminary studies have shown the importance of the relative angles between the laser beams of the triple lidar setup, presented in chapter 3, in the uncertainty of its measurements. Future work may address the error propagation in the trigonometric reconstruction procedure of the

velocity vector as well as a detailed uncertainty analysis of the technique. The virtual lidar approach presented in chapter 4 can be particularly useful, since different angular configurations, noise levels for each radial velocity measurement and inflow conditions can be easily simulated.

- **Volumetric characterization of full-scale wind turbine wakes with nacelle-mounted lidars:** one of the attributes of the far wake region of a wind turbine that simplifies its characterization and modeling is the self-similarity of the velocity deficit profile. Many studies and models, such as the one presented in chapter 5, assume an axial symmetry of these velocity profiles. Nevertheless, there is enough evidence from experimental data and LES simulations that indicate that the spanwise and vertical growth rates of the wake can differ and that the thermal stability of the ABL can be one of the key variables that determine this effect. Preliminary analysis of volumetric measurements -optimized using the virtual lidar approach as explained in chapter 4- obtained with the same lidar inflow characterization presented in chapter 5, also corroborate this fact. Further analysis of this data set may help understand the roles of different atmospheric conditions -such as longitudinal, transversal and vertical turbulence intensity, thermal stability and veer- in the expansion and the velocity recovery of the far wake, obtaining a complete picture of the latter and providing valuable information for the validation of more complex analytical models as well as LES simulation frameworks.

Bibliography

- Aitken, M. L. and Lundquist, J. K. Utility-scale wind turbine wake characterization using nacelle-based long-range scanning lidar. *Journal of Atmospheric and Oceanic Technology*, 31(7):1529–1539, 2014. ISSN 15200426.
- Aitken, M. L., Banta, R. M., Pichugina, Y. L., and Lundquist, J. K. Quantifying Wind Turbine Wake Characteristics from Scanning Remote Sensor Data. *Journal of Atmospheric and Oceanic Technology*, 31(4):765–787, apr 2014. ISSN 0739-0572.
- Angelou, N., Mann, J., Sjöholm, M., and Courtney, M. Direct measurement of the spectral transfer function of a laser based anemometer. *Review of Scientific Instruments*, 83:033111, mar 2012. ISSN 1089-7623.
- Banta, R. M., Pichugina, Y. L., Brewer, W. A., Lundquist, J. K., Kelley, N. D., Sandberg, S. P., Alvarez, R. J., Hardesty, R. M., and Weickmann, A. M. 3D volumetric analysis of wind turbine wake properties in the atmosphere using high-resolution Doppler lidar. *Journal of Atmospheric and Oceanic Technology*, 32(5):904–914, 2015. ISSN 15200426.
- Barthelmie, R. J., Hansen, K., Frandsen, S. T., Rathmann, O., Schepers, J. G., Schlez, W., Phillips, J., Rados, K., Zervos, A., Politis, E. S., and Chaviaropoulos, P. K. Modelling and measuring flow and wind turbine wakes in large wind farms offshore. *Wind Energy*, 12(5):431–444, 2009. ISSN 10954244.
- Barthelmie, R. J., Pryor, S. C., Frandsen, S. T., Hansen, K. S., Schepers, J. G., Rados, K., Schlez, W., Neubert, A., Jensen, L. E., and Neckelmann, S. Quantifying the impact of wind turbine wakes on power output at offshore wind farms. *Journal of Atmospheric and Oceanic Technology*, 27(8):1302–1317, 2010. ISSN 07390572.
- Bastankhah, M. and Porté-Agel, F. A new analytical model for wind-turbine wakes. *Renewable Energy*, 70:116–123, 2014. ISSN 09601481.
- Bastankhah, M. and Porté-Agel, F. Experimental and theoretical study of wind turbine wakes in yawed conditions. *Journal of Fluid Mechanics*, 806:506–541, 2016. ISSN 14697645.
- Bastankhah, M., Porté-Agel, F., and Porte-Agel, F. Wind tunnel study of the wind turbine interaction with a boundary-layer flow: Upwind region, turbine performance, and wake region. *Physics of Fluids*, 29(6):065105, jun 2017. ISSN 10897666.

Bibliography

- Benedict, L. H. and Gould, R. D. Towards better uncertainty estimates for turbulence statistics. *Experiments in Fluids*, 22(2):129–136, dec 1996. ISSN 0723-4864.
- Bingöl, F., Mann, J., and Larsen, G. Light detection and ranging measurements of wake dynamics part I: one-dimensional scanning. *Wind Energy*, 13:51–61, 2010.
- Bodini, N., Zardi, D., and Lundquist, J. K. Three-dimensional structure of wind turbine wakes as measured by scanning lidar. *Atmospheric Measurement Techniques*, 10(8):2881–2896, aug 2017. ISSN 1867-8548.
- Carbajo Fuertes, F., Iungo, G. V., and Porté-Agel, F. 3D Turbulence Measurements Using Three Synchronous Wind Lidars: Validation against Sonic Anemometry. *Journal of Atmospheric and Oceanic Technology*, 31(7):1549–1556, jul 2014. ISSN 0739-0572.
- Chamorro, L. P. and Porté-Agel, F. A wind-tunnel investigation of wind-turbine wakes: Boundary-Layer turbulence effects. *Boundary-Layer Meteorology*, 132(1):129–149, 2009. ISSN 00068314.
- Chamorro, L. P. and Porté-Agel, F. Turbulent flow inside and above a wind farm: A wind-tunnel study. *Energies*, 4(11):1916–1936, 2011. ISSN 19961073.
- Chehouri, A., Younes, R., Ilinca, A., and Perron, J. Review of performance optimization techniques applied to wind turbines, 2015. ISSN 03062619.
- Crespo, A., Hernández, J., and Frandsen, S. Survey of modelling methods for wind turbine wakes and wind farms. *Wind Energy*, 2(1):1–24, 1999. ISSN 1095-4244.
- Doubrawa, P., Barthelmie, R., Wang, H., Pryor, S., and Churchfield, M. Wind Turbine Wake Characterization from Temporally Disjunct 3-D Measurements. *Remote Sensing*, 8(11):939, 2016. ISSN 2072-4292.
- Drechsel, S., Mayr, G. J., Chong, M., and Chow, F. K. Volume Scanning Strategies for 3D Wind Retrieval from Dual-Doppler Lidar Measurements. *Journal of Atmospheric and Oceanic Technology*, 27(11):1881–1892, nov 2010. ISSN 0739-0572.
- Dupont, A., Paanathoen, P., Lecordier, J. C., and Gajan, P. Influence of temperature on the frequency response of fine-wire thermocouples over the range (300K-800K) in airflows. *Journal of Physics E: Scientific Instruments*, 17(9):808–812, sep 1984. ISSN 0022-3735.
- El-Asha, S., Zhan, L., and Iungo, G. V. Quantification of power losses due to wind turbine wake interactions through SCADA, meteorological and wind LiDAR data. *Wind Energy*, 20(11):1823–1839, 2017. ISSN 10991824.
- Elston, J., Argrow, B., Stachura, M., Weibel, D., Lawrence, D., and Pope, D. Overview of small fixed-wing unmanned aircraft for meteorological sampling. *Journal of Atmospheric and Oceanic Technology*, 32(1):97–115, 2015. ISSN 15200426.

- Emeis, S. *Surface-Based Remote Sensing of the Atmospheric Boundary Layer*, volume 40 of *Atmospheric and Oceanographic Sciences Library*. Springer Netherlands, Dordrecht, 2011. ISBN 978-90-481-9339-4.
- Gebraad, P., Thomas, J. J., Ning, A., Fleming, P., and Dykes, K. Maximization of the annual energy production of wind power plants by optimization of layout and yaw-based wake control. *Wind Energy*, 20(1):97–107, 2017. ISSN 10991824.
- Grant, I. and Parkin, P. A DPIV study of the trailing vortex elements from the blades of a horizontal axis wind turbine in yaw. *Experiments in Fluids*, 28(4):368–376, apr 2000. ISSN 0723-4864.
- Grant, I., Mo, M., Pan, X., Parkin, P., Powell, J., Reinecke, H., Shuang, K., Coton, F., and Lee, D. An experimental and numerical study of the vortex filaments in the wake of an operational, horizontal-axis, wind turbine. *Journal of Wind Engineering and Industrial Aerodynamics*, 85(2):177–189, apr 2000. ISSN 01676105.
- Haans, W., Sant, T., van Kuik, G., and van Bussel, G. HAWT near-wake aerodynamics, Part I: axial flow conditions. *Wind Energy*, 11(3):245–264, may 2008. ISSN 10954244.
- Hansen, K. S., Barthelmie, R. J., Jensen, L. E., and Sommer, A. The impact of turbulence intensity and atmospheric stability on power deficits due to wind turbine wakes at Horns Rev wind farm. *Wind Energy*, 15(1):183–196, jan 2012. ISSN 10954244.
- Herbert-Acero, J., Probst, O., Réthoré, P.-E., Larsen, G., and Castillo-Villar, K. A Review of Methodological Approaches for the Design and Optimization of Wind Farms. *Energies*, 7(11):6930–7016, 2014. ISSN 1996-1073.
- Herges, T. G., Maniaci, D. C., Naughton, B. T., Mikkelsen, T., and Sjöholm, M. High resolution wind turbine wake measurements with a scanning lidar. *Journal of Physics: Conference Series*, 854(1), 2017. ISSN 17426596.
- Hill, M., Calhoun, R., Fernando, H. J. S., Wieser, A., Dörnbrack, A., Weissmann, M., Mayr, G., and Newsom, R. Coplanar Doppler Lidar Retrieval of Rotors from T-REX. *Journal of the Atmospheric Sciences*, 67(3):713–729, mar 2010. ISSN 0022-4928.
- Hong, J., Toloui, M., Chamorro, L. P., Guala, M., Howard, K., Riley, S., Tucker, J., and Sotiropoulos, F. Natural snowfall reveals large-scale flow structures in the wake of a 2.5-MW wind turbine. *Nature Communications*, 5(May):1–9, jun 2014. ISSN 2041-1723.
- Hooper, J. and Musgrove, A. Reynolds stress, mean velocity, and dynamic static pressure measurement by a four-hole pressure probe. *Experimental Thermal and Fluid Science*, 15(4):375–383, 1997. ISSN 08941777.
- Lungo, G. V. Experimental characterization of wind turbine wakes: Wind tunnel tests and wind LiDAR measurements. *Journal of Wind Engineering and Industrial Aerodynamics*, 149:35–39, 2016. ISSN 01676105.

Bibliography

- Iungo, G. V. and Porté-Agel, F. Volumetric lidar scanning of wind turbine wakes under convective and neutral atmospheric stability regimes. *Journal of Atmospheric and Oceanic Technology*, 31(10):2035–2048, 2014. ISSN 15200426.
- Iungo, G. V., Wu, Y.-T., and Porté-Agel, F. Field Measurements of Wind Turbine Wakes with Lidars. *Journal of Atmospheric and Oceanic Technology*, 30(2):274–287, feb 2013a. ISSN 0739-0572.
- Iungo, G. V., Wu, Y. T., and Porté-Agel, F. Field measurements of wind turbine wakes with lidars. *Journal of Atmospheric and Oceanic Technology*, 30(2):274–287, 2013b. ISSN 07390572.
- Kaimal, J. C. and Finnigan, J. J. *Atmospheric boundary layer flows: their structure and measurement*, volume 72. 1994. ISBN 0195062396.
- Käsler, Y., Rahm, S., Simmet, R., and Kühn, M. Wake measurements of a multi-MW wind turbine with coherent long-range pulsed doppler wind lidar. *Journal of Atmospheric and Oceanic Technology*, 27(9):1529–1532, sep 2010. ISSN 07390572.
- Kato, K., Tagawa, M., and Kaifuku, K. Fluctuating temperature measurement by a fine-wire thermocouple probe: Influences of physical properties and insulation coating on the frequency response. *Measurement Science and Technology*, 18(3):779–789, 2007. ISSN 13616501.
- Kocer, G., Mansour, M., Chokani, N., Abhari, R., and Müller, M. Full-Scale Wind Turbine Near-Wake Measurements Using an Instrumented Uninhabited Aerial Vehicle. *Journal of Solar Energy Engineering*, 133(4):041011, 2011. ISSN 01996231.
- Kongara, S., Calhoun, R., Choukulkar, A., and Boldi, M. Velocity retrieval for coherent Doppler lidar. *International Journal of Remote Sensing*, 33(November):3596–3613, 2012.
- Köpp, F., Schwiesow, R. L., and Werner, C. Remote Measurements of Boundary-Layer Wind Profiles Using a CW Doppler Lidar. *Journal of Climate and Applied Meteorology*, 23:148–154, 1984.
- Leishman, J. G., Coyne, A. J., and Han, Y. O. Measurements of the Velocity and Turbulence Structure. *AIAA Journal*, 35(3):477–485, mar 1997. ISSN 0001-1452.
- Lignarolo, L., Ragni, D., Krishnaswami, C., Chen, Q., Simão Ferreira, C., and van Bussel, G. Experimental analysis of the wake of a horizontal-axis wind-turbine model. *Renewable Energy*, 70:31–46, oct 2014a. ISSN 09601481.
- Lignarolo, L. E., Ragni, D., Krishnaswami, C., Chen, Q., Simão Ferreira, C. J., and van Bussel, G. J. Experimental analysis of the wake of a horizontal-axis wind-turbine model. *Renewable Energy*, 70:31–46, 2014b. ISSN 09601481.
- Lundquist, J. K., Churchfield, M. J., Lee, S., and Clifton, A. Quantifying error of lidar and sodar doppler beam swinging measurements of wind turbine wakes using computational fluid dynamics. *Atmospheric Measurement Techniques*, 8(2):907–920, 2015. ISSN 18678548.

- Machefaux, E., Larsen, G. C., Troldborg, N., Gaunaa, M., and Rettenmeier, A. Empirical modeling of single-wake advection and expansion using full-scale pulsed lidar-based measurements. *Wind Energy*, 18(12):2085–2103, dec 2015. ISSN 10954244.
- Machefaux, E., Larsen, G. C., Koblitz, T., Troldborg, N., Kelly, M. C., Chougule, A., Hansen, K. S., and Rodrigo, J. S. An experimental and numerical study of the atmospheric stability impact on wind turbine wakes. *Wind Energy*, 19(10):1785–1805, oct 2016. ISSN 10954244.
- Mann, J., Cariou, J. J.-P., Courtney, M. S., Parmentier, R., Mikkelsen, T., Wagner, R., Lindelöw, P., Sjöholm, M., and Enevoldsen, K. Comparison of 3D turbulence measurements using three staring wind lidars and a sonic anemometer. *Meteorologische Zeitschrift*, 1:012012, may 2008. ISSN 1755-1315.
- Mann, J., Peña, A., Bingöl, F., Wagner, R., and Courtney, M. S. Lidar Scanning of Momentum Flux in and above the Atmospheric Surface Layer. *Journal of Atmospheric and Oceanic Technology*, 27(6):959–976, jun 2010. ISSN 0739-0572.
- Mansour, M., Kocer, G., Lenherr, C., Chokani, N., and Abhari, R. S. Seven-Sensor Fast-Response Probe for Full-Scale Wind Turbine Flowfield Measurements. *Journal of Engineering for Gas Turbines and Power*, 133(8):081601, 2011. ISSN 07424795.
- Markfort, C. D., Zhang, W., and Porté-Agel, F. Turbulent flow and scalar transport through and over aligned and staggered wind farms. *Journal of Turbulence*, 13(February):N33, 2012. ISSN 1468-5248.
- Martin, S., Bange, J., and Beyrich, F. Meteorological profiling of the lower troposphere using the research UAV "M²AV Carolo". *Atmospheric Measurement Techniques*, 4(4): 705–716, apr 2011. ISSN 1867-8548.
- Mast, E. H. M., Vermeer, L. J., and van Bussel, G. J. W. Estimation of the circulation distribution on a rotor blade from detailed near wake velocities. *Wind Energy*, 7(3):189–209, jul 2004. ISSN 1095-4244.
- Mauder, M. and Zeeman, M. J. Field intercomparison of prevailing sonic anemometers. *Atmospheric Measurement Techniques*, 11(1):249–263, 2018. ISSN 18678548.
- Meyer Forsting, A. R., Troldborg, N., Murcia Leon, J. P., Sathe, A., Angelou, N., and Vignaroli, A. Validation of a CFD model with a synchronized triple-lidar system in the wind turbine induction zone. *Wind Energy*, 20(8):1481–1498, aug 2017. ISSN 10954244.
- Mikkelsen, R. *Actuator Disc Methods Applied to Wind Turbines*. PhD thesis, Technical University of Denmark, 2003.
- Miller, M. A., Kiefer, J., Westergaard, C., and Hultmark, M. Model Wind Turbines Tested at Full-Scale Similarity. In *Journal of Physics: Conference Series*, volume 753, 2016.

Bibliography

- Mirocha, J. D., Rajewski, D. A., Marjanovic, N., Lundquist, J. K., Kosović, B., Draxl, C., and Churchfield, M. J. Investigating wind turbine impacts on near-wake flow using profiling lidar data and large-eddy simulations with an actuator disk model. *Journal of Renewable and Sustainable Energy*, 7(4), 2015. ISSN 19417012.
- Mullan, B. *Instruments and Techniques of Atmospheric Measurement*. ML Books International, 2016. ISBN 9781682863619.
- Newman, J. F. and Clifton, A. An error reduction algorithm to improve lidar turbulence estimates for wind energy. *Wind Energy Science*, 2(1):77–95, feb 2017. ISSN 2366-7451.
- Newman, J. F., Bonin, T. A., Klein, P. M., Wharton, S., and Newsom, R. K. Testing and validation of multi-lidar scanning strategies for wind energy applications. *Wind Energy*, 19(12):2239–2254, dec 2016. ISSN 10954244.
- Newsom, R. and Banta, R. Assimilating coherent Doppler lidar measurements into a model of the atmospheric boundary layer. Part I: Algorithm development and sensitivity to measurement error. *Journal of Atmospheric and Oceanic Technology*, 21:1328–1345, 2004.
- Newsom, R., Ligon, D., Calhoun, R., Heap, R., Gregan, E., and Princevac, M. Retrieval of microscale wind and temperature fields from single- and dual-Doppler Lidar data. *Journal of Applied Meteorology*, 44:1324–1345, 2005.
- Niayifar, A. and Porté-Agel, F. Analytical modeling of wind farms: A new approach for power prediction. *Energies*, 9(9):1–13, 2016. ISSN 19961073.
- Pandey, D. K. Response time correlations for chromel-constantan thermocouples in flowing hot air. *Journal of Physics E: Scientific Instruments*, 18(8):712–713, aug 1985. ISSN 0022-3735.
- Pearson, G., Davies, F., and Collier, C. An analysis of the performance of the UFAM pulsed Doppler lidar for observing the boundary layer. *Journal of Atmospheric and Oceanic Technology*, 26(2):240–250, 2009. ISSN 07390572.
- Pichugina, Y. L., Banta, R. M., Brewer, W. A., Sandberg, S. P., and Hardesty, R. M. Doppler Lidar-Based Wind-Profile Measurement System for Offshore Wind-Energy and Other Marine Boundary Layer Applications. *Journal of Applied Meteorology and Climatology*, 51(2): 327–349, feb 2012. ISSN 1558-8424.
- Pope, S. B. *Turbulent Flows*, volume 1. 2000. ISBN 0521598869.
- Porté-Agel, F., Meneveau, C., and Parlange, M. B. A scale-dependent dynamic model for large-eddy simulation: application to a neutral atmospheric boundary layer. *Journal of Fluid Mechanics*, 415:261–284, 2000. ISSN 00221120.
- Porté-Agel, F., Wu, Y.-T., Lu, H., and Conzemius, R. J. Large-eddy simulation of atmospheric boundary layer flow through wind turbines and wind farms. *Journal of Wind Engineering and Industrial Aerodynamics*, 99(4):154–168, 2011. ISSN 01676105.

- Rambola, D. *Atmospheric Measurement Techniques*. ML Books International, 2016.
- Reineman, B. D., Lenain, L., Statom, N. M., and Melville, W. K. Development and Testing of Instrumentation for UAV-Based Flux Measurements within Terrestrial and Marine Atmospheric Boundary Layers. *Journal of Atmospheric and Oceanic Technology*, 30(7):1295–1319, jul 2013. ISSN 0739-0572.
- Reuder, J. and Jonassen, M. O. First Results of Turbulence Measurements in a Wind Park with the Small Unmanned Meteorological Observer SUMO. *Energy Procedia*, 24(January): 176–185, 2012. ISSN 18766102.
- Sathe, A. and Mann, J. Measurement of turbulence spectra using scanning pulsed wind lidars. *Journal of Geophysical Research: Atmospheres*, 117(D1):n/a–n/a, jan 2012. ISSN 01480227.
- Sathe, A. and Mann, J. A review of turbulence measurements using ground-based wind lidars. *Atmospheric Measurement Techniques*, 6(11):3147–3167, nov 2013. ISSN 1867-8548.
- Sathe, A., Mann, J., Gottschall, J., and Courtney, M. S. Can Wind Lidars Measure Turbulence? *Journal of Atmospheric and Oceanic Technology*, 28(7):853–868, jul 2011. ISSN 0739-0572.
- Smalikho, I. N., Banakh, V. A., Pichugina, Y. L., Brewer, W. A., Banta, R. M., Lundquist, J. K., and Kelley, N. D. Lidar investigation of atmosphere effect on a wind turbine wake. *Journal of Atmospheric and Oceanic Technology*, 30(11):2554–2570, nov 2013. ISSN 07390572.
- Sørensen, J. N. and Shen, W. Z. Numerical Modeling of Wind Turbine Wakes. *Journal of Fluids Engineering*, 124(2):393, 2002. ISSN 00982202.
- Sorensen, J. N., Mikkelsen, R. F., Henningson, D. S., Ivanell, S., Sarmast, S., and Andersen, S. J. Simulation of wind turbine wakes using the actuator line technique. *Philosophical Transactions of the Royal Society A: Mathematical, Physical and Engineering Sciences*, 373(2035):20140071–20140071, jan 2015. ISSN 1364-503X.
- Spieß, T., Bange, J., Buschmann, M., and Vörsmann, P. First application of the meteorological Mini-UAV 'M2AV'. *Meteorologische Zeitschrift*, 16(2):159–169, may 2007. ISSN 0941-2948.
- St. Martin, C. M., Lundquist, J. K., Clifton, A., Poulos, G. S., and Schreck, S. J. Wind turbine power production and annual energy production depend on atmospheric stability and turbulence. *Wind Energy Science Discussions*, pages 1–37, 2016. ISSN 2366-7621.
- Stawiarski, C., Traumner, K., Knigge, C., and Calhoun, R. Scopes and challenges of dual-doppler lidar wind measurements-an error analysis. *Journal of Atmospheric and Oceanic Technology*, 30(9):2044–2062, 2013. ISSN 07390572.
- Stawiarski, C., Träumner, K., Kottmeier, C., Knigge, C., and Raasch, S. Assessment of Surface-Layer Coherent Structure Detection in Dual-Doppler Lidar Data Based on Virtual Measurements. *Boundary-Layer Meteorology*, 156(3):371–393, 2015. ISSN 15731472.

Bibliography

- Stoll, R. and Porté-Agel, F. Dynamic subgrid-scale models for momentum and scalar fluxes in large-eddy simulations of neutrally stratified atmospheric boundary layers over heterogeneous terrain. *Water Resources Research*, 42(1):1–18, jan 2006. ISSN 00431397.
- Stull, R. B. *An Introduction to Boundary Layer Meteorology*. Springer Netherlands, Dordrecht, 1988. ISBN 978-90-277-2769-5.
- Subramanian, B., Chokani, N., and Abhari, R. Experimental analysis of wakes in a utility scale wind farm. *Journal of Wind Engineering and Industrial Aerodynamics*, 138:61–68, mar 2015a. ISSN 01676105.
- Subramanian, B., Chokani, N., and Abhari, R. S. Drone-Based Experimental Investigation of Three-Dimensional Flow Structure of a Multi-Megawatt Wind Turbine in Complex Terrain. *Journal of Solar Energy Engineering*, 137(5):051007, jul 2015b. ISSN 0199-6231.
- Subramanian, B., Chokani, N., and Abhari, R. S. Aerodynamics of wind turbine wakes in flat and complex terrains. *Renewable Energy*, 85:454–463, 2016. ISSN 18790682.
- Tagawa, M., Kato, K., and Ohta, Y. Response compensation of fine-wire temperature sensors. *Review of Scientific Instruments*, 76(9), 2005. ISSN 00346748.
- Thomsen, K. and Sørensen, P. Fatigue loads for wind turbines operating in wakes. *Journal of Wind Engineering and Industrial Aerodynamics*, 80(1-2):121–136, 1999. ISSN 01676105.
- Toloui, M., Chamorro, L. P., and Hong, J. Detection of tip-vortex signatures behind a 2.5 MW wind turbine. *Journal of Wind Engineering and Industrial Aerodynamics*, 143:105–112, 2015. ISSN 0167-6105.
- Torben Knudsen, T. B. and Automation, M. S. Survey of wind farm control—power and fatigue optimization. *Wind Energy*, pages 1–19, 2014. ISSN 1099-1824.
- Trujillo, J., Bingöl, F., Larsen, G., Mann, J., and Kühn, M. Light detection and ranging measurements of wake dynamics. Part II: two-dimensional scanning. *Wind Energy*, 14:61–75, 2011.
- Ulden, A. and Wieringa, J. Atmospheric boundary layer research at Cabauw. *Boundary-Layer Meteorology*, 78:39–69, 1996.
- van den Kroonenberg, A., Martin, T., Buschmann, M., Bange, J., and Vörsmann, P. Measuring the Wind Vector Using the Autonomous Mini Aerial Vehicle M 2 AV. *Journal of Atmospheric and Oceanic Technology*, 25(11):1969–1982, nov 2008. ISSN 0739-0572.
- van Dooren, M. F., Trabucchi, D., and Kühn, M. A methodology for the reconstruction of 2D horizontal wind fields of wind turbinewakes based on dual-Doppler lidar measurements. *Remote Sensing*, 8(10), 2016. ISSN 20724292.

- van Dooren, M. F., Campagnolo, F., Sjöholm, M., Angelou, N., Mikkelsen, T., and Floris, M. Demonstration and uncertainty analysis of synchronised scanning lidar measurements of 2-D velocity fields in a boundary-layer wind tunnel. *Wind Energy Science*, 2(1):329–341, 2017.
- Vasiljević, N., Lea, G., Courtney, M., Cariou, J.-P., Mann, J., and Mikkelsen, T. Long-Range WindScanner System. *Remote Sensing*, 8(12):896, oct 2016. ISSN 2072-4292.
- Verkaik, J. W. and Holtslag, A. A. M. Wind profiles, momentum fluxes and roughness lengths at Cabauw revisited. *Boundary-Layer Meteorology*, 122:701–719, oct 2007. ISSN 0006-8314.
- Vermeer, L., Sørensen, J., and Crespo, A. Wind turbine wake aerodynamics. *Progress in Aerospace Sciences*, 39(6):467–510, 2003. ISSN 03760421.
- Vermeer, L. J. Measurements on the properties of the tip vortex of a rotor model. In *European Wind Energy Conference*, pages 805–808, Thessaloniki, 1994.
- Vermeer, L. J. A review of wind turbine wake research at TU Delft. In *20th 2001 ASME Wind Energy Symposium*, number c, pages 103–113, Reston, Virginia, jan 2001. American Institute of Aeronautics and Astronautics.
- Wieringa, J. Updating the Davenport roughness classification. *Journal of Wind Engineering and Industrial Aerodynamics*, 41(1-3):357–368, oct 1992. ISSN 01676105.
- Wildmann, N., Hofsäß, M., Weimer, F., Joos, A., and Bange, J. MASC – a small Remotely Piloted Aircraft (RPA) for wind energy research. *Advances in Science and Research*, 11:55–61, 2014a. ISSN 1992-0636.
- Wildmann, N., Ravi, S., and Bange, J. Towards higher accuracy and better frequency response with standard multi-hole probes in turbulence measurement with remotely piloted aircraft (RPA). *Atmospheric Measurement Techniques*, 7(4):1027–1041, 2014b. ISSN 18678548.
- Williams, A. and Marcotte, D. Wind measurements on a maneuvering twin-engine turboprop aircraft accounting for flow distortion. *Journal of Atmospheric and Oceanic Technology*, 17(6):795–810, 2000. ISSN 07390572.
- Wu, Y. T. and Porté-Agel, F. Large-Eddy Simulation of Wind-Turbine Wakes: Evaluation of Turbine Parametrisations. *Boundary-Layer Meteorology*, 138(3):345–366, 2011. ISSN 00068314.
- Wu, Y. T. and Porté-Agel, F. Modeling turbine wakes and power losses within a wind farm using LES: An application to the Horns Rev offshore wind farm. *Renewable Energy*, 75:945–955, 2015. ISSN 18790682.
- Wyngaard, J. The effects of probe-induced flow distortion on atmospheric turbulence measurements. *Journal of Applied Meteorology*, 20:784–794, 1981.

Bibliography

Zhang, W., Markfort, C. D., and Porté-Agel, F. Wind-Turbine Wakes in a Convective Boundary Layer: A Wind-Tunnel Study. *Boundary-Layer Meteorology*, 146(2):161–179, 2013. ISSN 00068314.

Fernando Carbajo Fuertes

Place Chauderon 20, CH-1003 Lausanne, Switzerland

(+41) 077 477 56 64

fernando.carbajo@epfl.ch

Education

École polytechnique fédérale de Lausanne (CH) – PhD candidate 2013 – Present
- Teaching assistant, fluid mechanics: co-responsible for course design, lectures, laboratory work and examinations

Von Karman Institute for Fluid Dynamics (BE) – Research Master in Fluid Dynamics Oct 2011 – Oct 2012
- Full scholarship; Honors student & Belgian Government Award

Technical University of Denmark (DK) – M.Sc. Wind Energy Sep 2009 – Sep 2011
- Top-grade MSc thesis

Polytechnic University of Madrid (SP) – B.Sc. Aeronautical Engineering Sep 2005 – Jul 2009
- Top 3.7% percentile & Honors B.Sc. thesis

Journal publications

F. Carbajo Fuertes et al. An inexpensive and versatile technique for wide frequency range surface pressure measurements: an application for the study of turbulent buffeting of a square cylinder. *Experiments in Fluids*. January 2014, 55:1627.

F. Carbajo Fuertes, G.V. Iungo and F. Porté-Agel. 3D turbulence measurements using three synchronous wind LiDARs: validation against sonic anemometry. *Journal of Atmospheric and Oceanic Technology*, 31:1549-1556, 2014.

F. Carbajo Fuertes, L. Wilhelm and F. Porté-Agel. Multirotor UAV-based platform for the measurement of atmospheric turbulence: validation and signature detection of tip vortices of wind turbine blades. Under review in *Journal of Atmospheric and Oceanic Technology*.

F. Carbajo Fuertes and F. Porté-Agel. Using a virtual lidar approach to assess the accuracy of the volumetric reconstruction of a wind turbine wake. Under review in *Remote Sensing*.

F. Carbajo Fuertes, C. Markfort and F. Porté-Agel. Wind turbine wake characterization with nacelle-mounted wind LiDARs for analytical wake model validation. *Remote Sensing*, 2018, 10(5), 668.

Conferences

- **F. Carbajo Fuertes, G.V. Iungo and F. Porté-Agel.** 3D turbulence measurements using three synchronous wind LiDARs: validation against sonic anemometry. European Geosciences Union General Assembly 2013, Vienna.
- **F. Carbajo Fuertes, G.V. Iungo and F. Porté-Agel.** 3D turbulence measurements in inhomogeneous boundary layers with three wind LiDARs. 21st Symposium on Boundary Layers and Turbulence 2014, Leeds, and European Geosciences Union General Assembly 2014, Vienna.
- **F. Carbajo Fuertes, J. Legerén Álvarez, and Fernando Porté-Agel.** Wind profiling with LiDARs: detection of boundary layer inhomogeneity and uncertainty analysis. European Geosciences Union General Assembly 2015, Vienna.
- **F. Carbajo Fuertes and F. Porté-Agel.** Volumetric LiDAR scanning of a wind turbine wake and comparison with a 3D analytical wake model. 22nd Symposium on Boundary Layers and Turbulence 2016, Salt Lake City, and European Geosciences Union General Assembly 2016, Vienna.
- **F. Carbajo Fuertes and F. Porté-Agel.** Virtual wind LiDAR experiments using LES data: examples of the limitations of LiDAR profilers and scanners. 22nd Symposium on Boundary Layers and Turbulence 2016, Salt Lake City.

Research interests

- Atmospheric boundary layer
- Environmental fluid mechanics
- Experimental fluid mechanics
- Remote sensing
- Wind energy

Languages

Spanish: First language
French: Fluent
English: Fluent
Italian: Fluent
German: Beginner

